Performance Comparison Between Gas Generator and Electrically Pumped Rocket Engines Under Ablative and Regenerative Cooling

Jordan Silver

Submitted in fulfilment of the academic requirements for the degree of Master of Science in Mechanical Engineering, College of Agriculture, Engineering and Science, University of KwaZulu-Natal.

Supervisor: Prof Michael J. Brooks

Co-Supervisors: Prof Glen C. Snedden,

Mr Ryan Cooper

Declaration 1 – Plagiarism

I, Jordan Silver, declare that:

1. The research reported in this thesis, except where otherwise indicated, is my original research.
2. This thesis has not been submitted for any degree or examination at any other university.
3. This thesis does not contain other persons' data, pictures, graphs or other information, unless specifically acknowledged as being sourced from other persons.
4. This thesis does not contain other persons' writing, unless specifically acknowledged as being sourced from other researchers. Where other written sources have been quoted, then:
    a. Their words have been re-written, but the general information attributed to them has been referenced.
    b. Where their exact words have been used, then their writing has been placed in italics and inside quotation marks and referenced.
5. This thesis does not contain text, graphics or tables copied and pasted from the Internet, unless specifically acknowledged, and the source being detailed in the thesis and in the References sections.

Signed:

Mr Jordan Silver

As the candidate's Supervisor I agree/do not agree to the submission of this thesis.

Signed:

Prof Michael J. Brooks

As the candidate's Supervisor I agree/do not agree to the submission of this thesis.

Signed:

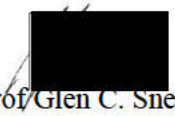

Prof Glen C. Snedden

Mr. Ryan Cooper

Acknowledgements

I would like to thank my supervisors, Prof Michael Brooks, Prof Glen Snedden and Mr. Ryan Cooper, for their continuous support and guidance throughout all stages of my research. I would also like to thank Tim Velthuysen for his assistance in cross-checking my work and for providing valuable advice for conducting my research and writing this thesis.

I am grateful to the whole ASRI team for their continued support, encouragement, and advice. Their expertise and invaluable knowledge accelerated my learning and shaped me into a better student and, most crucially, a better engineer. Thank you to the senior engineers, Duran Martin, Nino Wunderlin, Ryan Cooper, and Phillip Kwabena Konadu Gyasi-Agyei, for the time and effort to provide valuable information and expertise on the SAFFIRE engine and CLV parameters, which was the basis of my research conducted for this work Thank you to the rest of my ASRI colleagues. Not only did you provide your expertise and knowledge, but the nonstop banter kept me sane and highly motivated to complete my work.

I would also like to thank the South Africa National Space Agency (SANSA) and the Department of Science and Innovation (DSI) for funding my research.

Lastly, thank you to my family for all your sacrifices to get me to where I am now. You guys have never stopped believing in me and have continued to love and support me through all the highs and lows, showing me that perseverance and hard work will always reap rewards. A special thank you to my late grandfather, my biggest fan and supporter of my work. I know you are proud of me from above and have and will continue watching over me.

Abstract

In recent years, there has been a dramatic advancement in the global satellite industry, with new technologies allowing for smaller and more powerful satellites to be developed. Despite this, South Africa and other African countries developing satellite technologies still depend on foreign launch services as there is no indigenous capability in Africa, incurring additional costs and delays.

Against this backdrop, the University of KwaZulu-Natal's (UKZN) Aerospace Systems Research Institute (ASRI) is pursuing the development of a two-stage Commercial Launch Vehicle (CLV) to provide South Africa with a sovereign launch capability. ASRI is currently developing the booster engine for CLV - the South AFrican FIrst Rocket Engine (SAFFIRE). The booster stage will utilize a cluster of nine of the SAFFIRE engines, and the second stage will use a vacuum derivative of the SAFFIRE engine called SAFFIRE-V and will give CLV the envisioned payload capacity of 200 kg to a 500 km Sun Synchronous Orbit (SSO).

Although the design of the SAFFIRE engine is largely complete in terms of injector design, combustion chamber and nozzle geometry, and thrust output, the feed cycle responsible for delivering the propellants to the combustion chamber is undecided. In this report, the gas generator and electropump cycles are under consideration to supply propellants to the SAFFIRE and SAFFIRE-V chambers. In addition, although the chambers are currently ablatively cooled, ASRI remains interested in the possibility of using regenerative cooling. This study, therefore, considers the gas generator and electropump cycles under both cooling methods to identify which SAFFIRE engine combination can provide the best performance for CLV. To measure the performance of each engine combination, the payload mass capabilities of a hypothetical CLV are calculated using results attained from 1-dimensional simulations run in Flownex®, models coupled with Mass Estimating Relationships (MER) that evaluate the components that make up a two-stage liquid rocket engine.

The performance comparison found that each engine configuration exceeded the set payload capacity of 200 kg. For the electropump cycle, the ablative and regenerative engines achieved payload masses of 303 kg and 290 kg, respectively. The gas generator performed even better due to a lower dead mass than the electropump cycle, achieving payload masses of 392 kg and 386 kg, respectively. For both cycles, the ablatively cooled rocket engines had better payload capabilities than the regeneratively cooled engines due to a regeneratively cooled engine having a smaller expansion ratio. When the expansion ratios were made the same, the regeneratively cooled engines achieved a payload capacity of 308 kg and 405 kg for the electropump and gas generator cycles, respectively, due to the increased thrust from the heated fuel, which has an increased energy density, producing more thrust. When the dead mass of the electropump cycle was decreased by ejecting the depleted battery packs for each engine stage during the launch, the electropump payload deficit decreased from 98 kg to 29 kg for the ablative engines and 96 kg to 32 kg for the regenerative engines. Based on this study, the best performing

SAFFIRE engine configuration is a gas generator cycle with ablative cooling, giving the conceptual CLV rocket a payload of 392 kg to 500 km Sun Synchronous Orbit.

Table of Contents

List of Figures

List of Tables

Nomenclature

Symbol	Description	Unit
A	Area	m^2
AR	Area Ratio	-
b	Unknown Variable	-
d	Hydraulic Diameter	m
D	Diameter	m
e	Thickness	m
E	Earths Mass	kg
f_{inert}	Inertial Mass Fraction	-
F	Thrust	N
$F_{elec,a}$	Electropump Ablative Thrust	N
$F_{elec,r}$	Electropump Regenerative Thrust	N
$F_{GG,\ a}$	Gas Generator Ablative Thrust	N
$F_{GG,\ r}$	Gas Generator Regenerative Thrust	N
G	Earths Gravitational Constant	$m^3.kg^{-1}.s^{-2}$
H	Effective Recovery Factor	-
I_{sp}	Specific Impulse	s
K_s	Reduction in Stress	-
k	Coolant Thermal Conductivity	-
K_b	Battery Sizing Constant	-
K_{gg}	Gas Generator Safety Factor	-
K_{pi}	Injector Pressure Loss Constant	-
K_{pr}	Combustion Chamber Pressure Loss Constant	-
K_{propf}	Residual Fuel Factor	-
K_{propg}	Residual Pressurant Factor	-
K_{propo}	Residual Oxidizer Factor	-
K_{tg}	Pressurant Tank Safety Factor	-
M	Molecular Mass	kg/kmol
m	Mass	kg
$\dot{m}$	Mass Flow Rate	kg/s
P	Power	W
p	Pressure	Pa
Q	Volumetric Flow Rate	m^3/s
R_u	Universal Gas Constant	J/kg.K

R	Gas Constant	J/kmol.K
r	Local Recovery Factor	-
r_i	Inner Radius	m
r_o	Outer Radius	m
SA	Surface Area	m^2
T	Temperature	K
T_{day}	Time (1 day)	s
t_b	Burn Time	s
t_c	Characteristic Burn Time	s
t_d	Discharge Time	s
t_s	Stay Time	s
V	Volume	m^3
v	Velocity	m/s
Δv	Velocity Increment	m/s
Y	Allowable Stress	pa

Greek Symbols	**Description**	**Units**
α	Propellant Fraction	-
β	Azimuth Angle	°
γ	Specific Heat Ratio	-
δ	Power Density/Energy Density	kWh/kg or kW/kg
ε	Expansion Ratio	-
η	Efficiency	-
θ	Angle of Latitude	°
ρ	Density	kg/m^3
σ	Boundary Layer Thickness	-

Subscripts	**Description**
0	Initial Condition
1	1st Stage
2	2nd Stage
abl	Ablative Cooling
avi	Avionics
ba,en	Battery Energy

ba,po	Battery Power
bp	Battery Pack
cc	Combustion Chamber
cyl	Cylindrical
d	Drag
dry	Dry
dtu	Turbine Discharge
E	Energy
em	Electric Motor
en	Engine
epc	Electropump Cycle
ex	Extension
f	Fuel
fi	Final
fair	Fairings
fpu	Fuel Pump
ft	Fuel Tank
g	Gravity
gim	Gimble
gg	Gas Generator
ggc	Gas Generator Cycle
ggm	Gas Generator Material
He	Helium
hemi	Hemispherical
i	Initial
inj	Injector
inv	Inverter
is	Interstage Structure
itu	Inlet of Turbine
m	Material
N	Nitrogen
o	Oxidizer
opu	Oxidizer Pump
orb	Orbital
ot	Oxidizer Tank
P	Total Propellant

pg	Pressurant Gas
pi	Injector Pressure
pl	Payload
plum	Plumbing
propf	Residual Fuel
propg	Residual Pressurant
propo	Residual Oxidizer
pt	Pressurant Tank
ptu	Turbine Propellant
reg	Regenerative Cooling
sl	Sea Level
sur	Surface
tot	Total
tp	Turbopump
ts	Thrust Structure
tu	Turbine
u	Universal
ul	Ullage
wet	Wet
wire	Wiring

Abbreviation	**Description**
AC	Alternating Current
ASI	Augmented Spark Igniter
ASRI	Aerospace Systems Research Institute
BEP	Best Efficiency Point
BLDC	Brushless Direct Current
BMS	Battery Management System
CCV	Chamber Coolant Valve
CEA	Chemical Equilibrium with Applications
CFD	Computational Fluid Dynamics
CLV	Commercial Launch Vehicle
DC	Direct Current
GGFV	Gas Generator Fuel Valve
GGOV	Gas Generator Oxidizer Valve
LOX	Liquid Oxygen

LEO	Low Earth Orbit
MER	Mass Estimating Relationship
MFV	Main Fuel Valve
MR	Mass Ratio
MOV	Main Oxidizer Valve
NASA	National Aeronautics and Space Administration
NIST	National Institute of Standards and Technology
O/F	Oxidizer to Fuel Ratio
PR	Pressure Ratio
PUV	Propellant Utilization Valve
PWM	Pulse Width Modulation
RCS	Reaction Control System
RP-1	Rocket Propellant 1
SSO	Sun-synchronous orbit
UKZN	University of KwaZulu-Natal
UTS	Ultimate Tensile Strength

1. Introduction

1.1. SAFFIRE Program Summary

With the arrival of the fourth industrial revolution, there has been a dramatic rise in micro and nanosatellite deployment by countries globally. The capabilities of low earth orbital (LEO) satellites are rapidly increasing, with many countries now developing domestic nanosatellite programs (Woellert et al., 2011). Due to their advantageous low cost, shorter development time, and lower mass, numerous developing countries have begun developing their own nanosatellites (Space, 2019). Many African countries are now developing satellites for communications, agricultural, disaster management, and climate monitoring applications to improve economic growth (Anderson, 2017; Smyth, 2013). South Africa has built twelve microsatellites, ten of which have been nanosatellites launched in the past six years. On the 13th of January 2022, the country reached a milestone, marking the first launch of a satellite constellation consisting of three locally-built nanosatellites and six additional African-developed cube satellites (Isaacs, 2022).

While South Africa has made significant progress in developing nanosatellites, all satellite launches still depend on foreign launch capabilities. African countries can source commercial satellite services from outside the continent, but these come with cost implications and frequent timing delays (Smyth, 2013). Against this backdrop, the University of KwaZulu-Natal's (UKZN) Aerospace Systems Research Institute (ASRI) is pursuing the development of a small satellite Commercial Launch Vehicle (CLV) to provide South Africa with a sovereign launch capability. The current focus is CLV's booster engine - the South AFrican FIrst Rocket Engine (SAFFIRE). It is intended that CLV will provide South Africa with an economically sustainable launch service, promoting economic growth and stimulating the African aerospace industry. Figure 1-1 depicts a rendered launch of CLV.

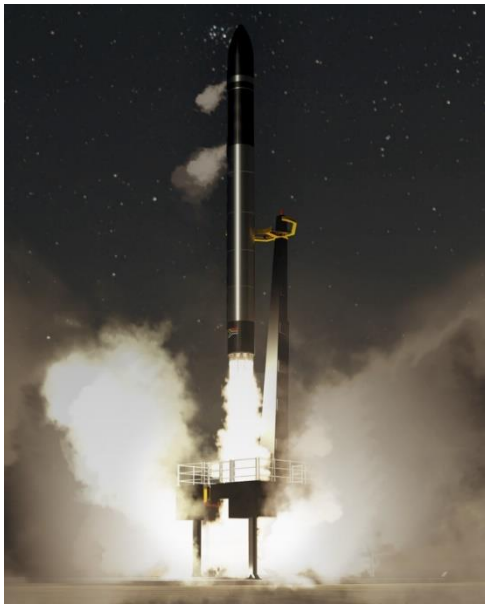

Figure 1-1: CLV rendered launch

The three primary categories of bipropellant rocket engines are defined by the physical state of the propellants used to generate thrust: solid, hybrid, and liquid. The fuel and oxidizer are mixed in solid rockets to form a solid grain containing all the chemical elements for complete combustion. Hybrid rocket propulsion systems use liquid and solid propellants, with the oxidizer typically being the liquid and the fuel a solid grain. Liquid rocket engines utilize liquid propellants for the fuel and the oxidizer, which are injected into the thrust chamber at high pressure (Sutton and Biblarz, 2001). Of the three rocket cycles, liquid rocket engines tend to have a higher specific impulse than the other engines, making them more advantageous as less propellant mass is required to produce the same thrust. Additionally, liquid rocket engines have more control than other rocket engines since the propellant flow rates can be regulated using a variety of valves (Chetty, 2018).

These considerations led to the development of the SAFFIRE program. SAFFIRE is proposed to employ a liquid rocket engine architecture using Rocket Propellant 1 (RP-1) and liquid oxygen (LOX) as the fuel and oxidizer; respectively and is designed to produce approximately 27.6 kN of thrust. To produce the necessary thrust for CLV, the SAFFIRE engine has been designed to be modular so that nine engines can be clustered together to form the booster stage for CLV. A smaller modular design reduces the cost of development, manufacture, transport, and testing of individual engines and associated components. Although the preliminary conceptual design of SAFFIRE is complete, the question remains as to which liquid rocket engine feed cycle offers the best performance for CLV in terms of payload to orbit.

Rocket propellants must be pressurized to ensure a high-pressure flow from the propellant tanks to the engine chamber of liquid rocket engines. Turbopumps conventionally feed propellants from the pressurized tanks to the thrust chamber (Huzel et al., 1992). The configuration of the propellant delivery system constitutes the engine cycle. There are a number of engine cycle types, several of which are

under consideration by ASRI for future development of the SAFFIRE engine, including the gas generator and electropump cycles. Both use a series of pumps to pressurize the propellants to a higher working pressure before entering the combustion chamber. The gas generator uses hot gases to drive a turbine connected to the propellant pumps, and the electropump cycle uses battery-driven pumps.

The gas generator engine cycle requires a portion of the main rocket propellants to be tapped-off and combusted in a gas generator to power the turbopumps (Liu et al., 2021). The electropump cycle configuration does not require propellants; rather, the pumps are powered directly via electric motors and on-board batteries. Compared with traditional liquid rocket engines, electropump liquid propellant rocket engines have a low cost of manufacture and testing, fast development, easy start-up, and high reliability. They also can achieve deep variable thrust through their electric drive system and are modular in design (Liu et al., 2021). Gas generator turbopumps require exotic materials and advanced manufacturing techniques, but they scale up better than electropumps for larger engines (Haidn, 2008). In addition to the method of driving flow, another important variable in the architecture of a rocket engine is the method by which the internal chamber wall is protected from high temperatures, with numerous concepts under consideration by ASRI.

This study analyzes four variations of the basic SAFFIRE engine: an electrically pumped engine with ablative and regenerative cooling and a turbopump-driven engine with the same two cooling variations. A one-dimensional analysis was completed for each engine, where performance characteristics were compared to aid in selecting the best configuration for the SAFFIRE program.

To measure the performance of each engine configuration, a payload mass is estimated for each of the four variations using the same mission parameters, with the configuration that produces the largest payload mass designated as having the best performance. The 1-dimensional simulations of each engine variation and a set of Mass Estimating Relationships (MER) are used to identify the engine's performance.

1.2. Thesis Outline

The present chapter covers the background of the SAFFIRE program and the motivation to produce the first South African Commercial Launch Vehicle and outlines the objectives of the study. Chapter 2 is a literature review on the propellant delivery cycles and engine cooling methods, focusing on the project's main components and how each engine configuration can be represented in a 1-dimensional model.

Chapter 3 contains the mass estimating relationships required to evaluate the mass of each feed cycle. Additional structural mass estimating relationships are used to evaluate the total mass of the launch vehicle for a more accurate payload mass estimation.

Chapter 4 outlines the simulation methodology used to create the one-dimensional models of the four SAFFIRE engine variations for the first and second-stage engines. The methodology used to create a

surrogate mixture of RP-1, evaluate the payload mass for each engine configuration, and determine the mass estimating relationship input variables is included in this chapter.

Chapter 5 contains the results and discussion of the analysis, including a verification of the one-dimensional Flownex® models using the Fastrac gas generator cycle and the Rutherford electropump cycle. The discussion addresses a performance comparison between the gas generator and electropump cycles and the payload performance comparison of each engine configuration. A mass sensitivity analysis is provided to assist in identifying the impact of input variables on the feed system masses. The dissertation concludes with Chapter 6, which contains the conclusions and recommendations for future work.

2. Literature Review

2.1. SAFFIRE Propellant Delivery

Liquid rocket engines typically consist of the following major components: the nozzle and combustion chamber, propellant tanks, a propellant control system, electric and pneumatic control systems, and a propellant feed system. Of the listed components, the propellant feed system, which supplies the propellants from the tanks to the combustion chamber, is the only component that greatly varies for each rocket engine and is referred to as a cycle (Huzel et al., 1992). The rocket engine cycle can be a pressure-fed or turbopump cycle. The cycle selection depends on the rocket engine's characteristics and overall rocket design, including the mass flow rates, combustion chamber pressures, burn time, payload mass, cost, reliability, reusability, and ease of manufacturing. The pressure-fed cycle has high reliability, few subcomponents, and moving parts like a pump. The pressure-fed cycle requires the pressure of the propellant tanks to be constantly greater than the chamber pressure for the mission's duration. As the required chamber pressure increases, the tank wall thickness increases to withstand the increased pressure, adding weight and limiting the rocket's performance. Thus, the pressure-fed cycle is limited to low chamber pressures and payload mass compared to pump-fed cycles. Due to the limited performance of the pressure-fed cycle, only turbopump cycles and the electropump cycle were considered for the SAFFIRE engine, which is intended to propel CLV.

A turbopump system pressurizes the propellants before entering the combustion chamber using pumps mechanically driven through a shaft connected to a turbine. Turbopumps can be categorized into single-shaft dual-pump turbopump assemblies with a common turbine and individual fuel and oxidizer turbopumps with dedicated turbines for each pump. The single-shaft turbopump assemblies have distinct features: the fuel and oxidizer pump is a single assembly that features a single turbine connected to each pump using a mechanical link of rotors, leading to each pump rotor having the same rotational speed. The single-shaft turbopump setup is beneficial when the densities of the propellants are closely matched (Demyanenko et al., 2006). Individual fuel and oxidizer turbopump assemblies are often classified as double-shaft assemblies and utilize a dedicated turbine for each pump, allowing different pump speeds to be achieved. Dual shaft assemblies are commonly used for propellants that have a large density variation (Demyanenko et al., 2006).

Electropump cycles also use a set of pumps to pressurize the propellant driven by electric motors. Thus, how the propellant pumps are powered differentiates the different feed cycles. There are four well-known pump-fed systems in modern rocket engines: the gas generator cycle, the staged combustion cycle, the expander cycle, and the electric pump-fed cycle, each of which is discussed in detail in the following subchapters.

2.1.1. Gas Generator Cycle

The gas generator, or open cycle, is a popular rocket engine cycle (Sutton and Biblarz, 2001). The gas generator cycle consists of many of the same components as the pressure-fed system, including the thrust chamber, nozzle, valves, piping, and propellant tanks, additional components include a gas generator and turbine, which power the pumps necessary to pressurize the propellants. A gas generator is a device that generates hot gas to power the turbine. During use, a small amount of the propellant is diverted to a gas generator, ignited, and expanded, creating hot, high-pressure exhaust gas. The hot gas is then directed through the turbine, which expands, rotating the turbine and the pumps through a connecting shaft (Law, 2022). Figure 2-1 shows the flow diagram of the propellants and exhaust gases of the gas generator engine cycle.

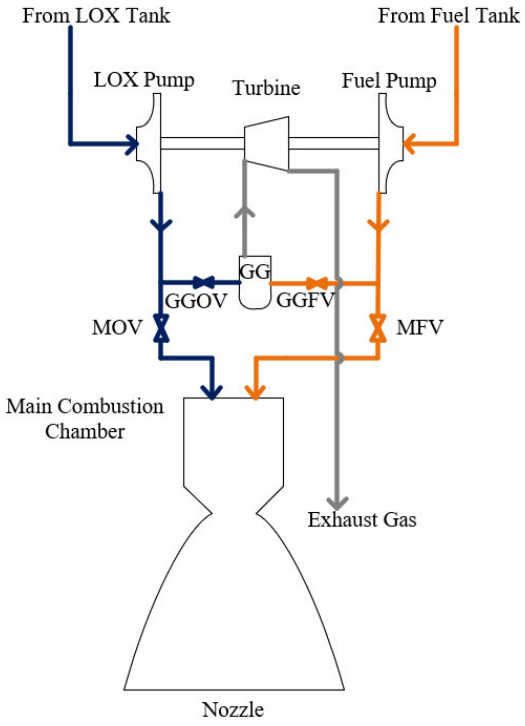

Figure 2-1: Gas generator engine cycle with ablative cooling

Since the main combustion chamber does not reuse the exhaust gases, they are expelled into the atmosphere, which is why this is called an open cycle. More thrust can be produced by increasing the mass flow rate of the propellant that flows into the gas generator as the combusted gases increase in inlet temperature and pressure, allowing the turbine to spin faster and further increasing the turbopump speed. Since the percentage of propellant flows through the gas generator is small compared to the staged combustion and expansion cycles, the turbine's efficiency is not as influential on the overall performance. Thus, the gas generator cycle is designed for low flow rates and high-pressure differentials to generate the most power while utilizing as little propellant as possible.

The turbine is temperature- and mechanically-limited, and there is an upper limit of inlet temperature and rotational speed to ensure the turbine components are not damaged and can withstand the full burn duration. Most gas generator peripheral turbine blade speeds are limited to 500 - 600 m/s and have an inlet temperature limit of 1,430°C (Rao, 2010; Smyth, 2013). The gas generator operates at a less-than-optimal burning ratio with a fuel-rich oxidizer-to-fuel (*O/F*) ratio of 0.2 - 0.5, limiting combustion temperature and, thus, the turbine inlet temperature (Aerospace Engineering, 2012). The gas generator cycle offers the advantage of simplicity and lower mass compared to the staged and expander cycles because it contains fewer components and piping arrangements. The ease of manufacturing and overall cost are also lower than the other two cycles. However, the gas generator cycle has a large tubing complexity of the propellant feed lines and exhaust and a lengthy start-up sequence. It has a lower efficiency than the other cycles since the exhaust gas used for the turbine are not utilized, reducing the overall specific impulse of the engine (Huzel et al., 1992).

2.1.2. Staged Combustion Cycle

The staged combustion cycle, otherwise known as the closed cycle, is more complex than the gas generator and expander cycles, as it uses partially combusted exhaust gases from the turbine and injects them into the combustion chamber for further combustion. This requires exotic materials to withstand extreme environments and complex layouts and components. The staged engine cycle achieves additional thrust and higher efficiency than the gas generator cycle by utilizing all of the propellants. In the staged combustion cycle, the gas generator is replaced by a preburner. Unlike a gas generator that fully combusts the relatively small amounts of fuel and oxidizer that enter the chamber, a preburner only allows fuel-rich mixtures into the combustion chamber, leading to incomplete combustion. The fuel-rich exhaust gases flow through the first combustion chamber to expand the turbine, generating rotational power for the pumps (Sutton and Biblarz, 2001). Figure 2-2 shows the fluid flow path of a staged engine cycle.

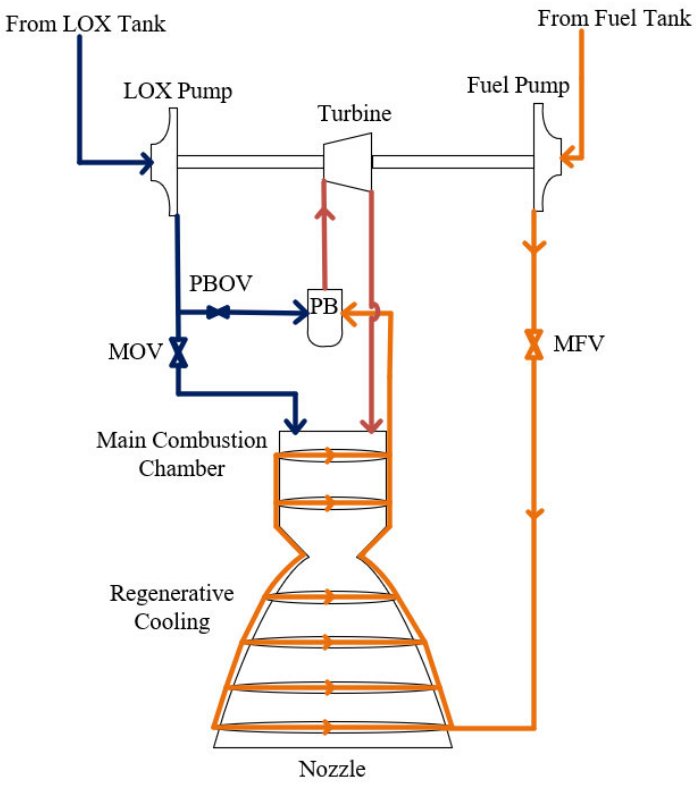

Figure 2-2: Staged combustion engine cycle

The staged cycle can either be oxidizer- or fuel-rich depending on which of the propellants flows entirely through the preburner (Law, 2022). When using fuels containing hydrocarbons like RP-1, soot within the exhaust gases can clog the injectors, reducing the performance and lifespan of the engine. The main advantages of the staged combustion cycle are higher propellant efficiency, reduced pumping pressure losses, and a higher chamber pressure resulting in a higher specific impulse and efficiency due to the propellant's increased temperature. Thus, smaller, lighter engines that produce the same thrust as the gas generator cycle can be built, with the staged cycle often used for high-power applications. The engineering complexity is, however, much greater than the other cycles requiring exotic materials for the plumbing and turbine. All the components are required to withstand high temperatures and pressures since partially burnt gases will flow through them to the combustion chamber. The higher discharge pressures of the cycle also require multistage pumps, which increases the engine's size and weight (Smyth, 2013). The exhaust gases are also at a much lower pressure than the combustion chamber, which can lead to undesirable backflow through the turbine and preburner if there is insufficient discharge pressure (Sutton and Biblarz, 2001). Additionally, since all the propellants pass through the turbine, the cycle is very sensitive to the turbine's efficiency, unlike the gas generator cycle. The cycle also requires complex control and feedback designs, resulting in longer manufacturing times, increased costs, and complex development processes (Aerospace Engineering, 2012).

2.1.3. Expander Cycle

The expander cycle is unique because it does not require a preburner or gas generator to generate the gases necessary to spin the turbine. Instead, the fuel or oxidizer is passed through the regenerative cooling channels of the rocket engine, where the heat in the cooling jackets is transferred to the cooler fluid (Sutton and Biblarz, 2001). The thermal transfer allows the fluid passing through the cooling channels to expand and change phase from a liquid to a gas. The heated and gaseous fuel vapor has a much larger nominal enthalpy and is fed through the turbine, spinning it, which drives the oxidizer and fuel turbopumps. The partially expanded fuel is then directed to the combustion chambers via the injector, where the primary combustion of the fuel and oxidizer occurs, generating the engine's thrust (ESA, 2017; Law, 2022). Figure 2-3 shows the expander engine cycle propellant flow path. Like the staged engine cycle, no gas is exhausted, with all the fuels burnt at an optimum mixture ratio in the combustion ratio, allowing for high specific impulse (Aerospace Engineering, 2012). The square cube law dictates that the nozzle's volume increases more than the available surface area for heat transfer, so the expander cycle engine's total thrust is limited, making the cycle appropriate for small to medium-sized engines (Smyth, 2013). Despite the limitations in thrust, the expander cycle offers significant advantages, including a significantly lower operating temperature since fuel gases are generated at room temperature, unlike the burnt gases of the gas generator and staged cycle, in which many exceed 1,000 K.

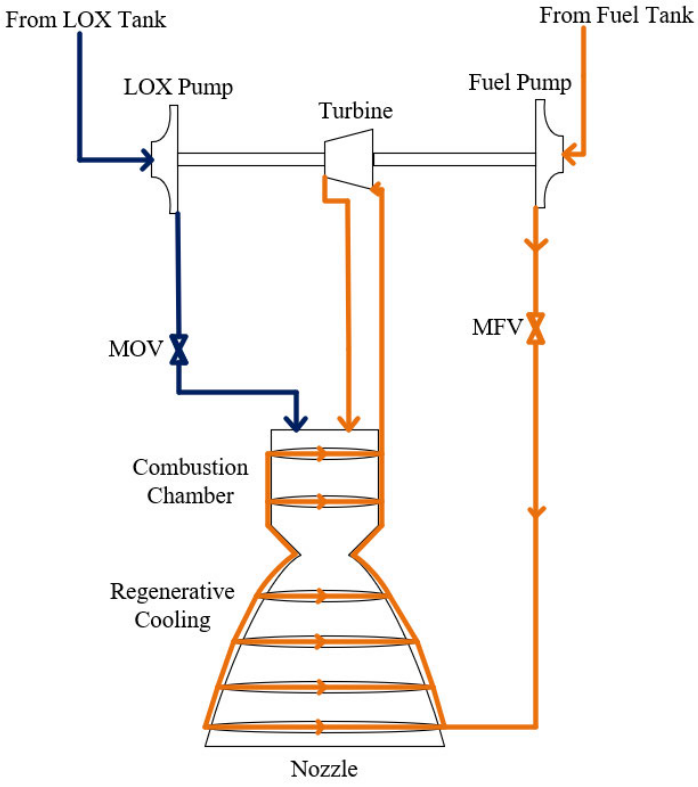

Figure 2-3: Expander cycle engine diagram

The cooler fuel gases mean the turbine runs cooler than the staged combustion and gas generator cycles, allowing for a much longer life, which has positive implications for the reusability of the engine. The lower operating temperature also means less exotic and expensive turbine and piping materials are required, reducing the overall material cost compared to the gas generator and staged rocket engine cycles. The start-up sequence is also much simpler than the staged and gas generator cycles due to the reduced number of subsystems and the cryogenic propellants freely expanding even before the heat source (Smyth, 2013). Thus, the engine can be restarted numerous times, sustain long burn times, and is most suitable for upper-stage engines. Since all the fuel passes through the turbine, the cycle is very sensitive to the turbine's efficiency, unlike the gas generator cycle. The expander cycle engines are also inherently expensive to design and manufacture. They mainly suit cryogenic fuels like liquid hydrogen, propane, and methane which can easily reach their boiling point, allowing for a large volume change, generating the pressure required to drive the turbine (ESA, 2017).

2.1.4. Electric Pump Fed Cycle

The electric pump-fed rocket engine cycle for small to medium-liquid rocket engine cycles has grown in popularity because of rapid developments in battery and electric motor technology. The newer technology significantly reduces the battery pack and motor sizes and weights while offering increased performance (Rachov and Tacca, 2010). The resulting electropump cycle is a bipropellant engine cycle that utilizes two electrically powered pumps to pressurize the fluid before the combustion chamber. All the propellants are used directly in the combustion chamber, unlike gas generators and staged engine cycles, which utilize a portion of the fuels to power a turbine. The electric pump cycle consists of fewer components than the gas generator, staged and expander cycles with the major components consisting of the DC battery pack, an inverter, fuel and oxidizer pumps, an electric motor, a controller, and the thrust chamber (Liu et al., 2021). Figure 2-4 shows the basic electropump engine cycle.

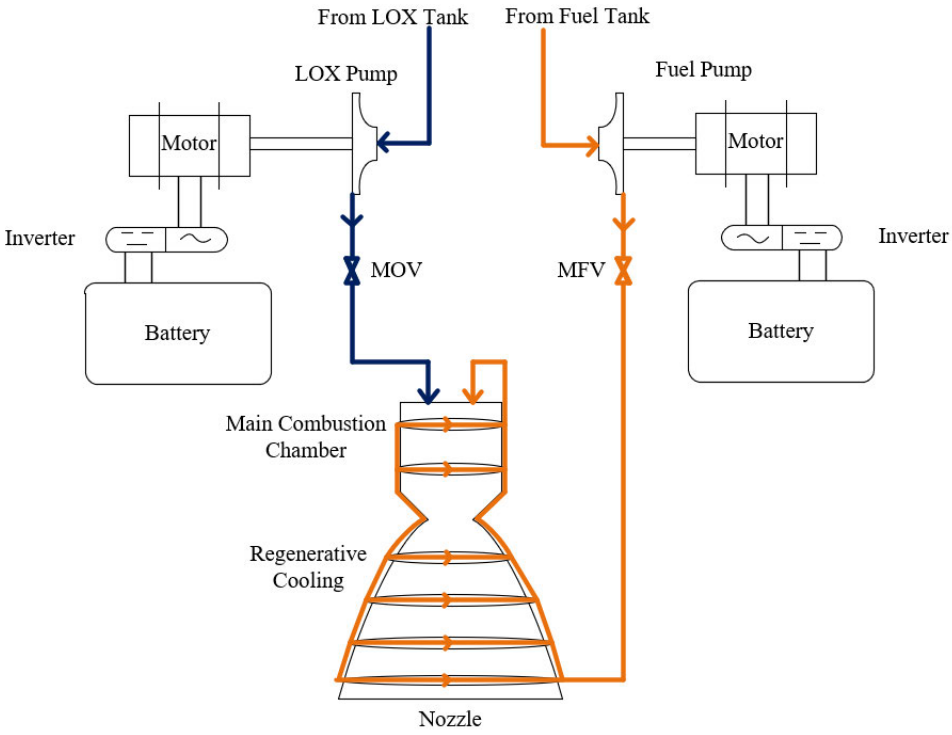

Figure 2-4: Electropump engine cycle with regenerative cooling

Unlike the conventional turbopump cycles, the electric pump-fed engine utilizes direct current from the battery packs, which is converted to alternating current via an inverter to a frequency suitable to drive the electric motor at the desired speed for the oxidizer and fuel pumps (Rachov and Tacca, 2010). The electropump assembly can be set up in a single-motor or dual-motor assembly. The single motor assembly utilizes one electric motor connected to the propellant pumps via a common shaft, rotating the fuel and oxidizer pumps at a constant speed. The dual shaft assembly utilizes separate inverter and electric motor assemblies for each propellant pump, allowing for the rotational speed to be varied. The electropump cycle offers the advantage of a simple and reliable design, a short R&D cycle, and a lower manufacturing cost. It can be easily throttled, started, or stopped, unlike the other cycles (Liu et al., 2021). One of the drawbacks of the electropump cycle is the dead weight of electric motors, batteries, and inverter, which is greater than the mass of the additional components needed for the other cycles when combined with the additional propellants needed to power the preburner or gas generator. Some dead weight can be overcome by hot-swapping the batteries, meaning that depleted batteries are ejected from the vehicle during the burn time.

2.1.5. Propellant Selection

The nominal fuel and oxidizer selected for the SAFFIRE engine are Rocket Propellant 1 (RP-1) and Liquid Oxygen (LOX). Despite RP-1 offering a lower specific impulse than the cryogenic options like liquid hydrogen, RP-1 is better suited for the SAFFIRE program since RP-1 can be easily transported and stored since it is stable at room temperature, presents a lower explosion and fire hazard and is

significantly cheaper and easier to acquire than cryogenic fuels like liquid hydrogen or liquid methane. RP-1 is also noncorrosive and is not carcinogenic, simplifying handling the fuel and allowing for cheaper and less exotic materials required for the storage tanks and the piping used within the rocket (Liu et al., 2021). LOX was selected as the oxidizer due to its good performance for the cost and availability of the fluid. Additionally, LOX is not carcinogenic, reducing the associated health and safety issues when working with the liquid. However, LOX is flammable and reactive and requires special safety precautions and clothing when working with the fluid. Due to its cryogenic nature, LOX requires unique exotic seals and materials. Most items, like steel tubing, become extremely brittle due to the low temperatures, with LOX boiling point of -183°C (Liu et al., 2021). Thus, custom storage tanks are required. Despite these issues, LOX offers the best performance, availability, safety, and cost-effectiveness compared to oxidizers like liquid fluorine or oxygen difluoride (Rachov and Tacca, 2010).

The propellant combination of RP-1 and LOX has good performance as it achieves an Ideal Specific Impulse of 344 s (Liu et al., 2021). The density of the fluids is also similar, with LOX at 1,142 kg/m^3 and RP-1 810-1,020 kg/$m^{3,}$ which significantly decreases the size and the mass of the tanks required. Unlike cryogenic fuels like liquid hydrogen, which have a significantly smaller density than RP-1, the propellant combination of RP-1 and LOX allows for a single shaft mechanical arrangement between the pumps, greatly decreasing engineering complexities, costs, weight, and manufacturing difficulty.

2.1.6. SAFFIRE Engine Cycle Selection

Since the SAFFIRE Program is focused on producing an affordable rocket engine that can be easily manufactured and operated with the finalized propellants, some liquid engine cycles are inappropriate for use. The expander cycle requires the fuel to be cryogenic to expand the gases to drive the turbine for the pumps. Since RP-1 is not cryogenic (boiling point of 210°C) like hydrogen (boiling point of -253°C), it does not allow for rapid expansion, and the expander cycle is not suitable for use in the SAFFIRE engine with the current propellant selection. The staged combustion cycle, while offering a higher specific impulse and overall efficiency compared to the electric pump and gas generator cycle, the engineering complexity, significantly high development cost, longer development time, and difficulty in manufacturing outweigh the advantages for the SAFFIRE Program. Thus, the staged combustion cycle is not suitable for use.

2.2. Engine Cooling Methods

During operation, rocket engines experience extreme thermal gradients, especially in the thrust chamber where the combustion of the rocket propellants occurs. Combustion temperatures range from 2,700 K to 3,600 K, significantly higher than most materials' melting points (Browne et al., 2020). As a result, it is necessary to implement a cooling system to reduce the temperatures of many engine components and prolong the engine's lifespan. Liquid rocket engines can feature one or more cooling methods,

including the regenerative, ablative, radiation, film, dump, and transpiration methods (Browne et al., 2020). Among these, regenerative and ablative are the most used methods and are the two cooling methods under consideration for the SAFFIRE engine.

2.2.1. Ablative Cooling

Ablative cooling utilizes a sacrificial liner to cool the engine through chemical reactions, which uses the enthalpy of vaporization to remove thermal energy from the system, protecting the inner layers from extreme conditions within the nozzle and combustion chamber (Browne et al., 2020). Figure 2-5 shows a schematic diagram of the ablative cooling method highlighting that the sacrificial ablative layer is bonded to the outer wall or overwrap of the rocket engine.

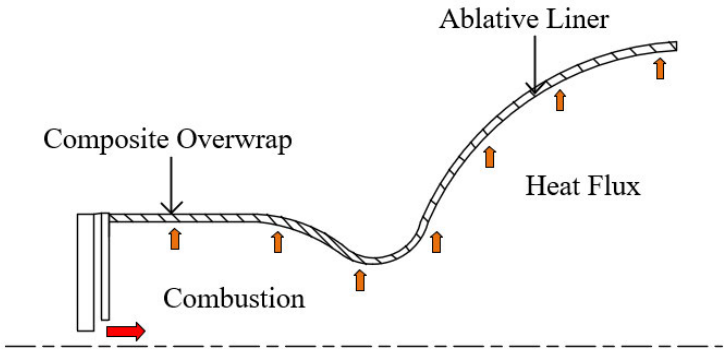

Figure 2-5: Ablative cooling schematic diagram

During use, the ablative material will continually absorb heat until its surface heats sufficiently and vaporizes, taking the heat with it. This prevents the temperatures from penetrating deeper into the engine component (Percival, 2022). The material used for the ablative layers can be characterized as pyrolyzing and non-pyrolyzing. When a non-pyrolyzing material like carbon or graphite is used, a large portion of the heat is reflected and re-radiated and does not go under any phase or mass changes during use. However, the non-pyrolyzing materials are temperature-limited and unsuitable for use in the thrust chamber (Harpale et al., 2018). Therefore, pyrolyzing materials are commonly used for the ablative layers as they can withstand a significantly higher working temperature through phase change and mass loss.

Pyrolyzing materials are usually composite materials consisting of a carbon or silica fiber matrix embedded with phenolic resin (Browne et al., 2020). When the composites are exposed to high temperatures, the resin absorbs the heat, which undergoes an endothermic degradation, leading to the material charging and ablating away, taking the energy away with it. The porous carbonaceous residue known as char also radiates heat and thermally insulates the layers of the ablative material below. Simultaneously, pyrolysis gas evaporates into the boundary layer, shifting the gas's hot, chemically

reactive shock layer away from the combustion chamber and nozzle walls. Thus, a transpiration cooling effect is created near the surface, adding additional cooling capabilities (Harpale et al., 2018). This method of cooling has no moving parts and is self-regulating, making it extremely reliable and efficient (Percival, 2022). However, because the ablative material is lost during use, the engine cannot be reused, and the material erosion can reduce the rocket engine's performance as the expansion ratio changes with time.

2.2.2. Regenerative Cooling

Regenerative cooling of a rocket engine necessitates the flow of the liquid propellants through a series of pipes or channels on the exterior surface of the rocket's nozzle and combustion chamber before passing through the injectors and entering the combustion chamber (Percival, 2022). As seen in Figure 2-6, the fuel or oxidizer is directed along the outside surface of the combustion chamber and nozzle through the channels or pipes.

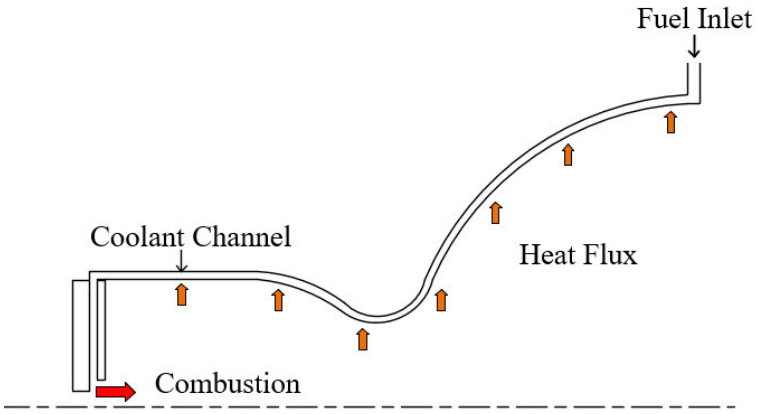

Figure 2-6: Regenerative cooling schematic diagram

The fluid acts as a heat exchanger as it absorbs thermal energy from the combustion through convective heat transfer, preventing the rocket engine from melting at high temperatures (Browne et al., 2020). During use, the propellants are preheated by thermal transfer, which increases the energy density of the fuel and can often lead to higher efficiency and more thrust. The materials between the channels or pipes also act as cooling fins and transfer heat from the engine to the atmosphere via conduction and radiation. Materials with high thermal conductivity, like copper or nickel alloys, are commonly used to increase thermal transfer (Percival, 2022). Fuel is often used as the cooling fluid. However, there are cases where it is more beneficial to use the oxidizer as the fuel does not have a large enough thermal conductivity or the mass flow rate is too low to remove sufficient heat from the engine (Browne et al., 2020).

One of the most significant drawbacks of the regenerative cooling is coking. This occurs from the deposition of soot by some of the rocket fuels used for cooling, leading to blockages in the cooling

channels. Regenerative cooling also requires large fluid inlet pressures to overcome the pressure drop associated with the cooling channels and to ensure adequate atomization of the propellants for complete combustion. Despite these issues, regenerative engines experience longer operational lives and are more efficient than ablatively cooled engines while also offering better reusability.

2.3. Electric Motor

In traditional pressure-fed rocket engine cycles, a gas turbine provides the torque required to drive the pump impellers using expanded hot gases. The hot gases are supplied to the turbine using various methods, including preburners and gas generators (Waxenegger-Wilfing et al., 2018). In electropump cycles, the electric motor replaces turbines by providing the necessary torque and power using converted electrical energy from a battery pack to supply propellant to the rocket engines.

In the case of a commercial launch vehicle platform, the electric motor must have high rotational speeds to generate the large, desired pressure and mass flow rates. The electric motors must achieve a range of 20,000-100,000 rpm with a power output upwards of 30 kW (Waxenegger-Wilfing et al., 2018). The motors used to power the pumps must also have a high-power density to reduce the mass of the components, making it a viable option to replace gas turbines.

Only one operational electric pump engine cycle is currently used in a commercial launch vehicle, namely the Rutherford engine. Designed and manufactured by Rocket Lab, it is used to propel the Electron, a small satellite launch vehicle. The Electron is a two-stage reusable rocket that uses a cluster configuration of nine Rutherford engines on the first stage and a single vacuum Rutherford engine for the second stage. The Electron is designed to place a 200 kg payload into a 500 km Sun-synchronous orbit (SSO) but can place 150 – 250 kg payloads to a 400 – 1,200 km SSO suitable for Cubesats and small payloads (Rocket Lab USA Inc., 2022). The proposed design of South Africa's CLV will follow the same rocket engine configuration for both stages and has a similar payload design condition of 200 kg for a 500 km SSO (Gyasi-Agyei, 2021). Thus, the Electron is an equivalent rocket for comparison of the electric pump feed cycle used in the SAFFIRE engine for CLV. Tables 2-1 and 2-2 list the booster stage engine properties of the Rutherford and SAFFIRE rocket engines.

Table 2-1: First-stage engine comparison between the Rutherford and SAFFIRE engines

	Rutherford Engine (Liu et al., 2021)	**SAFFIRE Rocket Engine** (Wunderlin, 2019)
Combustion Chamber Pressure	3 MPa	3.5 MPa
Vacuum Thrust	26 kN	30.1 kN
Sea Level Thrust	24 kN	27.6 kN
O/F Ratio	2.60	2.39

Table 2-2: First-stage engine comparison between the Rutherford and SAFFIRE engines continued

	Rutherford Engine (Liu et al., 2021)	**SAFFIRE Rocket Engine** (Wunderlin, 2019)
LOX Mass Flow Rate	5.65 kg/s	7.05 kg/s
Fuel Mass Flow Rate	2.17 kg/s	2.95 kg/s
Required LOX Pump Power	36.1 kW	50 kW
Required Fuel Pump Power	29.1 kW	35 kW
LOX Pump Rotational Speed	-	20,000 rpm
Fuel Pump Rotational Speed	-	33,400 rpm
Maximum Motor Speed	40,000 rpm	-
1st Stage Burn Time	150 s	164 s

The Rutherford engine uses dual three-phase brushless DC electric (BLDC) motors to power the fuel and oxidizer pumps, with each electric motor producing 37 kW at 40,000 rpm. A BLDC motor is considered a permanent magnet DC motor commutated electronically from rotor position feedback. Such a motor, therefore, uses power switches and not brushes like generic DC motors (Zhao and Yangwei, 2011). Three hall sensors or rotary encoders are attached to the motors to measure the position of the rotor and create the necessary feedback for speed control (Zhao and Yangwei, 2011).

BLDC motors have numerous advantages over brushed DC motors, AC induction motors, and permanent magnet synchronous motors (PMSM). According to Zhao and Yangwei (2011), they have a high operating efficiency (85 - 94%), superior speed vs torque characteristics, a more comprehensive operating speed range (1,500 – 100,000 rpm), reduced need for maintenance due to fewer components, a higher operating temperature, higher power densities and can be easily controlled using positioning feedback sensors (Gopal, 2020; Zhao and Yangwei, 2011). Table 2-1 shows that the Rutherford and SAFFIRE engines possess similar characteristics throughout, especially regarding the required power for the fuel and oxidizer pumps and operating speeds. Thus, with the advantages that BLDC motors offer above their counterparts and the viability of the BLDC motors proven from the numerous flights of Electron, the BLDC motors are considered a suitable choice for the SAFFIRE electropump system.

BLDC motors are coupled with an inverter to implement reverse movement, as they do not have any brushes or other mechanical contacts. With the use of the inverter circuitry, the voltage of each coil can be adjusted in addition to the current. The most common way to control the voltage is via pulse width modulation (PWM), as the voltage can be adjusted by varying the pulse length on time, known as duty time. An increase in the duty time allows for a corresponding increase in the voltage, and a decrease in the duty cycle decreases the voltage, adjusting the speed of the motor (Mohammad et al., 2017). The most common configuration for sequentially adjusting the voltage and current of each motor phase is to use an inverter with three pairs of MOSFETs arranged in a bridge structure, as seen in Figure 2-7.

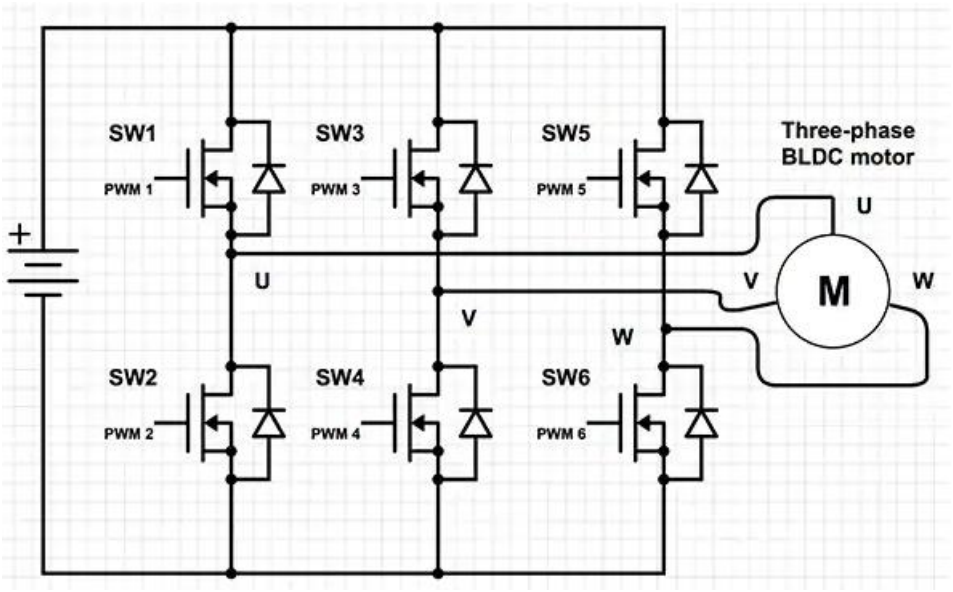

Figure 2-7: A three-phase BLDC motor MOSFET control system (Zhao and Yangwei, 2011)

The high-side MOSFETs receive a pulse-width modulation (PWM) voltage signal that converts the input DC voltage into a modulated driving voltage sent to the BLDC motors, controlling their speed. PWM allows precise control of the electric motor's speed and torque and enables an accurate start-up torque for the motors. The PWM MOSFET control system thus allows for relatively simple and accurate control of the speed of the electric motors used for the pumps (Lee and Kim, 2019).

2.4. Battery Pack

The battery pack is a crucial element of the electropump cycle as it is responsible for delivering the power to the motors and electronic systems of the vehicle and accounts for a substantial amount of the rocket's mass. The battery pack consists of numerous modules that contain battery cells wired together in series, parallel, or a combination of both, depending on the voltage, power, and current requirements (Vezzini, 2014). A cell is an energy storage medium comprising an anode, cathode, and electrolyte. When the batteries are connected to a closed circuit, an electron buildup begins, generating an electrical potential difference between the electrodes, providing power to the connected circuit (Odunlade, 2018). The battery pack also requires an internal battery management system (BMS). The BMS is a real-time control system that ensures correct and safe battery operation, monitors temperatures and voltages, and permits current performance optimization and failure prediction (Vezzini, 2014).

The most crucial parameters of the battery packs are the energy density and power density, as these define the mass and performance of the battery pack. Increasing energy or power densities makes more power available for a smaller mass. The engine's burn time determines which type of battery pack is the most suitable for use as it determines how long cells will be discharged and, thus, how much energy is required. The combustion chamber pressure also influences the pump power required. As the chamber pressure increases, there is a corresponding increase in pumping power, leading to a larger and heavier

battery requirement (Gyasi-Agyei, 2021). Thus, for the electropump cycle, the battery pack must have a high power and energy density cell to minimize the overall mass.

Figure 2-8 lists six existing battery types available on the current market. The cells are plotted in terms of energy density per liter on the vertical axis, which represents the size of the cell, and the energy density per kilogram on the horizontal axis, which represents the mass of the cells. From Figure 2-8, a good selection for the battery pack is lithium-ion (Li-ion) or lithium-ion polymer (PLiON or Li-Po) cells, as they have the highest energy in terms of mass and volume when compared to other safe and readily available battery options. Only lithium metal batteries offer higher energy and power density. Still, they are unstable, especially during charging, as they are plagued by lithium dendrite formation that leads to hazardous operation and a limited life span (Polinovel, 2022).

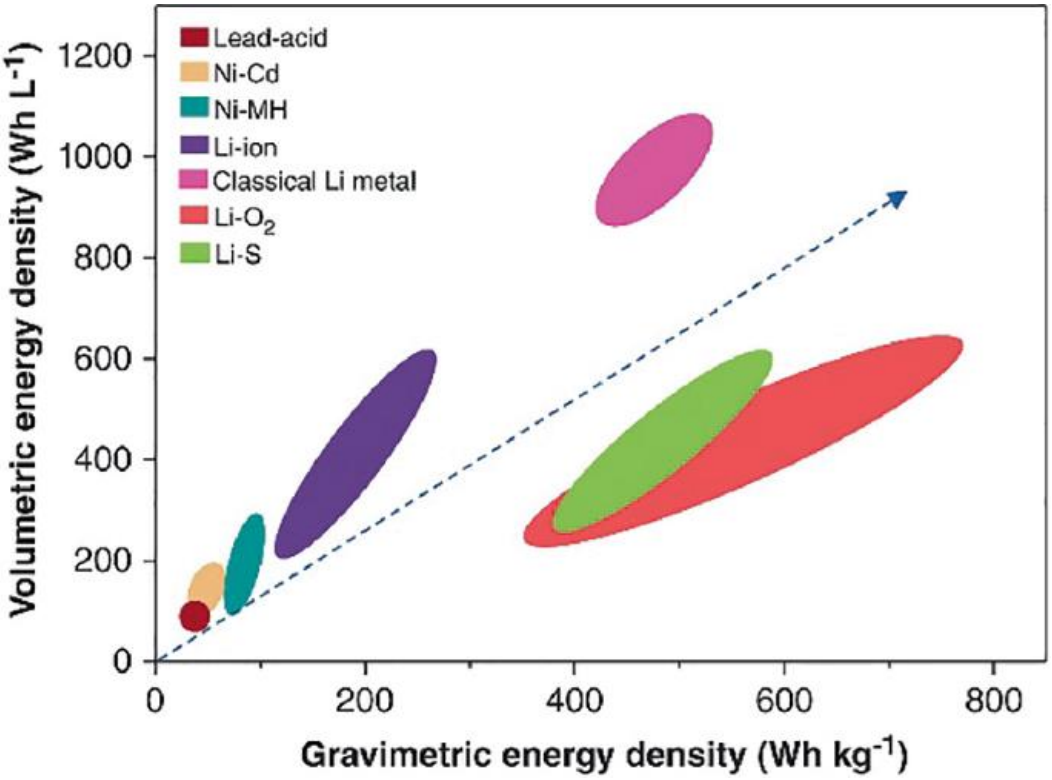

Figure 2-8: Energy density comparison of various batteries (Durakbasa, 2023)

Lithium-ion refers to a group of cells that use lithium as an anode mixed with a metal oxide representing the cathode. Lithium-ion batteries used cobalt dioxide (LCO), which initially was costly and had a poor lift span and safety rating. Over the years, lithium-ion batteries have greatly advanced in increased safety, cost reduction, and increased specific power and energy densities, as seen in Figure 2-9, the spider diagram that compares the six readily available lithium-ion batteries (Shepard, 2021). The six lithium batteries are Lithium Cobalt Oxide ($LiCoO_2$), Lithium-Ion Manganese Oxide (LMO), Lithium Iron Phosphate (LFP), Lithium Nickel Manganese Cobalt Oxide (NMC), Lithium Nickel Cobalt Aluminum Oxide (NCA), and Lithium Titanate (LTO).

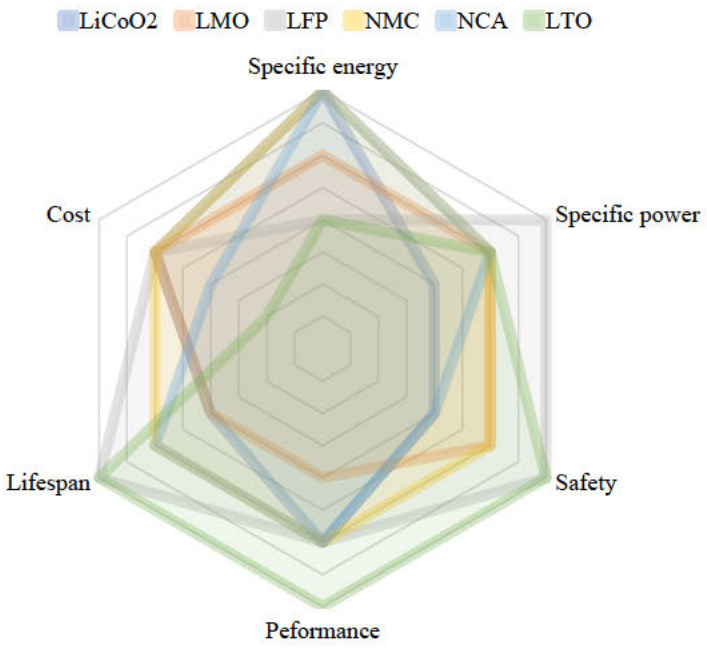

Figure 2-9: Performance comparison of lithium-ion chemistries

NMC batteries offer superior overall performance to other lithium-ion cells. NMC cells have varying elemental proportions in their chemical composition. This allows for a highly optimized and refined cell with excellent energy and power densities, low cost, good performance, safety, and reusability, making it one of the most successful lithium-ion batteries. They are commonly used in electric vehicles, power tools, and the medical field (Shepard, 2021).

Lithium-ion polymer (Li-Po) cells are similar in structure to lithium-ion cells, sharing the same lithium anode but with a polymer electrolyte instead of the conventional liquid electrolyte. Li-Po batteries offer higher specific energies than other lithium-ion batteries and have enhanced battery safety. They offer increased flexibility for use and are mostly used in systems where space and weight are crucial factors (Shepard, 2021).

When comparing the prices of battery packs, the Li-Po cells cost an additional 10 - 30% compared to Li-ion cells (Vashista, 2022). Li-Po batteries are more versatile as it is possible to manufacture them in a variety of shapes and sizes. They are also lighter and more robust than Li-Ion batteries due to their sturdy design and are less prone to leakage. Additionally, Li-Po batteries have a superior ability to maintain their full charging capacity. They are safer, hold fast charging, and possess a low self-discharge level, allowing the battery packs to be stored for long periods without losing a large amount of energy like lithium-ion cells. Li-Po batteries also use stacking technology compared to lithium-ion winding technology, allowing for more explosive energy and lower internal resistance (Lam, 2022).

An important factor to consider in battery selection for launch vehicles is the battery packs' operational time or duty cycle (Kwak et al., 2018). The proposed burn time for the first stage of the SAFFIRE rocket

engine is 164 seconds, and the second stage burn time is 236 seconds. Using the proposed burn times as the discharge time (t_d) a battery's current rate or C rate is defined in equation 2-1.

$$Current\ Rate = \frac{3600}{t_d} \tag{2-1}$$

This study selected an appropriate battery using the current rate related to the stage burn times. According to Kwak et al., (2018) the higher power density of the Li-Po batteries makes them better suited for rocket engine applications as they can discharge energy quicker than lithium-ion batteries and do not show any significant voltage drops for discharge times less than 400 s. Thus, Li-Po batteries are better suited to matching the motor's power and energy requirements to last the full burn time. Furthermore, the Rutherford engines used to power Rocket Lab's Electron launch vehicle, which is similar in size to the proposed design of CLV, use custom-manufactured Li-Po batteries to supply the energy and power required by the electric motors, confirming the viability of Li-Po Cells (Beck, 2019).

2.5. Modular Simulation Methods

The New Space era has led numerous private ventures to develop liquid propulsion systems. The timeline for designing them is generally lengthy, they are both expensive and complex. It has become increasingly important to evaluate different components and cycles as quickly as possible without ignoring the system complexities, as it is crucial to capture the interdependencies between components. Such simulations allow the designer and project managers to make effective decisions at the early stages of the engine and enhancement phase and enable validation before or after hot fire tests of rocket engines (Naderi and Liang, 2019).

Trying to simulate a large, interconnected model of the SAFFIRE engine using a 3D CFD model on a system scale would be computationally expensive and is not a viable option. A 1D-model also has the additional advantage of evaluating properties that cannot be addressed by a CFD code. Therefore, employing a suitable 1-dimensional model of the rocket engine system allows the user to predict and improve the system's performance in a predictive and repeatable manner with a lower computational cost and lead time (Naderi and Liang, 2019). Gore (1957) established a principal nonlinear dynamic model for bipropellant liquid rocket engines and used an analog computer for the simulations. A digital computer was later developed by Kluger (1958) that enabled the engine's pressure surges during engine start-up and shutdown to be studied using an interconnected modular system of liquid rocket engines. Goertz (1995) suggested a modular analysis method for liquid rocket engine cycles, noting that despite liquid rocket engines containing many components, many of these components are shared, such as the pump turbines, combustion chamber, and nozzle. It was then proposed that the rocket engine could be assembled using a predefined component library. A relatively small component library was found to be sufficient for a general analysis of the most complex rocket engine cycles. Numerous authors then adapted the modular method, most recently Naderi (2018). The space shuttle main rocket engine was

analyzed using the modular method under a steady-state environment using 14 interconnected modules found in MATLAB Simulink. According to Naderi and Liang (2019), the modular concept proved successful as it allowed for an easily understood model that can be easily adjusted while yielding accurate results. When comparing the simulation results to the Rocketdyne hot fire tests, there was a mean error of 3% to 7% when operating the engines at 109%, 100%, 60%, and 50% of the rated thrust level, proving that the simulation provides reasonable accuracy without having the long computational time and complexities of 3D CFD models of the entire system. Figure 2-10 shows the simulated flow diagram used by Naderi and Liang (2019) to perform the steady-state simulations of the space shuttle main engine (SSME). The diagram consisted of 14 components, axial pumps (AP), combustion chamber (CC), cooling jacket (CJ), centrifugal pumps (CP), fuel preburner (FP), fuel preburner valve (FPV), gas turbine (GT), hydraulic turbine (HT), main fuel valve (MFV), main oxidizer valve (MOV), nozzle performance (NP), oxidizer preburner valve (OPV), preburner (PB) and pipelines (PL).

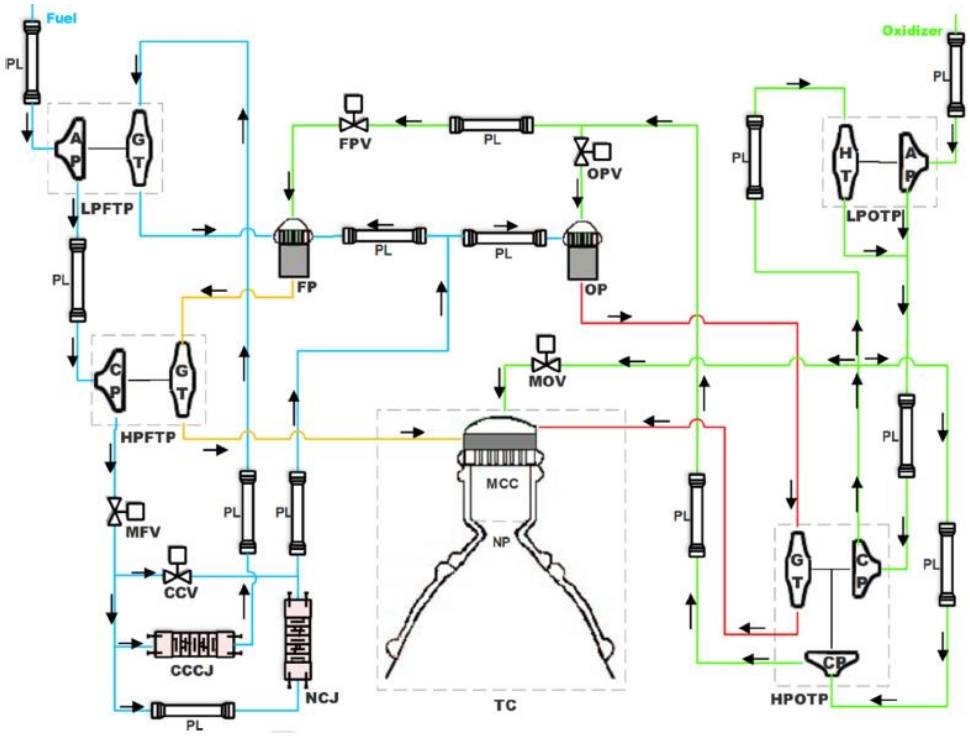

Figure 2-10: Simulated flow diagram of the SSME (Naderi and Liang, 2019)

In this study, the lumped modular method is adopted for the 1D models of the SAFFIRE rocket engine configurations, although some changes are made to adapt the model found in Figure 2-10 so as to match the gas generator and the electropump cycles. For the gas generator cycle, the fuel preburner valve (FPV) and the oxidizer preburner valve (OPV) are replaced by a gas generator fuel valve (GGFV) and gas generator oxidizer valve (GGOV), and the preburner and turbines are replaced by a gas generator and impulse turbine connected to two axial pumps for the oxidizer and fuel lines, forming the traditional turbopump. The electropump cycle features none of the preburner or turbine components and instead uses electric motors connected to two axial pumps using a mechanical shaft. Therefore, several

components, including the tanks, inverter, battery pack, the fuel and oxidizer pre valve, the fuel and oxidizer purge valves, and bleed or purge valves for both the propellants can be neglected from the simulated electropump and gas generator cycles.

2.6. Regenerative Convection Cooling

A regeneratively cooled thrust chamber design considers gas-side convective heat transfer and coolant-side convective heat transfer. It can be described as the heat transfer between two moving fluids through a multilayer partition. The sections below outline how each convective heat transfer coefficient is estimated using numerical methods.

2.6.1. Gas-Side Convective Cooling

One of the primary steps in designing a thrust chamber cooling system is analyzing the heat transfer from the combustion gases to the engine's chamber walls via forced convection. The heat transfer from the combustion gas to the coolant can be approximated as a one-dimensional flow that involves a combination of convection through multiple boundary layers. Along the side of the chamber's walls is a boundary layer of stagnant gas that the heat must pass through before heat energy can transfer to the wall (Huzel et al., 1992). The basic heat transfer equation to evaluate the heat flux is found in equation 2-2,

$$q = h_{\mathrm{g}}(T_{\mathrm{aw}} - T_{\mathrm{wg}}) \tag{2-2}$$

where q represents the rate of heat flux or total heat transferred across the stagnant layer, h_{g} is the gas-side heat transfer coefficient, T_{aw} represents the adiabatic wall temperature of the gas and T_{wg} is the gas side local chamber wall temperature.

The adiabatic wall temperature of the combustion gases at any given location of the combustion chamber can be evaluated using equation 2-3.

$$T_{\mathrm{aw}} = (T_{\mathrm{c}})_{\mathrm{ns}} \left[\frac{1 + r\left(\frac{\gamma - 1}{2}\right) M_{\mathrm{x}}^2}{1 + \left(\frac{\gamma - 1}{2}\right) M_{\mathrm{x}}^2} \right] \tag{2-3}$$

$$T_{\mathrm{aw}} = (T_{\mathrm{c}})_{\mathrm{ns}} H$$

Here, $(T_{\mathrm{c}})_{\mathrm{ns}}$ is the nozzle stagnation temperature, M_{x} is the local Mach number, r is the local recovery factor, γ is the specific heat ratio, and H is the effective recovery factor. The local recovery factor represents the ratio of frictional temperature increase to the increase caused by adiabatic compression. Since the flow in the combustion chamber can be assumed to be turbulent, equation 2-4 is used to evaluate the correction factor using the Prandtl number (Pr).

$$r = (Pr)^{0.33} \tag{2-4}$$

Adapted from Huzel et al., (1992), the Bartz Equation, shown in equation 2-5, can be used to estimate the forced convective heat transfer coefficient, which is commonly used to find the convective heat fluxes in rocket engines,

$$h_{gas} = \left[\frac{0{,}026}{D_{\mathrm{t}}^{0.2}}\left(\frac{\mu^{0.2}C_p}{pr^{0.6}}\right)\left(\frac{P_{\mathrm{c}}g}{c^*}\right)^{0.8}\left(\frac{D_{\mathrm{t}}}{R_{\mathrm{throatcurve}}}\right)^{0.1}\right]\left(\frac{A_{\boldsymbol{t}}}{A}\right)^{0.9}\sigma \tag{2-5}$$

where D_{t} is the throat diameter, μ is the dynamic viscosity of the exhaust gas, C_{p} is the specific heat at constant pressure, P_{c} is the chamber pressure, c^* is the characteristic velocity, $R_{\mathrm{throatcurve}}$ is the nozzle radius of curvature at the throat, A_{t} is the area of the throat, A is the area along the chamber axis, and σ is the correction factor for property variation across the boundary layer.

The Bartz Equation, while accurate for the rocket engine's throat and diverging section, reduces in accuracy in the combustion chamber since the assumption of fully developed flow is not justified upstream of the throat. In this case, it underpredicts the convective heat flux by approximately 8-10% (Huzel et al., 1992). In this study, the underestimation is disregarded to approximate the full convective heat transfer ratio, and the Bartz Equation is used to evaluate the forced gas side convection across the entire rocket engine.

The correction factor for property variation across the boundary layer (σ) can be evaluated in terms of nozzle stagnation temperature (T_{st}), local gas-side chamber wall temperature (T_{wg}) and local Mach Number (M_{a}) as seen in equation 2-6.

$$\sigma = \left[\left(\frac{T_{\mathrm{wg}}}{2T_{\mathrm{st}}}\right)\left(1+\frac{\gamma-1}{2}M_{\mathrm{a}}^2\right)+\frac{1}{2}\right]^{-0.68}\left(1+\frac{\gamma-1}{2}M_{\mathrm{a}}^2\right)^{-0.12} \tag{2-6}$$

As seen in Figure 2-11, there are existing graphs of σ plotted as a function of $\frac{T_{\mathrm{wg}}}{T_{\mathrm{st}}}$ and γ as computed by Bartz (Huzel et al., 1992).

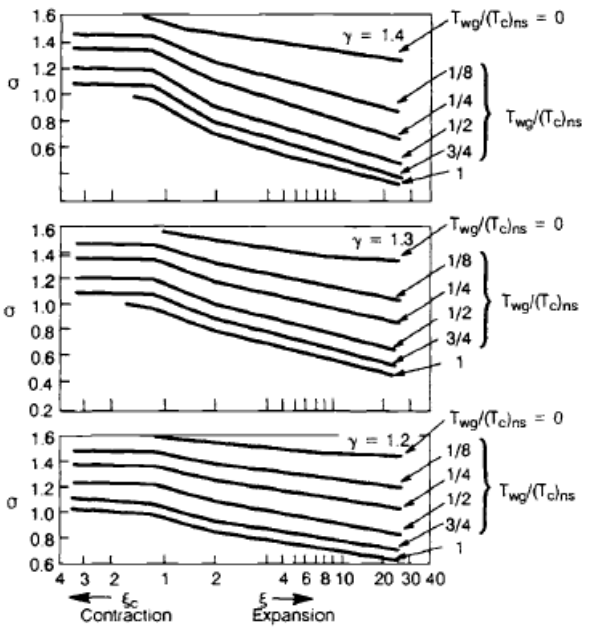

Figure 2-11: Correction Factor σ Across Boundary Layer (Huzel et al., 1992)

Therefore, since the specific heat ratio is approximately 1.2 for a Kerosene/LOX rocket engine, the lowest of the graphs can be used for the correction factor estimation (Huzel et al., 1992). If the Prandtl Number and viscosity of the combustion gas mixture are unavailable, they can be approximated using equations 2-7 and 2-8,

$$Pr = \frac{4\gamma}{9\gamma - 5} \tag{2-7}$$

$$\mu = (46.6 \times 10^{-10}) M^{0.5} T^{0.6} \tag{2-8}$$

where M is the molar mass of the gas mixture, and T is the temperature of the gas mixture.

2.6.2. Coolant-Side Heat Transfer

The coolant side heat transfer coefficient can be affected by numerous factors. The heat transfer coefficient (h_c) may decrease due to fouling deposits from the fluid that decrease the heat transfer efficiency due to a thin fouling layer generated on the surface. The propellant may decompose or deposit impurities upon the heated surface, reducing the cooling effectiveness. Furthermore, when the coolant pressures are sub-critical and the wall temperature exceeds the saturation temperature by a margin of 10 – 40 K, bubbles form within the coolant layer close to the wall. The bubbles grow outward into the cooler liquid stream until condensation at the vapor-to-liquid surface starts to exceed the vaporization rate at the bubbles' base and begin to collapse. The bubbles collapse at a high frequency called nucleate boiling and substantially increase the heat transfer coefficient, resulting in a small increase in the wall temperature for a wide range of heat flux. The further increase in the heat flux leads to a dense bubble

population that causes the bubbles to combine into a vapor film, leading to a sharp decrease in the heat-transfer coefficient. The resulting decrease in heat transfer increases the wall temperature, significantly increasing the probability of the wall material failing. An induced penalty of nucleate boiling is an increased pressure drop across the channel and a reduced mass flow rate, which can negatively affect the rocket engine's performance. It was assumed that the nucleate boiling did not affect the heat transfer coefficient and that the mass flow rates used remained constant.

No nucleate boiling can occur when the coolant is above the critical pressure, and wall temperatures increase with increasing heat flux. As the wall temperature gradually transitions to a stable supercritical vapor-film boundary layer, a slight decrease in heat transfer coefficients begins. Thus, according to Huzel et al., (1992), the regenerative cooling channels should operate between 0.3 and 0.7 of the critical pressure to take advantage of the high heat transfer coefficients available from nucleate boiling. It was assumed that an operating pressure of less than 0.3 of the critical pressure existed in the cooling channels to simplify the analysis and the estimation of the heat transfer coefficient. It is common for the coolant pressure in turbopump systems to be supercritical, resulting in a low chance of nucleate boiling. Thus, the convective heat transfer coefficient can be evaluated accurately using the Sieder-Tate equation for turbulent heat transfer in liquids flowing in channels shown in equation 2-9 (Huzel et al., 1992).

$$Nu = 0.0214 Re^{0.8} Pr^{0.4} \left(\frac{\mu}{\mu_{\mathrm{w}}}\right)^{0.14} \tag{2-9}$$

Here, Re is the Reynolds Number, μ is the coolant viscosity at bulk temperature, and μ_{w} is the coolant viscosity at the coolant sidewall temperature.

The convective heat transfer coefficient can be calculated using equation 2-10, which uses the Nusselt number from equation 2-9, the coolant thermal conductivity (k), and the hydraulic diameter of the channels (d).

$$h_c = \frac{Nu\ k}{d} \tag{2-10}$$

Equation 2-11 can be used to evaluate the coolant-side heat transfer coefficient when the heat is transferred through the vapor-film boundary layer.

$$h_c = \frac{0.029 C_{\mathrm{p}} \mu^{0.2}}{Pr^{\frac{2}{3}}} \left(\frac{G^{0.8}}{d^{0.2}}\right) \left(\frac{T_{\mathrm{co}}}{T_{\mathrm{wc}}}\right)^{0.55} \tag{2-11}$$

Here, G is the coolant mass flow rate per unit area, T_{co} is the coolant bulk temperature and T_{wc} is the coolant-side wall temperature. For calculating the final heat transfer coefficient, equation 2-10 and 2-11 are used simultaneously in an iterative manner to find the wall temperature until it balances, and a final convective heat transfer coefficient is found for the coolant-side.

3. Mass Evaluation of Engine Cycles

It is necessary to evaluate the principal components of the electropump and gas generator cycles to calculate a payload mass of a hypothetical launch vehicle for each engine configuration and, therefore, to identify which variation offers the best performance. Principal components common in each stage include the propellants, pressurizing gas, engines, propellant tanks, pressurizing gas tanks, thrust structures, and gimbals. Components unique to the first stage of the rocket include the intertank structures. In contrast, components unique to the second stage include the payload, the payload adaptor, fairings, interstage, reaction control systems, and the separation system. The equations used to evaluate the launch feed cycles and the structural components are adaptations from Kwak et al., (2018), Huzel et al., (1992), Akin, (2016) and Rachov and Tacca, (2010).

For the evaluation of the engine mass, only the regeneratively cooled engine is estimated using mass models as the SAFFIRE rocket engine injector, and the ablatively lined combustion chamber and nozzle are already manufactured and have known masses.

3.1. Gas Generator Cycle

The total mass of a two-stage CLV carrier rocket using the gas generator cycle (m_{ggc}) for both stages can be evaluated using equation 3-1. This consists of the masses of the most significant components, including the pressurant ($m_{\mathrm{pg1,2}}$), oxidizer ($m_{\mathrm{o1,2}}$), fuel ($m_{\mathrm{f1,2}}$), the propellants consumed by the turbine ($m_{\mathrm{ptu1,2}}$), oxidizer tank ($m_{\mathrm{ot1,2}}$), fuel tank ($m_{\mathrm{ft1,2}}$), pressurant tank ($m_{\mathrm{pt1,2}}$), the gas generator ($m_{\mathrm{gg1,2}}$), the turbopump ($m_{\mathrm{tp1,2}}$), and the turbine ($m_{\mathrm{tu1,2}}$). Structural components, including the thrust structures ($m_{\mathrm{ts1,2}}$), engines ($m_{\mathrm{en1,2}}$), the fairing (m_{fair}), the interstage (m_{is}), and gimbals ($m_{\mathrm{gim1,2}}$) are included. Additional components consisting of the wiring ($m_{\mathrm{wire1,2}}$), the avionics ($m_{\mathrm{avi1,2}}$), the residual propellant and pressurant ($m_{\mathrm{res1,2}}$), the plumbing ($m_{\mathrm{plum1,2}}$), the payload (m_{pl}) and the Reaction Control System (RCS) (m_{RCS}) are also included in the mass evaluation. Minor components like the mass of the valves, mountings, and controls were neglected due to the lack of information to estimate their masses for the analysis.

$$\begin{aligned} m_{\mathrm{ggc}} = {} & m_{\mathrm{pg1,2}} + m_{\mathrm{o1,2}} + m_{\mathrm{f1,2}} + m_{\mathrm{ptu1,2}} + m_{\mathrm{ot1,2}} + m_{\mathrm{ft1,2}} + m_{\mathrm{pt1,2}} \\ & + m_{\mathrm{gg1,2}} + m_{\mathrm{tp1,2}} + m_{\mathrm{tu1,2}} + m_{\mathrm{ts1,2}} + m_{\mathrm{en1,2}} + m_{\mathrm{fair}} + m_{\mathrm{is}} + m_{\mathrm{gim1,2}} \\ & + m_{\mathrm{wire1,2}} + m_{\mathrm{res1,2}} + m_{\mathrm{avi1,2}} + m_{\mathrm{plum1,2}} + m_{\mathrm{pl}} + m_{\mathrm{RCS}} \end{aligned} \tag{3-1}$$

3.1.1. Pressurizing Gas

The gas used for pressuring the oxidizer and fuel tanks to accommodate for the required pump inlet pressure can be approximated using the ideal gas law and assuming that there is negligible initial gas inside the pipes and propellant tanks and adiabatic expansion occurs (Rachov and Tacca, 2010). The pressurizing gas mass is estimated using equation 3-2,

$$m_{\mathrm{pg}} = \frac{p_{\mathrm{p}} V_{\mathrm{p}}}{R_{\mathrm{pg}} T_0} \left(\frac{\gamma_{\mathrm{pg}}}{1 - \frac{p_{\mathrm{pg}}}{p_0}} \right) \tag{3-2}$$

where, p_{p} is the propellant tank instantaneous pressure, V_{p} is the propellant volume, R_{pg} is the pressurizing gas constant, T_0 is the pressurizing gas initial temperature, γ_{pg} represents the pressurizing gas specific heat ratio, p_{pg} is the gas tank instantaneous pressure, and p_0 is the pressuring gas initial pressure respectively.

For the estimation of the pressurizing gas, it is assumed that there are no pipe pressure losses between the pressurizing tank and the propellant tank. The gas tank's instantaneous and initial pressures are the same. Comparing all pressures to the combustion chamber pressure is convenient for further calculations. Therefore, the following pressure ratio constant (K_{PR}), which relates the gas's instantaneous pressure to the combustion chamber pressure, is created and represented in equation 3-3,

$$K_{\mathrm{PR}} = \frac{p_{\mathrm{p}}}{p_{\mathrm{cc}}} = \frac{p_{\mathrm{pg}}}{p_{\mathrm{cc}}} \tag{3-3}$$

where p_{cc} represents the combustion chamber pressure.

In all propellant tanks, a small portion of the tank volume, called ullage, remains empty. It represents the necessary space for the propellant to expand thermally and allows the gases originally in liquid form to accumulate during storage (Sutton and Biblarz, 2001). To reduce the complexity of the mass analysis, an additional constant that relates the total tank volume to the propellant volume is introduced. The ullage constant (K_{ul}) is assumed to be the same for the fuel and oxidizer tanks and represented in equation 3-4.

$$K_{\mathrm{ul}} = \frac{V_{\mathrm{ft}}}{V_{\mathrm{f}}} = \frac{V_{\mathrm{ot}}}{V_{\mathrm{o}}} \tag{3-4}$$

Here, V_{ft}, represents the fuel tank volume, V_{f}, is the fuel volume, V_{ot} is the oxidizer tank volume, and V_{o} is the oxidizer volume, respectively.

The mass of the pressurizing gas depends on the type of gas used. It is useful to represent the gas constant (R_{pg}) in terms of the molar mass of the gas, as seen in equation 3-5.

$$R_{\mathrm{pg}} = \frac{R_{\mathrm{u}}}{M_{\mathrm{pg}}} \tag{3-5}$$

Here, R_{u} and M_{pg} represent the universal gas constant and the molar mass of the pressurizing gas.

The mass flow rates of the oxidizer ($\dot{m}_o$) and the fuel ($\dot{m}_{\mathrm{f}}$) in the oxidizer-to-fuel ratio can be separated into the product of the propellants' density ($\rho_{\mathrm{o}}/\rho_{\mathrm{f}}$) and the volumetric flow rate (Q) shown in equation 3-6.

$$O/_F = \frac{\dot{m}_\mathrm{o}}{\dot{m}_\mathrm{f}} = \frac{\rho_\mathrm{o} Q_\mathrm{o}}{\rho_\mathrm{f} Q_\mathrm{f}} \tag{3-6}$$

Thus, the relationship between the volume and mass of the oxidizer, fuel, and the total propellant can be represented using a propellant mass fraction as seen in equations 3-7 to 3-10,

$$Q_\mathrm{o} = \frac{O/_F}{\rho_\mathrm{o}} \left(\frac{1}{1 + O/_F} \right) \dot{m}_\mathrm{p} = \alpha_\mathrm{o} \dot{m}_\mathrm{p} \tag{3-7}$$

$$Q_\mathrm{f} = \frac{1}{\rho_\mathrm{f}} \left(\frac{1}{1 + O/_F} \right) \dot{m}_\mathrm{p} = \alpha_\mathrm{f} \dot{m}_\mathrm{p} \tag{3-8}$$

$$\alpha_\mathrm{o} + \alpha_\mathrm{f} = \alpha_\mathrm{t} \tag{3-9}$$

$$V_\mathrm{p} = V_\mathrm{o} + V_\mathrm{f} = \alpha_\mathrm{o} m_\mathrm{p} + \alpha_\mathrm{f} m_\mathrm{p} = \alpha_\mathrm{t} m_\mathrm{p} \tag{3-10}$$

where α_o, α_f and α_t represent the oxidizer, fuel, and total propellant mass fractions relating the volumetric flow rate to the mass flow rate, respectively.

Equation 3-11 represents a simplified estimation of the pressurant gas created by substituting the new constants and ratios generated in equations 3-3 to 3-10 into equation 3-2. An additional component (K_g) was added to the pressurant mass to account for the residual gases in the tank and pipelines.

$$m_\mathrm{PG} = K_\mathrm{g} K_\mathrm{PR} K_\mathrm{ul} \gamma_\mathrm{pg} \alpha_\mathrm{t} \frac{1}{R_\mathrm{pg} T_0} \left(\frac{m_\mathrm{p} p_\mathrm{cc}}{1 - K_\mathrm{PR} \frac{p_\mathrm{cc}}{p_0}} \right) \tag{3-11}$$

3.1.2. Propellant Masses

The propellant mass for each stage of the launch vehicle is directly proportional to the fuel or oxidizer mass flow rates, the burn time (t_b) for each stage, and a constant (K_prop), which represents the residual oxidizer and fuel left in the tanks, pumps, and piping after the burn time is complete. Equations 3-12 and 3-13 represent the oxidizer and fuel masses.

$$m_\mathrm{o} = K_\mathrm{propo} \dot{m}_\mathrm{o} t_\mathrm{b} \tag{3-12}$$

$$m_\mathrm{f} = K_\mathrm{propf} \dot{m}_\mathrm{f} t_\mathrm{b} \tag{3-13}$$

3.1.3. Oxidizer and Fuel Tanks

The propellant storage vessels were split into subcomponents depending on their shape to determine their masses. The proposed oxidizer and fuel tank used for CLV are cylindrical with hemispherical end caps. Thus, the tank is split into two components: the end caps and the cylindrical section. The tank mass depends on the wall thickness. Therefore, the minimum wall thickness that can withstand tank pressurization must be found. Two separate calculations for the minimum wall thickness are completed for each tank section. Equations 3-14 and 3-15 are used to calculate the minimum thickness for the cylindrical (e_{cyl}) and hemispherical (e_{hemi}) sections. The thickness of the cylindrical section consists of the product of the internal pressure (p) and the tank's inner radius (r_{i}) divided by the product of the allowable stress (Y) and the weld joint efficiency (E). The allowable stress is calculated by dividing the tank material's yield stress by a safety factor. According to Modlin and Zipay (2014), the United States aerospace industry has employed an ultimate safety factor of 1.5 since the 1930s. Still, there have been cases where a lower safety factor of 1.4 was employed, for example, the Boening X-20 Dyna-Solar lifting body test. However, for space flight applications, a safety factor of 1.1 is employed to reduce mass.

$$e_{\mathrm{cyl}} = \frac{p r_{\mathrm{i}}}{YE} \tag{3-14}$$

Equation 3-15 incorporates a stress factor (K_{s}) representing the reduction in stress over a spherical surface compared to a flat area (Gyasi-Agyei, 2021).

$$e_{\mathrm{hemi}} = \frac{p r_{\mathrm{i}} K_{\mathrm{s}} + \frac{1}{2}}{2YE} \tag{3-15}$$

Equation 3-16 represents the maximum thickness found using equations 3-14 and 3-15 which are used for the mass evaluation of the mass analysis of the oxidizer and fuel tank.

$$e = max(\, e_{\mathrm{cyl}}, e_{\mathrm{hemi}}) \tag{3-16}$$

Equations 3-17 and 3-18 represent formulas used to find the mass of the cylindrical section (m_{cyl}) and the hemispherical end caps (m_{hemi}),

$$m_{\mathrm{cyl}} = \pi l \rho [r_{\mathrm{o}}^2 - (r_{\mathrm{o}} - e)^2] \tag{3-17}$$

$$m_{\mathrm{hemi}} = \frac{4}{3} \pi \rho [r_{\mathrm{o}}^3 - (r_{\mathrm{o}} - e)^3] \tag{3-18}$$

where, l is the cylindrical length, ρ is the tank material's density, r_o is the tank's outer diameter, and e is the tank's wall thickness.

The total mass of the fuel tank and the oxidizer tank is the sum of the cylindrical and ellipsoidal sections for the total tank mass, which is found using equation 3-19.

$$m_{ft/ot} = m_{\text{cyl}} + m_{\text{hemi}} \tag{3-19}$$

3.1.4. Pressurant Tank

Spherical tanks are proposed to store the pressurant for both stages of CLV as they are stress-resilient shapes and can withstand the high initial pressure (Huzel et al., 1992). The first step in calculating the pressurant tank mass is calculating the minimum pressurant tank wall thickness (e_{pt}) using equation 3-20.

$$e_{\text{pt}} = \frac{pr_{\text{o}}}{2YE} \tag{3-20}$$

Here, r_{o} is the outer diameter of the tank.

The surface area of the tank (SA_{pt}) is required for the mass evaluation and can be found using equation 3-21.

$$SA_{\text{pt}} = 4\pi r_{\text{o}}^2 \tag{3-21}$$

Finally, the mass of the pressurant tank is evaluated using equation 3-22,

$$m_{\text{pt}} = \rho_{\text{pt}} SA_{\text{pt}} e_{\text{pt}} \tag{3-22}$$

where, ρ_{pt} is the density of the material used to manufacture the tank.

3.1.5. Turbopump

Assuming that there are no mechanical losses between the oxidizer and fuel pumps and turbine, the total turbopump power (P_{tp}) equals the sum of the power consumed by the oxidizer pump (P_{opu}), and fuel pump power (P_{fpu}), which is the same as the power generated by the turbine (P_{tu}) represented in equation 3-23 and equation 3-24.

$$P_{\text{tp}} = P_{\text{pu}} = P_{\text{tu}} \tag{3-23}$$

$$P_{\text{tp}} = P_{\text{pu}} = P_{\text{opu}} + P_{\text{fpu}} \tag{3-24}$$

Here, P_{pu} is the total pump power.

The amount of power consumed by the pump is directly proportional to the product of the head rise across the pump (Δp), the mass flow rate through the pump, and inversely proportional to the product of the density of the fluid and the pump efficiency ($\eta_{\text{opu}}/\eta_{\text{fpu}}$) as seen in equation 3-25.

$$P_{\mathrm{pu}} = \frac{\Delta p_{\mathrm{opu}} \dot{m}_{\mathrm{o}}}{\rho_{\mathrm{o}} \eta_{\mathrm{opu}}} + \frac{\Delta p_{\mathrm{fpu}} \dot{m}_{\mathrm{f}}}{\rho_{\mathrm{f}} \eta_{\mathrm{fpu}}} \tag{3-25}$$

The head rise across the pumps can be estimated as the sum of the chamber pressure (p_{cc}) and injector pressure drop (Δp_{inj}) subtracted by the initial tank pressure (p_{p}) as seen in equation 3-26.

$$\Delta p_{\mathrm{op}} \approx \Delta p_{\mathrm{fp}} = p_{\mathrm{cc}} + \Delta p_{\mathrm{inj}} - p_{\mathrm{p}} \tag{3-26}$$

A constant representing the injector pressure drop (K_{pi}) is shown in equation 3-27 to reduce the complexity of the mass analysis of the pump power and further calculations.

$$K_{\mathrm{pi}} = \frac{\Delta p_{\mathrm{i}}}{p_{\mathrm{c}}} \tag{3-27}$$

As a merit factor, the pump power density (δ_{pu}) is defined in equation 3-28 for the evaluation of the pump masses and is represented as the power divided by the total pump mass (m_{pu}).

$$\delta_{\mathrm{pu}} = \frac{P_{\mathrm{pu}}}{m_{\mathrm{pu}}} \tag{3-28}$$

Thus, the approximate mass of the turbopump assembly is found by using equation 3-29, which sums the power consumed by the oxidizer and fuel pumps and then divides by the energy density of the turbopump assembly (δ_{tp}).

$$m_{\mathrm{tp}} = \frac{P_{\mathrm{tp}}}{\delta_{\mathrm{tp}}} = \frac{P_{\mathrm{pu}}}{\delta_{\mathrm{tp}}} = \frac{1}{\delta_{\mathrm{tp}}} (P_{\mathrm{opu}} + P_{\mathrm{fpu}}) \tag{3-29}$$

3.1.6. Gas Generator

The mass of the gas generator is based on the internal volume (V_{gg}) and wall thickness (e_{gg}). Assuming that the gas generator is spherical and adopts the stay time method used by Rachov and Tacca, (2010), the gas generator volume is estimated using equation 3-30,

$$V_{\mathrm{gg}} = \frac{t_{\mathrm{s}} m_{\mathrm{ptu}}}{t_{\mathrm{b}} \rho_{\mathrm{gg}}} \tag{3-30}$$

where t_{s} is the stay time, m_{ptu} is the mass of propellant consumed by the gas generator, t_{b} is the burn time, and ρ_{gg} is the density of the exhaust gas generator gases, respectively.

The inner radius of the gas generator (r_{gg}) is approximated using equation 3-31, which represents the volume of a sphere.

$$V_{\mathrm{gg}} = \frac{4}{3} \pi r_{\mathrm{gg}}^3 \tag{3-31}$$

The mass of the gas generator is estimated using equation 3-32 consisting of the ratio of the gas generator wall material density (ρ_{tgg}) to the materials yield stress (σ_{gg}), multiplied by the wall thickness safety factor (K_{gg}), the gas generator combustion pressure (p_{gg}), the inner radius, and the volume of the gas generator.

$$m_{\mathrm{gg}} = \frac{\rho_{\mathrm{tgg}}}{2\sigma_{\mathrm{gg}}} K_{\mathrm{gg}} p_{\mathrm{gg}} r_{\mathrm{gg}} 4\pi \left(\frac{3V_{\mathrm{gg}}}{4\pi}\right)^{\frac{2}{3}} \tag{3-32}$$

3.1.7. Turbine Mass

It is necessary to define pump efficiency (η_{pu}) due to power losses from heat dissipation, noise, and mechanical losses, by relating the total power consumed by the propellant pumps to the power delivered by the turbine to the total output power of the turbine (P_{otu}) as seen in equation 3-33.

$$\eta_{\mathrm{pu}} = \frac{P_{\mathrm{pu}}}{P_{\mathrm{otu}}} \tag{3-33}$$

The total turbine power and the turbine energy density merit factor (δ_{tu}) can be used to find the mass of the turbine shown in equation 3-34.

$$\delta_{\mathrm{tu}} = \frac{P_{\mathrm{otu}}}{m_{\mathrm{tu}}} \tag{3-34}$$

Since the power losses of each pump are required to be included, the pumping power of each pump is divided by the pump's efficiency, as seen in equation 3-35.

$$m_{\mathrm{tu}} = \left(\frac{P_{\mathrm{fpu}}}{\eta_{\mathrm{fpu}}} + \frac{P_{\mathrm{opu}}}{\eta_{\mathrm{opu}}}\right) \frac{1}{\delta_{\mathrm{tu}}} \tag{3-35}$$

Replacing the power values with the preceding power formula found in equation 3-25 and utilizing the predefined constants and propellant mass fractions, equation 3-35 can be converted to be independent of the pumping power, as seen in equation 3-36.

$$m_{\mathrm{tu}} = \left(1 + K_{\mathrm{pi}} - K_{\mathrm{pr}}\right) \frac{p_{\mathrm{cc}} m_{\mathrm{p}}}{t_{\mathrm{b}}} \left(\frac{\alpha_{\mathrm{f}}}{\eta_{\mathrm{fpu}}} + \frac{\alpha_{\mathrm{o}}}{\eta_{\mathrm{opu}}}\right) \frac{1}{\delta_{\mathrm{tu}}} \tag{3-36}$$

3.1.8. Propellant Consumed by Turbine

For the gas generator cycle operation, a small portion of the fuel and oxidizer is tapped off from the main feed lines and directed to the engine's gas generator. Consequently, the mass of the additional propellant used for the gas generator must be included in estimating the engine cycle rocket mass. The mass analysis starts by defining the turbine efficiency. The efficiency is defined by the ratio of the total turbine output power to the turbine inlet power (P_{itu}) as seen in equation 3-37.

$$\eta_{\mathrm{tu}} = \frac{P_{\mathrm{otu}}}{P_{\mathrm{itu}}} \tag{3-37}$$

The turbine inlet power is related to the thermal expansion of the gases expelled from the gas generator in the turbine and is calculated using equation 3-38,

$$P_{\mathrm{itu}} = \frac{m_{\mathrm{ptu}}}{2t_{\mathrm{b}}} v_{\mathrm{gg}}^2 \tag{3-38}$$

where, v_{gg} is the velocity of the gases that enter the turbine and m_{ptu} is the mass consumed by the turbine. Under the assumption that the gases that impel the turbine undergo an isentropic expansion, the gas velocity can be estimated using equation 3-39,

$$v_{\mathrm{gg}}^2 = \frac{2\gamma_{\mathrm{gg}}}{\gamma_{\mathrm{gg}} - 1} R_{\mathrm{gg}} T_{\mathrm{itu}} \left(1 - \left(\frac{p_{\mathrm{dtu}}}{p_{\mathrm{itu}}} \right)^{\frac{\gamma_{\mathrm{gg}}-1}{\gamma_{\mathrm{gg}}}} \right) \tag{3-39}$$

where γ_{gg}, R_{gg}, T_{itu}, p_{dtu}, and p_{itu} represent the gas generator exhaust gas specific heat ratio, the turbine drive gas constant, the turbine inlet temperature, and the pressure downstream and upstream of the turbine, respectively.

Using equations 3-36 to 3-39, the turbine output power can be estimated using the gas generator exhaust gas parameters as shown in equation 3-40.

$$P_{\mathrm{otu}} = \frac{\eta_{\mathrm{tu}} m_{\mathrm{ptu}} \gamma_{\mathrm{gg}} R_{\mathrm{gg}} T_{\mathrm{itu}}}{t_{\mathrm{b}}(\gamma_{\mathrm{gg}} - 1)} \left(1 - \left(\frac{p_{\mathrm{dtu}}}{p_{\mathrm{itu}}} \right)^{\frac{\gamma_{\mathrm{gg}}-1}{\gamma_{\mathrm{gg}}}} \right) \tag{3-40}$$

Finally, the mass of the propellants consumed by the turbine can be estimated by combining equations 3-40 and 3-24 to form equation 3-41.

$$m_{\mathrm{ptu}} = (1 + K_{\mathrm{pi}} - K_{\mathrm{p}}) \frac{p_{\mathrm{c}} m_{\mathrm{p}}}{\eta_{\mathrm{tu}}} \times \left(\frac{\alpha_{\mathrm{f}}}{\eta_{\mathrm{fpu}}} + \frac{\alpha_{\mathrm{o}}}{\eta_{\mathrm{opu}}} \right) \frac{(\gamma_{\mathrm{gg}} - 1)}{R_{\mathrm{gg}} \gamma_{\mathrm{gg}}} \left(T_{\mathrm{itu}} \left(1 - \left(\frac{p_{\mathrm{dtu}}}{p_{\mathrm{itu}}} \right)^{\frac{\gamma_{\mathrm{gg}}-1}{\gamma_{\mathrm{gg}}}} \right) \right)^{-1} \tag{3-41}$$

3.2. Electric Pump Fed Cycle

The total mass of the electropump cycle (m_{ep}) is evaluated in the same manner as the gas generator cycle, with the exception being that the gas generator mass components like the turbopump, turbine, and gas generator are replaced by electrical components consisting of the battery pack (m_{ba}), the inverter (m_{inv}), electric motors (m_{em}), oxidizer pumps (m_{opu}) and fuel pumps (m_{fpu}). The total mass

of South Africa's two-stage CLV using the electropump cycle for both stages is represented by equation 3-42.

$$m_{\mathrm{ep}} = m_{\mathrm{pg1,2}} + m_{\mathrm{o1,2}} + m_{\mathrm{f1,2}} + m_{\mathrm{ot1,2}} + m_{\mathrm{ft1,2}} + m_{\mathrm{pt1,2}} + m_{\mathrm{opu1,2}} + m_{\mathrm{fpu1,2}} + m_{\mathrm{em1,2}} + m_{\mathrm{inv1,2}} + m_{\mathrm{ba1,2}} + m_{\mathrm{ts1,2}} + m_{\mathrm{en1,2}} + m_{\mathrm{wire1,2}} + m_{\mathrm{avi1,2}} + m_{\mathrm{gim1,2}} + m_{\mathrm{res1,2}} + m_{\mathrm{plum1,2}} + m_{\mathrm{pl}} + m_{\mathrm{fair}} + m_{\mathrm{is}} + m_{\mathrm{RCS}} \quad (3\text{-}42)$$

3.2.1. Pump Masses

The masses of each propellant pump can be expressed using equations 3-43 and 3-44 by introducing pump power densities for the oxidizer pump (δ_{opu}) and the fuel pump (δ_{fpu}) and utilizing the required pump power.

$$m_{\mathrm{opu}} = \frac{P_{\mathrm{opu}}}{\delta_{\mathrm{opu}}} = \frac{1}{\delta_{\mathrm{opu}}}\left(\frac{\Delta p_{\mathrm{opu}} \dot{m}_{\mathrm{o}}}{\rho_{\mathrm{o}} \eta_{\mathrm{opu}}}\right) \quad (3\text{-}43)$$

$$m_{\mathrm{fpu}} = \frac{P_{\mathrm{fpu}}}{\delta_{\mathrm{fpu}}} = \frac{1}{\delta_{\mathrm{fpu}}}\left(\frac{\Delta p_{\mathrm{fpu}} \dot{m}_{\mathrm{f}}}{\rho_{\mathrm{f}} \eta_{\mathrm{fpu}}}\right) \quad (3\text{-}44)$$

3.2.2. Electric Motor

The mass evaluation of the electric motor begins with equation 3-45, where the inlet pump power and the output pumping power of the electric motors (P_{em}) is used to define the efficiency of the pumps (η_{pu}).

$$\eta_{\mathrm{pu}} = \frac{P_{\mathrm{pu}}}{P_{\mathrm{em}}} \quad (3\text{-}45)$$

An electric motor's energy density (δ_{em}) is then defined using the output power and the mass of the electric motors, as seen in equation 3-46.

$$\delta_{\mathrm{em}} = \frac{P_{\mathrm{em}}}{m_{\mathrm{em}}} \quad (3\text{-}46)$$

The total work required by the pumps is found for both pumps using the pump efficiency. By summing the power required for each pump and rearranging the energy density equation, the mass of the electric motors can be evaluated using equation 3-47.

$$m_{\mathrm{em}} = \left(\frac{P_{\mathrm{fpu}}}{\eta_{\mathrm{fpu}}} + \frac{P_{\mathrm{opu}}}{\eta_{\mathrm{opu}}}\right)\frac{1}{\delta_{\mathrm{em}}} \quad (3\text{-}47)$$

3.2.3. Inverter

The evaluation of the inverter mass begins with calculating the efficiency of the electric motors (η_{em}) by finding the ratio of the power consumed by the electric motors to the total power supplied by the inverter (P_{inv}) as seen in equation 3-48.

$$\eta_{\mathrm{em}} = \frac{P_{\mathrm{em}}}{P_{\mathrm{inv}}} \tag{3-48}$$

Thus, the energy density of the inverter (δ_{inv}) and the power supplied by the inverter, represented by the power consumed by the motors divided by the motor efficiency, is used to evaluate the mass of the inverter shown in equation 3-49.

$$m_{\mathrm{inv}} = \frac{P_{\mathrm{inv}}}{\delta_{\mathrm{inv}}} = \frac{1}{\delta_{\mathrm{inv}}\eta_{\mathrm{em}}}\left(\frac{P_{\mathrm{fpu}}}{\eta_{\mathrm{fpu}}} + \frac{P_{\mathrm{opu}}}{\eta_{\mathrm{opu}}}\right) \tag{3-49}$$

3.2.4. Battery Pack

A battery pack has two limiting factors, namely, the power density and the energy density. The final battery pack mass depends on which factor yields the highest mass. Equations 3-50 and 3-51 define the power and energy densities, respectively.

$$\delta_{\mathrm{ba,po}} = \frac{P_{\mathrm{ba}}}{m_{\mathrm{ba}}} \tag{3-50}$$

$$\delta_{\mathrm{ba,en}} = \frac{t_{\mathrm{b}} P_{\mathrm{ba}}}{m_{\mathrm{ba}}} \tag{3-51}$$

For shorter burn times, having a battery pack with a higher power density is more favorable, while longer burn times require more energy, thus a higher energy density. The mass of a power-constrained battery pack ($m_{\mathrm{ba,po}}$) is based on the power the battery pack requires and is evaluated using equation 3-52.

$$m_{\mathrm{ba,po}} = K_{\mathrm{bp}} \frac{\left(P_{\mathrm{opu}} + P_{\mathrm{fpu}}\right)}{\eta_{\mathrm{inv}}\eta_{\mathrm{em}}\delta_{\mathrm{ba,po}}} \tag{3-52}$$

Here, K_{bp} is a structural margin to account for subcomponent masses of the battery pack, consisting of wiring, a battery management system, and the housing of the batteries.

The mass of an energy-constrained battery pack ($m_{\mathrm{ba,en}}$) is based on the battery pack's energy and is evaluated using equation 3-53.

$$m_{\mathrm{ba,en}} = K_{\mathrm{bp}} \frac{(P_{\mathrm{opu}} + P_{\mathrm{fpu}})(t_{\mathrm{b}})}{\eta_{\mathrm{E}} \eta_{\mathrm{inv}} \eta_{\mathrm{em}} \delta_{\mathrm{ba,en}}} \tag{3-53}$$

Here η_{E} is the battery energy efficiency.

The final mass estimation of the battery pack mass is determined by which factor yields the greatest value represented using equation 3-54.

$$m_{\mathrm{ba}} = max(m_{\mathrm{ba,po}}, m_{\mathrm{ba,en}}) \tag{3-54}$$

3.3. Structural Elements

Several structural elements require approximation to determine CLV's mass. The components listed below are shared components for the gas generator and the electropump cycle. The list of equations of the structural elements was adapted from Akin, (2016) and Huzel et al., (1992).

3.3.1. Thrust Structures

The mass of the thrust structures of each rocket engine can be evaluated using equation 3-55 adapted from Akin, (2016), which is dependent on the output thrust (F) of the rocket engine at sea level.

$$m_{\mathrm{ts}} = 2.55 \times 10^{-4}(F) \tag{3-55}$$

3.3.2. Gimbles

The estimated mass of the gimble depends on the rocket engine's thrust and the combustion chamber pressure (Akin, 2016). It is evaluated using equation 3-56.

$$m_{gim} = 237.8\left(\frac{F}{p_{\mathrm{cc}}}\right) \tag{3-56}$$

3.3.3. Pump Fed Rocket Engine

A pump-fed rocket engine consists of four major components: the injector, the combustion chamber, the nozzle, and the cooling system. Huzel et al., (1992) identified that the mass of the sum of these components representing the engine mass is calculated using equation 3-57.

$$m_{\mathrm{en}} = 7.81 \times 10^{-4}(F) + 3.37 \times 10^{-5}(F)\left(\sqrt{\epsilon}\right) \tag{3-57}$$

Here, ϵ is the expansion ratio of the nozzle, which is the exit area of the nozzle divided by the area of the throat.

3.3.4. Fairings and Interstage

Akin, (2016) found that the fairing mass and interstage mass depend on the area of the preliminary fairing and interstage design and are approximated using equations 3-58 and 3-59.

$$m_{\mathrm{fair}} = 4.95(A_{\mathrm{fair}})^{1.15} \tag{3-58}$$

$$m_{\text{is}} = 4.95(A_{\text{is}})^{1.15} \tag{3-59}$$

3.3.5. Avionics

According to Akin, (2016), the avionics mass depends on the total propellant mass (m_{p}) and is estimated using equation 3-60.

$$m_{\text{avi}} = 10\left(m_{\text{p}}\right)^{.361} \tag{3-60}$$

3.3.6. Wiring

The mass of the wiring for each rocket stage is calculated and depends on the total propellant mass and the proposed length (l) of the wiring required, as seen in equation 3-61.

$$m_{\text{wire}} = 1.058\sqrt{m_{\text{p}}}l \tag{3-61}$$

4. Simulation Methodology

4.1. Overview of Flownex®

Flownex® is an integrated one-dimensional Computational Fluid Dynamics (CFD) software for designing, simulating, and optimizing thermal fluid systems. It uses a network approach in which the built-in Flownex® flow modules are modeled as elements and nodes. Elements consist of but are not limited to pipes, pumps, valves, turbomachines, heat exchangers, and other thermo-hydraulic components. Nodes are the endpoints of each element. Figure 4-1 shows the layout of a Flownex® element with nodes.

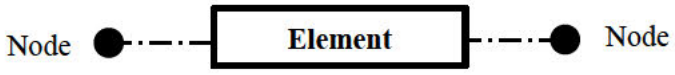

Figure 4-1: Example of Flownex® element and node

The elements can be connected arbitrarily at the nodes to form a network, which is then solved using the implicit solution algorithm. The Flownex® implicit solution algorithm is robust and accurate with the resemblance of a conventional CFD code. The system is discretized into several spatial control volumes with conservation equations (mass, energy, and momentum) to solve for flow, temperature, and pressure at each node in any user-defined system of components.

Flownex® is capable of modeling steady-state and transient event sequences, compressible and incompressible flow, laminar and turbulent flow conductive, convective, and radiative heat transfer, thermal capacitance, heat exchangers, turbo machinery, and reactors. It is used in many industries, including the mining, aircraft, and power generation industries, with rapid growth in the space industry with large operations, including Blue Origin, Foosung, and AEROSUD, utilizing the software (Leander, 2021).

4.2. Assumptions and Simplifications

Each rocket engine configuration was split into seven major components to create the SAFFIRE models and the two validation models. These components comprised the boundary conditions for the inlet and the outlet, the turbopump, the electropump, the injector, the gas generator and combustion chamber, the nozzle, and the regenerative cooling. The simulations are conducted in a steady state environment, allowing the propellant tanks, bleed valves, check valves, purge valves, the battery packs and inverters, and the ignition system of the rocket engines to be neglected from the simulation as they do not impact the performance of the outputs of the rocket engine. Furthermore, since the length of the plumbing of the SAFFIRE rocket engines is undecided, it was neglected from the simulation and replaced with a flow resistance element from Flownex® that can replicate the pressure losses of the pipes without the finalized length and diameters of the plumbing.

4.3. Flownex® First Stage Engine Models Inputs

The following sections discuss how the Flownex® models of the first-stage SAFFIRE rocket engines are modeled using the library elements within the simulation software. The design parameters of the SAFFIRE rocket engine cycle models and additional assumptions, where applicable, are also included under each section of the rocket engine.

4.3.1. Boundary Conditions

For each rocket engine cycle, an inlet and outlet boundary condition is required, with the inlet boundaries representing the exit from the fuel and oxidizer tanks and the exit boundary condition representing the exit conditions at the nozzle exit. The boundary conditions are kept constant for each SAFFIRE rocket engine simulation. Table 4-1 displays the inlet boundary conditions used for the simulations.

Table 4-1: Inlet boundary conditions for each simulation

Boundary Condition	Value	Unit
RP-1 Inlet Temperature	294.65	K
RP-1 Inlet Pressure	250	kPa
Oxidizer Inlet Temperature	85.15	K
Oxidizer Inlet Pressure	250	kPa

Figure 4-2 shows the boundary conditions of each engine configuration using Flownex® elements. For the RP-1 and LOX inlet conditions, the boundary node represented by the gauge was connected to a flow resistance element, representing the piping between the tanks and the inlet to the rocket engine pumps.

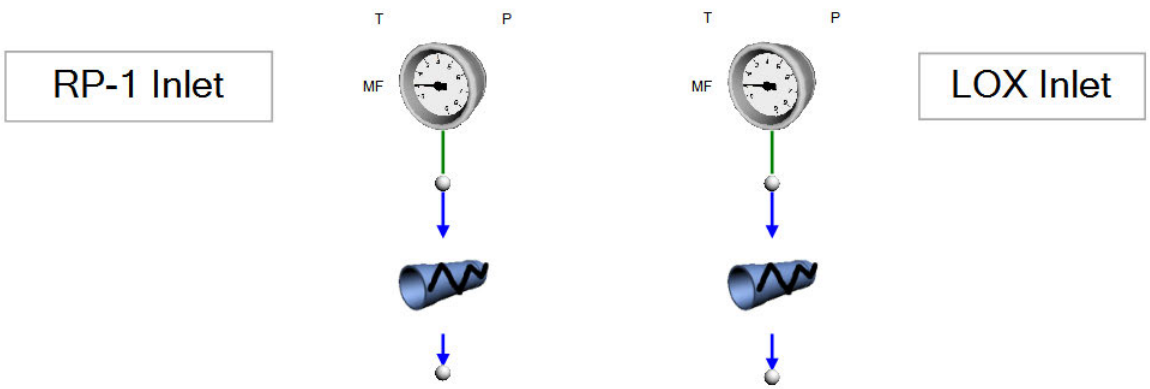

Figure 4-2: Flownex® Inlet Boundary Conditions for Each Engine Configuration

Three different exit boundary pressures are required for the simulations of the SAFFIRE engines: atmospheric pressure, optimum exit pressure, and vacuum pressure. Table 4-2 displays the exit boundary conditions for the three exit pressure variations.

Table 4-2: Exit boundary conditions for each simulation

Boundary Condition	Value	Unit
Sea Level Exit Pressure	101.325	kPa
Optimum Exit Pressure for Ablative Engine	53.36	kPa
Optimum Exit Pressure for Regenerative Engine	57.21	kPa
Vacuum Exit Pressure	0	kPa

The regeneratively cooled engine utilized a smaller expansion ratio and had a different optimum exit pressure, as seen in Table 4-2. Figure 4-3 represents the element configuration for the exit boundary condition for each engine configuration. The exit boundary node was connected after the exit thrust nozzle to represent the pressure at the nozzle exit.

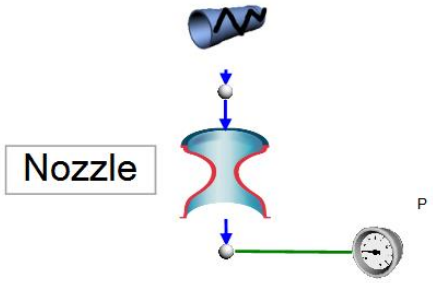

Figure 4-3: Flownex® exit boundary condition for each engine cycle

4.3.2. Turbopump

The turbopump of the SAFFIRE rocket engine was modeled using two centrifugal pumps that represent the oxidizer and the fuel pumps for each engine. Each pump inlet and outlet is connected to an upstream and a downstream node of flow resistance elements representing the upstream and downstream plumbing. Data links are used to connect the two pumps to a common shaft to ensure the pumps have the same operational speed. A turbine was placed after the gas generator and connected to the same shaft as the two pumps using a data link, completing the turbopump assembly. The turbine is responsible for supplying the required amount of power to the pumps and is driven by the high-pressure gases supplied by the gas generator. Figure 4-4 shows the turbopump configuration created in Flownex® using the library elements.

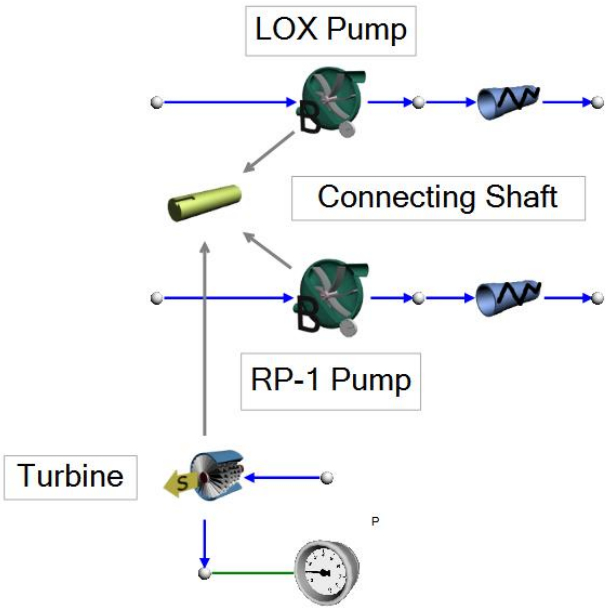

Figure 4-4: Flownex® turbopump configuration

The fuel and oxidizer pumps required a set mass flow rate, pump head at best efficiency point (BEP), and the volumetric flow rate at BEP to generate an approximate pump curve since the turbopump curves are not available for this study. The mass flow rates are also larger than the set oxidizer and fuel flow rates of 7.05 kg/s and 2.95 kg/s, as they include the additional 0.3 kg/s of propellant consumed by the gas generator. The centrifugal pump inputs for the oxidizer and the fuel are listed in Table 4-3, including the fuel pump head value for regenerative cooling. Due to the additional pressure drops in the regenerative cooling methods compared to the ablatively cooled engine, the fuel pump head increases to account for the increased losses.

Table 4-3: Turbopump input variables

Centrifugal Pump	Value	Unit
Rotational Speed	22,000	rpm
Fuel Mass Flow Rate	3.16	kg/s
Fuel Pump Head at BEP	526.81	m
Fuel Volume Flow at BEP	0.0040	m^3/s
Regeneratively Cooled Fuel Pump Head at BEP	568.40	m
Oxidizer Mass Flow Rate	7.14	kg/s
Oxidizer Pump Head at BEP	348.22	m
Oxidizer Volume Flow at BEP	0.0061	m^3/s

The turbine is responsible for supplying the required power to the pumps and is driven via the hot, high-pressure gases from the gas generators. The Ellipse-Law was used to find the turbine output parameters,

which required inlet variables consisting of the turbine inlet conditions and the mass fraction of the combusted gas from the gas generator to calculate the losses, efficiency, and power output (Leander, 2021). Table 4-4 provides the input parameters of the simple turbine used for the ablative and the regeneratively cooled engines.

Table 4-4: Turbine input conditions

Turbine	Value	Unit
Design Inlet Pressure	250	kPa
Design Inlet Temperature	1,123.15	K
Design Pressure Ratio	10	-
Design Mass Flow Rate	0.3	kg/s
Methane Mass Fraction	0.61	-
Carbon Monoxide Mass Fraction	0.17	-
Carbon Dioxide Mass Fraction	0.057	-
Hydrogen Mass Fraction	0.053	-
Water Mass Fraction	0.11	-

4.3.3. Electropump

The electropump utilizes electric motors to supply the torque to rotate the pumps at the optimum speed. Unlike the turbopump configuration, the fuel and oxidizer pumps are operated at different speeds and require separate electric motors. The design consists of two centrifugal pumps used for the fuel and oxidizer pumps connected to the electric motors using a mechanical shaft and data links to link the elements. Figure 4-5 represents the electropump configuration created in Flownex® using the library components.

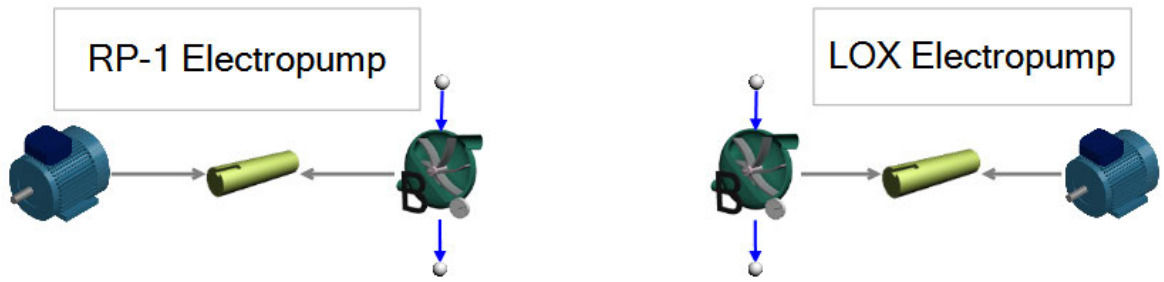

Figure 4-5: Flownex® electropump configuration

The input variables for the pumps are the same as the turbopump and consist of a fixed mass flow rate, the pump head at BEP, and the volumetric flow rate at BEP. An additional pump head value is included for the regeneratively cooled electropump cycle due to the increase in pump head from the additional

pressure drop of the regenerative cooling system. Table 4-5 contains the input conditions for the fuel and oxidizer pumps.

Table 4-5: Electropump input variables

Centrifugal Pump	Value	Unit
Fuel Pump Speed at BEP	33,400	rpm
Fuel Mass Flow Rate	2.95	kg/s
Fuel Pump Head at BEP	526.53	m
Fuel Volume flow at BEP	0.0037	m^3/s
Regeneratively Cooled Fuel Pump Head at BEP	567.93	m
Oxidizer Pump Speed at BEP	17,400	rpm
Oxidizer Mass Flow Rate	7.05	kg/s
Oxidizer Pump Head at BEP	353.08	m
Oxidizer Volume flow at BEP	0.0061	m^3/s

4.3.4. Gas Generator and Main Combustion Chamber

The Flownex® gas generator model comprises three main components: the inlet valves, the injector, and the chamber. The inlet valves are modeled using the basic valve element in Flownex® and are used to control the flow of the propellants and replicate the pressure drop across the valves. The injector is represented by a restrictor with a discharge coefficient in conjunction with Flownex's flow interface nodes, which converts the fluid into a gaseous state, representing the atomization of the propellants after passing through the injector. A boundary condition is added on each primary flow interface node for accurate atomization of the propellants. The boundary node and the data transfer link from the secondary node are responsible for maintaining the temperature and mass fraction when converting the propellants from a fluid into a gaseous state.

The gas generator and combustion process were modeled using a series of flow resistances and an adiabatic flame defined by NASA CEA (Leander, 2021). The flow resistances were used to model the combustion chamber walls and pressure losses. The CEA adiabatic flame element calculates the off-gas composition and the combustion temperature for the chemical reaction of a chemical mixture using a NASA-Glenn Chemical Equilibrium Program CEA2, a secondary software running in the background of Flownex®. Figure 4-6 shows the subassembly that represents the gas generator.

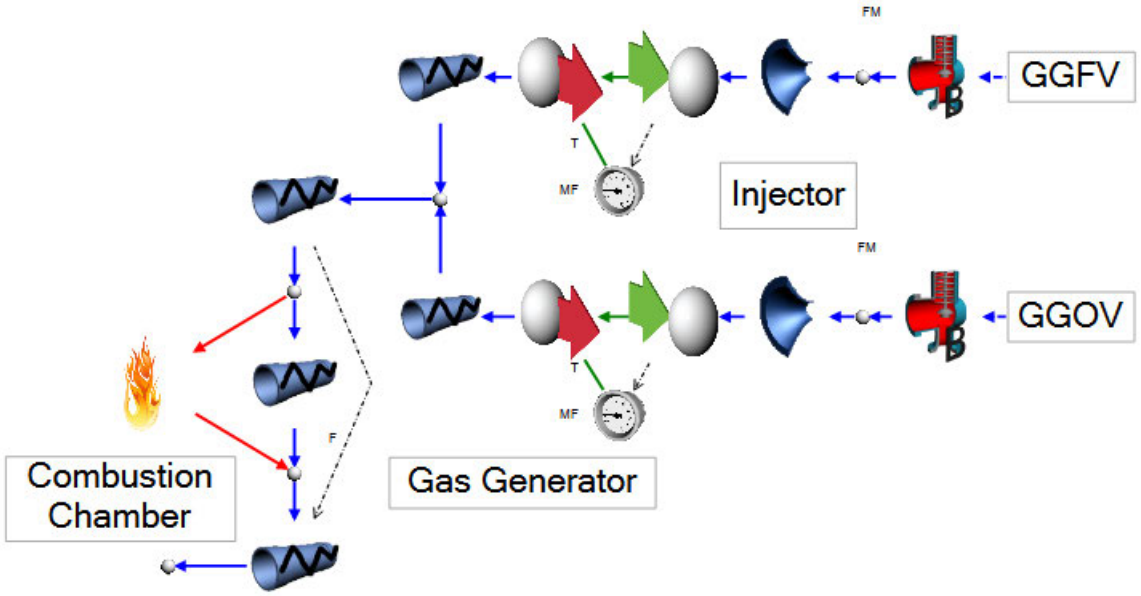

Figure 4-6: Flownex® subassembly of the gas generator

The basic valve data consists of the valve diameter, the valve coefficient (C_v) at the maximum opening, the fraction opening, and the number in parallel. Table 4-6 displays the inlet parameters for the basic valves that represent the GGFV and the GGOV.

Table 4-6: Gas generator valve input parameters

Basic Valve	Value	Unit
Fuel Valve Diameter	0.325	in
Fuel Valve Coefficient	0.93	-
Fuel Valve Fraction Opening	1	-
Number in Parallel	1	-
Oxidizer Valve Diameter	0.325	in
Oxidizer Valve Coefficient	0.060	-
Oxidizer Valve Fraction Opening	1	-
Number in Parallel	1	-

The restrictor input parameters for the gas generator fuel and oxidizer injector consist of the diameter of the orifices, the discharge coefficient, the number in parallel, and the opening percentage. The input conditions for the fuel injector are given in Table 4-7.

Table 4-7: Gas generator fuel restrictor input parameters

Fuel Restrictor	Value	Unit
Orifice Diameter	1.8	mm
Discharge Coefficient	0.86	-
Number of Orifices	20	-
Opening Percentage	100	-

Table 4-8 shows the restrictor inputs for the oxidizer injector orifices.

Table 4-8: Gas generator oxidizer restrictor input parameters

Oxidizer Restrictor	Value	Unit
Orifice Diameter	2	mm
Discharge Coefficient	0.77	-
Number of Orifices	10	-
Opening Percentage	100	-

To model the gas generator combustion chamber, resistance data, including the flow admittance, the admittance factor, and the percentage opening, were required for the flow resistance elements. The input values for the parameters are found in Table 4-9.

Table 4-9: Flow resistance input parameters

Flow Resistance	Value	Unit
Flow Admittance	0.1	-
Admittance Scaling Factor	1	-
Percentage Opening	100	%

The main combustion chamber was modeled using the same methodology as the gas generator in Flownex®, with the only difference being the input parameters for the fuel and oxidizer injectors. Figure 4-7 illustrates the main combustion chamber subassembly created in Flownex® using the library elements.

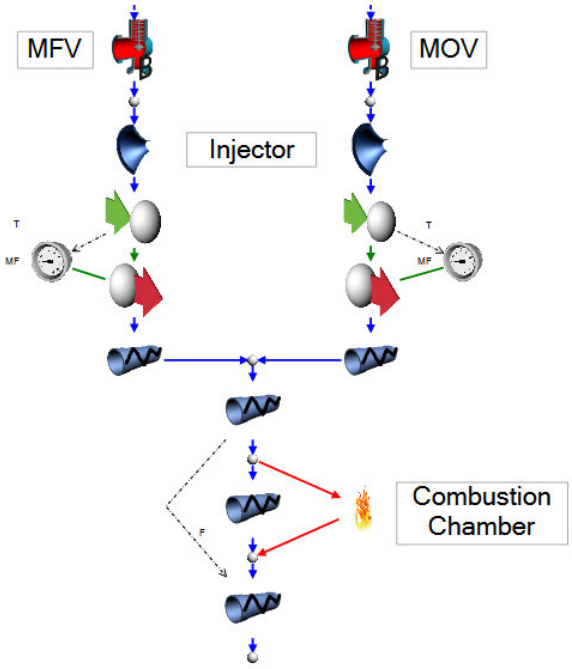

Figure 4-7: Flownex® subassembly of the main combustion chamber

Table 4-10 contains the basic valve input data for the MFV and MOV for the main combustion chamber.

Table 4-10: Main combustion chamber valve input parameters

Basic Valve	Value	Unit
Fuel Valve Diameter	1	in
Fuel Valve Coefficient	8.66	-
Fuel Valve Fraction Opening	1	-
Number in Parallel	1	-
Oxidizer Valve Diameter	1	in
Oxidizer Valve Coefficient	18.85	-
Oxidizer Valve Fraction Opening	1	-
Number in Parallel	1	-

Table 4-11 displays the input values for the fuel injector of the combustion chamber.

Table 4-11: Combustion chamber fuel restrictor input parameters

Fuel Restrictor	Value	Unit
Orifice Diameter	1.8	mm
Discharge Coefficient	0.78	-
Number of Orifices	40	-
Opening Percentage	100	-

Table 4-12 contains the input parameters for the oxidizer injector.

Table 4-12: Combustion chamber oxidizer restrictor input parameters

Oxidizer Restrictor	Value	Unit
Orifice Diameter	2	mm
Discharge Coefficient	0.77	-
Number of Orifices	80	-
Opening Percentage	100	-

4.3.5. Nozzle

The nozzle of the rocket engine accelerates the high-pressure gases from the combustion chamber, generating the thrust necessary to propel the rocket. An exit thrust nozzle is used to model the SAFFIRE nozzle in Flownex®. Figure 4-3 contains the exit thrust nozzle used for each rocket engine configuration. It consists of a converging and diverging section and can model subsonic and supersonic flow at the outlet of a flow network. The calculations are based on the nozzle's throat and outlet area, a momentum correction factor, and the assumption that the flow is adiabatic. The momentum correction factor, (λ), is based on the cone half angle, (α), and is calculated using equation 4-1.

$$\lambda = \frac{1}{2}(1 + cos\ \alpha) \tag{4-1}$$

The first stage SAFFIRE rocket engine had a cone half angle of 15°, resulting in a momentum correction factor of 98.3%.

The SAFFIRE regeneratively cooled engine has a smaller expansion ratio of 10.5 compared to the ablatively cooled engine, which has an expansion ratio of 13. The smaller expansion ratio was used to ensure that the rocket engine was cooled without the fuel changing phase before entering the injectors. Thus, the ablatively and regeneratively cooled engines have differing exit diameters due to the change in expansion ratios. The input values for the exit thrust nozzle of the first-stage SAFFIRE ablative and regenerative engines are displayed in Table 4-13.

Table 4-13: Exit thrust nozzle input parameters

Exit Thrust Nozzle	Value	Unit
Throat Diameter	80.5	mm
Ablative Engine Exit Diameter	294.3	mm
Regenerative Engine Exit Diameter	260.85	mm
Momentum Correction Factor	0.98	-

4.3.6. Regenerative Cooling

The regenerative cooling method requires that the liquid propellants flow through a series of pipes or channels on the exterior surface of the rocket's nozzle and combustion chamber to remove heat from the system. This is modeled using the composite heat transfer element in Flownex®. The elements can model conduction, convection, and radiative heat transfer. One composite heat transfer element is connected to one of three pipe elements used to represent the regenerative cooling channel lengths of the combustion chamber, the converging section, and the diverging section of the nozzle. Figure 4-8 shows the layout of the regenerative cooling system created in Flownex® for both feed cycles.

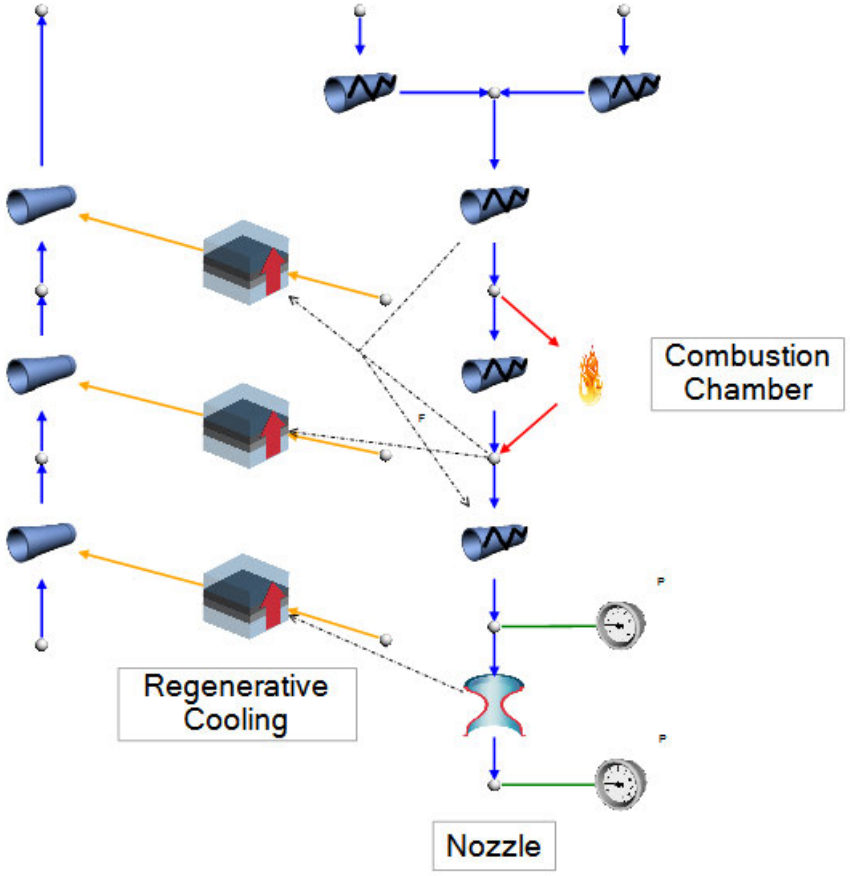

Figure 4-8: Flownex® subassembly of the regenerative cooling

Conduction

In the regenerative cooling case, conduction was modeled using the geometry and material data of the cooling channels found in Tables 4-14 to 4-17. The geometry of cooling channels is represented using the area upstream surface, the thickness in the element direction, the thickness in the cross direction, the number of nodes, and the area downstream surface. The area upstream surface represents the inner surface of the combustion chamber and nozzle. The thickness in the element direction is the wall thickness of the channels. The thickness in the cross direction represents the length of the combustion chamber, converging, and diverging sections. The number of nodes represents the two half control

volumes at the ends of the cooling channels volume with a third node centered in the control volume. The area downstream surface represents the inner surface of the cooling channel. The data used for the input parameters was derived from Wunderlin (2019), who designed a preliminary regenerative chamber and nozzle code using CuCrZr, a precipitation-hardened alloy with additions of chrome and zirconium. Table 4-14 contains the geometry inputs for the composite heat transfer responsible for removing heat from the combustion chamber.

Table 4-14: Combustion chamber composite heat transfer conduction geometry inputs

Conduction Geometry	Value	Unit
Chamber Area Upstream Surface	0.099	m^2
Thickness in Element Direction	0.0005	m
Thickness in Cross-direction	0.23	m
Number of Nodes	3	-
Area Downstream Surface	0.081	m^2

Table 4-15 contains the geometry inputs for the composite heat transfer for the converging section.

Table 4-15: Converging section composite heat transfer conduction geometry inputs

Conduction Geometry	Value	Unit
Chamber Area Upstream Surface	0.086	m^2
Thickness in Element Direction	0.0005	m
Thickness in Cross-direction	0.15	m
Number of Nodes	3	-
Area Downstream Surface	0.066	m^2

Table 4-16 contains the geometry inputs for the composite heat transfer for the diverging section of the rocket engine.

Table 4-16: Diverging section composite heat transfer conduction geometry inputs

Conduction Geometry	Value	Unit
Chamber Area Upstream Surface	0.15	m^2
Thickness in Element Direction	0.0005	m
Thickness in Cross-direction	0.21	m
Number of Nodes	3	-
Area Downstream Surface	0.13	m^2

Table 4-17 contains the material properties of CuCrZr used to manufacture the regeneratively SAFFIRE engines.

Table 4-17: Composite heat transfer conduction material inputs

Conduction Material Data	Value	Unit
Capacitance	383	kJ/m^3. K
Conductivity in Element Direction	356.43	W/m.K
Conductivity in Cross-direction	356.43	W/m.K

Convection

Convective heat transfer was modeled using upstream and downstream variables consisting of the internal ambient temperature of the combustion engine, the convective heat transfer coefficients of the gas-side and the fluid-side, the fin efficiency, the fouling factor, and the area of the cooling channels. For the engine's combustion chamber and converging sections, the NASA CEA flame combustion temperature was linked to the internal ambient temperature using a data transfer link to approximate the combustion chamber and converging section internal temperatures, as seen in Figure 4-8. The average temperature over the exit thrust nozzle was used for the internal ambient temperature of the diverging section of the nozzle. It was assigned to the composite heat transfer element using a data transfer link displayed in Figure 4-8.

The downstream convective heat transfer coefficient represented by the gas-side heat transfer coefficient was calculated using the Bartz Equation discussed in Chapter 2-6. This is used to estimate the convective heat fluxes in rocket engines but loses its accuracy upstream of the throat, where the assumption of fully developed flow is unjustified. In this analysis, the underprediction of the upstream conditions is disregarded. For the liquid-side of the regenerative cooling, referred to as the upstream convective heat transfer coefficient, the Sieder-Tate equation discussed in Chapter 2-6 was used to evaluate the convective heat transfer coefficient at the combustion chamber, converging section, and diverging section of the engine.

The wall temperature of the three sections of the cooling channels was initially assumed for the first coolant side heat transfer coefficient calculation. The Nusselt number was calculated to find a separate convective heat transfer coefficient, and a new wall temperature was found. The wall temperature in the Sider-Tate equation was updated, and a new convective heat transfer coefficient was found. This iterative process was repeated until the wall temperature for both equations was equal, resulting in a convective transfer coefficient for each section of the rocket engine.

The convective heat transfer input variables also included a fin efficiency and a fouling factor, which was assumed to be 95% efficient for each section of the rocket engine, and the fouling factor was

assumed to remain constant. Furthermore, the upstream area for the gas-side convection was assumed to be the same as the areas used for the conduction heat transfer. Table 4-18 contains input values for the convection heat transfer section of the composite heat transfer elements.

Table 4-18: Composite heat transfer inputs for convection

Convection Input Variables	Value	Unit
Combustion Chamber and Throat Internal Temperature	3,571.95	K
Nozzle Internal Temperature	2,182.09	K
Chamber Gas-Side Convective Heat Transfer Coefficient	2,378	W/m^2. K
Converging Gas-Side Convective Heat Transfer Coefficient	6,387	W/m^2. K
Diverging Gas-Side Convective Heat Transfer Coefficient	832	W/m^2. K
Chamber Liquid-Side Convective Heat Transfer Coefficient	6,221	W/m^2. K
Converging Liquid-Side Convective Heat Transfer Coefficient	7,688	W/m^2. K
Diverging Liquid-Side Convective Heat Transfer Coefficient	4,754	W/m^2. K
Fin Efficiency	95	%
Fouling Factor	0.00018	m^2.K/W

Radiation

The radiation heat transfer was modeled in the composite heat transfer element using the form factor, the emissivity of the inner and outer layer of the cooling channel, the internal ambient temperature, and the ambient area of the inner surface. The inner surface area was assumed to be the same for the conduction heat transfer. The internal ambient temperature was assigned to the composite heat transfer elements using the same data transfer links used for the convective heat transfer. Table 4-19 contains the input values to model the radiation heat transfer through the cooling channels.

Table 4-19: Radiation input values for the composite heat transfer element

Radiation Input Variables	Value	Unit
Form Factor	1	-
The Emissivity of Inner Surface	0.7	-
The Emissivity of Outer Surface	0.7	-
Internal Ambient Temperature	357.95	K

As seen in Figure 4-8, three pipe elements and three composite heat transfer elements were used to model the three sections of the regenerative cooling channels. To increase the accuracy of the results, each pipe element was discretized into several increments. The number of increments was increased in steps of 100 until the density, the output temperature of the fluid, and the thrust remained constant, and

an equilibrium was reached. For each pipe element, the number of increments was found to be 1000 for equilibrium to be reached. The pipe elements also required the length of the regenerative cooling channel, the hydraulic diameter of channels, and the surface roughness for each section of the rocket engine. The input values for the channels of the combustion chamber, converging section, and diverging section are given in Table 4-20.

Table 4-20: Regenerative pipe element input variables

Pipe Input Variables	Value	Unit
Combustion Chamber Channel Length	0.23	m
Combustion Chamber Channel Diameter	0.0035	m
Converging Section Channel Length	0.15	m
Diverging Section Channel Diameter	0.0021	m
Nozzle Channel Length	0.21	m
Nozzle Channel Diameter	0.0031	m
Surface Roughness	4.5	μm

4.4. Flownex® Second Stage Engine Models Inputs

The second stage SAFFIRE rocket engines were also modelled in Flownex® as the vacuum thrust was required to calculate the payload mass for each engine configuration. Copies of the first-stage engines were made to create the second-stage simulation models, with changes being made to selected input variables of the elements. These variables included the mass flows of the fuel and oxidizer, the operating speed of the electropumps, the nozzle exit diameter, and the momentum correction factor of the nozzle. Table 4-21 gives the input variables and corresponding values changed on the first-stage engines to represent the second-stage engines.

Table 4-21: Updated input variables for second-stage engines

Changed Input Variables	Value	Unit
Fuel Mass Flow Rate	2.56	kg/s
Oxidizer Mass Flow Rate	7.44	kg/s
Fuel Pump Speed at BEP	36,000	rpm
Oxidizer Pump Speed at BEP	17,078.7	rpm
Exit Thrust Nozzle Exit Diameter	600	mm
Exit Thrust Nozzle Momentum Correction Factor	0.92	-

The oxidizer and fuel pump head and volume flow rate at BEP for the electropump and the turbopump rocket engines changed because of the changes in the rotational speed of the pumps; pressure drops across the system, and the changes in the mass flow rates. The updated turbopump centrifugal pump

parameters, including the increased fuel head at BEP for the regeneratively cooled engine for the second stage engine, are displayed in Table 4-22.

Table 4-22: Second-stage turbopump pump parameters

Centrifugal Pump	Value	Unit
Fuel Pump Head at BEP	503.24	m
Fuel Volume Flow at BEP	0.0035	m^3/s
Regeneratively Cooled Fuel Pump Head at BEP	538.78	m
Oxidizer Pump Head at BEP	356.92	m
Oxidizer Volume Flow at BEP	0.0064	m^3/s

Table 4-23 contains the updated values for the centrifugal pumps of the electropump cycle, including a second fuel pump head at BEP for the regeneratively cooled rocket engine, which experiences a larger pressure loss caused by the cooling channels.

Table 4-23: Second-stage electropump pump parameters

Centrifugal Pump	Value	Unit
Fuel Pump Head at BEP	501.5	m
Fuel Volume Flow at BEP	0.0032	m^3/s
Regeneratively Cooled Fuel Pump Head at BEP	536.69	m
Oxidizer Pump Head at BEP	362.34	m
Oxidizer Volume Flow at BEP	0.0064	m^3/s

4.5. Surrogate Rocket Propellant Mixture

RP-1 fluid reference data was required for the simulations of the SAFFIRE rocket engine configurations. Thereafter, performance data from the Fastrac and Rutherford rocket engines were used for validation. Flownex® has an existing fuel library of liquids and gases, but it only has two kerosene fuels, namely JP-10, a high-density jet propellant, and JP-8, a fuel equivalent to Jet-A1 aviation fuel and RP-1. Both fluids were unusable for the simulations. The density of JP-10 was too high and is a fuel that is not readily available for use in South Africa. The JP-8 density and properties were unsuitable for the simulation as large amounts of fluid data were missing from the fuel library, and the fluid was not gaseous within Flownex®. Therefore, a new project-based fluid representing RP-1 was created and imported into the simulations. The most suitable approach was to create a fuel surrogate mixture due to the extensive number of fluid properties required. Fuel surrogate mixtures consist of eight or fewer compounds representing the thermophysical properties of complex fuels, allowing detailed combustion modeling of complex fuels that typically consist of hundreds of compounds. Using a chemical analysis and numerous thermophysical property tests, Huber et al., (2009) determined that the surrogate mixture

of the RP-1 can be represented using four components, α-Methyldecalin, n-Dodecane, 5-Methylnonane, and Heptylcyclohexane. Comparisons with experimental data of the fuel sample demonstrated that the surrogate mixture represented the density, sound speed, viscosity, and thermal conductivity within 0.4%, 2%, 2%, and 4% error at a 95% confidence level (Huber et al., 2009). Table 4-24 contains the composition of the RP-1 surrogate mixture in terms of mole fraction quantities.

Table 4-24: Composition of RP-1 surrogate mixture

Fluid Type	Mole Fraction
α-Methyldecalin	0.354
n-Dodecane	0.15
5-Methylnonane	0.183
Heptylcyclohexane	0.313

National Institute of Standards and Technology (NIST) Reference Fluid Thermodynamic and Transport Properties (Refprop) was used to create the surrogate mixture of RP-1 (Lemmon et al., 2018). NIST Refprop can provide thermophysical properties of pure fluids and mixtures for various fluid conditions, including liquid gas and supercritical phases. Flownex® can import fluids using NIST, allowing for the project fluid to be imported by stipulating the mole ratio of the four fluids, automatically generating all the fluid property curves.

4.6. Payload Mass Estimation

As a means of comparing the performance of each engine variation, the parameter of primary interest in this study was the payload mass of CLV. An open-source application called Launcher Calculator® was used to evaluate the payload mass capacity of CLV for each engine configuration (Nikishchenko, 2020). The software allows users to assess the impact of main rocket characteristics on the payload mass. The launcher calculator is split into four sections: rocket, spaceport, orbit losses, and output.

The payload approximation begins with inserting the performance parameters of the rocket's first-stage and second-stage engine, the size of the launch vehicle, and the mass ratios for the rocket section of the software. Initially, the type of feed cycle, the number of stages, and the propellant types are selected under the rocket section. The first stage, engine thrust at sea level, and the second stage, thrust at vacuum, are entered into the software. The maximum rocket diameter, the fairing mass, and the fairing mass jettison velocity are then inputted into the software. Finally, the percentage of unused propellant of the first and second-stage engines and the specific impulse of both rocket engines at sea level and vacuum are added.

The spaceport section of the software requires the launch point altitude above sea level, any additional velocity (Air Launch), and the latitude angle of the launch facilities. The type of orbit must also be

supplied along with the orbit apogee and the orbit inclination angle. The losses section implements an array of formulae to estimate the gravitational and aerodynamic losses and a required Delta-V for the mission. Under output, the first and second-stage propellant and dry masses are added, allowing for an approximate first-stage and second-stage mass ratio to be calculated and a final payload mass to be found.

The mass-estimating relationships discussed in Chapter 3 were used to evaluate each stage's propellant mass, subcomponent masses, and the vehicle's wet and dry mass. The rocket performance parameters were extracted from each Flownex® simulation of the SAFFIRE engine configuration, with the spaceport and orbit inputs remaining constant for each calculation. The orbit input parameters included a 200-1,000 km apogee range for a Sun Synchronous Orbit (SSO). CLV was assumed to be launched from the Denel Overberg Test Range (OTR) located near Arniston in the Western Cape province of South Africa, with a latitude of -34.6° and a launch point altitude of 20 m.

4.7. Mass Estimating Relationship Parameters

This section summarizes the comparative parameters used in the mass estimating relationships of Chapter 3 to evaluate the mass of the electropump and gas generator cycles and the structural elements of CLV. The parameters are split into 11 subcomponents.

The common constants are parameters appearing in multiple launch vehicle components. These include the gas constants and molar mass of the pressurant gas, the combustion chamber pressure of the rocket engines, the initial tank pressure, pressure losses, tank ullage ratios, mass flow rates, *O/F* ratios, and the burn times of the first and second stage engines. The common constants used to evaluate the subcomponents of both electropump, and gas generator cycle rocket stages are found in Tables 4-25 and 4-26.

Table 4-25: Mass estimating relationship's common constants

Name	Symbol	Value	Unit
Nitrogen Gas Constant	R_N	593.6	J/kmolK
Combustion Chamber Pressure	p_{cc}	3,500,000	Pa
Initial Tank Pressure	$p_{ot/ft}$	250,000	Pa
Initial Pressure to Chamber Pressure Ratio	K_{pr}	0.071	-
Initial Pressurant Tank Pressure	p_0	35,000,000	Pa
Injector Pressure Drop	P_{inj}	700,000	Pa
Injector Pressure Drop to CC Pressure Ratio	K_{pi}	0.2	-
Oxidizer Ullage Ratio	$K_{ul,o}$	1.05	-
Fuel Ullage Ratio	$K_{ul,f}$	1.04	-

Table 4-26: Mass estimating relationship's common constants continued

Name	Symbol	Value	Unit
1st Stage O/F Ratio	O/F	2.39	-
1st Stage Total Propellant Fraction	α_t	0.00099	-
1st Stage Oxidizer Mass Flow Rate	$\dot{m}_{o,1}$	7.05	kg/s
1st Stage Fuel Mass Flow Rate	$\dot{m}_{f,1}$	2.95	kg/s
1st Stage Burn Time	$t_{b,\,1}$	164	s
2nd Stage O/F Ratio	O/F	2.91	-
2nd Stage Total Propellant Fraction	α_t	0.00098	-
2nd Stage Oxidizer Mass Flow Rate	$\dot{m}_{o,2}$	7.44	kg/s
2nd Stage Fuel Mass Flow Rate	$\dot{m}_{f,2}$	2.56	kg/s
2nd Stage Burn Time	$t_{b,\,2}$	236	s

The propellant selected for the tank pressurant, and pneumatic controls was nitrogen. The volume and thickness of the first- and second-stage tanks were required to evaluate the mass of the nitrogen and the storage tanks. The preliminary design of the nitrogen tanks produced by Gyasi-Agyei, (2021) consisted of four spherical tanks for the first stage and the single spherical tank for the second stage. At the end of a mission, residual gases remain in the tanks, contributing to the rocket's final mass. According to (Sutton and Biblarz, 2001), the residual pressurant can be approximately 1 - 2%. The upper limit of 2% was selected for the first and second-stage residual gas mass evaluation. The constants used to evaluate the pressurant and the tanks are displayed in Table 4-27.

Table 4-27: Mass estimating relationship's pressurant constants

Name	Symbol	Value	Unit
Residual Pressurant Factor	K_{propg}	1.002	-
Nitrogen Specific Heat Ratio	γ_N	1.4	-
Pressurizing Gas Safety Factor	K_{tg}	1.2	-
Propellant Tank Density	ρ_{pt}	4,430	kg/m^3
1st Stage Pressurant Tank Volume	$V_{pt,\,1}$	0.028	m^3
1st Stage Pressurant Tank Thickness	$e_{pt,\,1}$	0.0048	m
2nd Stage Pressurant Tank Volume	$V_{pt,\,2}$	0.017	m^3
2nd Stage Pressurant Tank Thickness	$e_{pt,\,2}$	0.0041	m

316 stainless steel was selected for the propellant tanks due to the high tensile strength at cryogenic temperatures and ease of manufacturing. The properties of the 316 stainless steels are found in Table 4-28. The fuel and oxidizer tanks were also calculated to be 0.5 mm thick.

Table 4-28: Mass estimating relationship's propellant tank constants

Name	Symbol	Value	Unit
316 Stainless Steel Yield Stress	σ_{ot}	276,000,000	Pa
316 Stainless Steel Density	ρ_{ot}	7,880	kg/m^3
Propellant Tank Thickness	e_t	0.0005	m

RP-1 was selected as the fuel for the SAFFIRE rocket engine. To evaluate the mass of the fuel used during the duration of the flight, the fuel density was required and extracted from NIST Refrop at 101.325 kPa and 298 K. The fuel tank length, volume, and residual propellant percentages are adapted from the preliminary designs of CLV propellant tanks (Gyasi-Agyei, 2021). The fuel constants used to evaluate the mass of the fuel and fuel tank are listed in Tables 4-29.

Table 4-29: Mass estimating relationship's fuel constants

Name	Symbol	Value	Unit
Fuel Density	ρ_f	800	m^3/kg
1st Stage Fuel Tank Length	$L_{ft,\,1}$	3.98	m
1st Stage Fuel Tank Volume	$V_{ft,\,1}$	5.71	m^3
1st Stage Fuel Volume	$V_{f,\,1}$	5.47	m^3
1st Stage Fuel Propellant Fraction	$\alpha_{f,\,1}$	0.00037	-
1st Stage Residual Fuel Factor	$K_{propf,\,1}$	1.0027	-
2nd Stage Fuel Tank Length	$L_{ft,\,2}$	0.33	M
2nd Stage Fuel Tank Volume	$V_{ft,\,2}$	0.79	m^3
2nd Stage Fuel Volume	$V_{f,\,2}$	0.75	m^3
2nd Stage Fuel Propellant Fraction	$\alpha_{f,\,2}$	0.00032	-
2nd Stage Residual Fuel Factor	$K_{propf,\,2}$	1.0023	-

The same procedure was used to evaluate the oxidizer tanks with the tank parameters and the residual propellant factor. Tables 4-30 and 4-31 contain the oxidizer constants used for the mass estimating relationships.

Table 4-30: Mass estimating relationship's oxidizer constants

Name	Symbol	Value	Unit
Oxidizer Density	$\rho_{o,\,1}$	1,126.1	m^3/kg
1st Stage Oxidizer Propellant Fraction	$\alpha_{o,\,1}$	0.00063	-
1st Stage Oxidizer Tank Volume	$V_{ot,\,1}$	9.81	m^3
1st Stage Oxidizer Volume	$V_{o,\,1}$	9.31	m^3

Table 4-31: Mass estimating relationship's oxidizer constants continued

Name	Symbol	Value	Unit
1st Stage Residual Oxidizer Factor	$K_{propo,\ 1}$	1.0064	-
1st Stage Oxidizer Tank Length	$L_{ot,\ 1}$	7.17	m
2nd Stage Oxidizer Propellant Fraction	$\alpha_{o,\ 2}$	0.00066	-
2nd Stage Oxidizer Tank Volume	$V_{ot,\ 2}$	1.65	m^3
2nd Stage Oxidizer Volume	$V_{o,\ 2}$	1.57	m^3
2nd Stage Residual Oxidizer Factor	$K_{propo,\ 2}$	1.0066	-
2nd Stage Oxidizer Tank Length	$L_{ot,\ 2}$	1.03	m

The SAFFIRE engine design is similar in concept to the Rutherford liquid rocket engine, which utilizes DC brushless electric motors to drive the pumps. The motor parameters used for the SAFFIRE engine were, therefore, set to those of the Rutherford rocket engine (Liu et al., 2021). Table 4-32 contains the pump constants used for the oxidizer and fuel pump of the electropump cycles.

Table 4-32: Mass estimating relationship's pump constants

Name	Symbol	Value	Unit
Pump Efficiency	η_{fpu}	0.5	-
Pump Power Density	δ_{fpu}	10	kW/kg

The gas generator exhaust gases were calculated using CEA, an input flow rate of 0.3 kg/s, and a combustion pressure of 25 bar. The stay time and the gas generator chamber safety factor were used from historical reports (Rachov and Tacca, 2010). The gas generator is proposed to be made from Inconel 718. The gas generator exhaust gas and material properties are provided in Tables 4-33, and 4-34.

Table 4-33: Mass estimating relationship's gas generator constants

Name	Symbol	Value	Unit
GG Molar Mass	M_{gg}	16	g/mol
GG Gas Constant	R_{gg}	519.65	J/kmolK
Exhaust Gas Specific Heat Ratio	γ_{gg}	1.24	-
Density of Burnt Gas	ρ_{gg}	3.46	kg/m^3
Stay Time	t_s	0.01	s
GG Material Density	$\rho_{gg,m}$	8,220	kg/m^3
GG Chamber Wall Thickness Factor	K_{gg}	1.5	-

Table 4-34: Mass estimating relationship's gas generator constants continued

Name	Symbol	Value	Unit
GG Chamber Pressure	p_{gg}	2,500,000	Pa
GG Chamber Yield Stress	$\sigma_{gg,m}$	550,000,000	Pa

Figure 4-9 shows the turbopump power densities of existing LOX/RP-1 rocket engines against the vacuum thrust each engine produced. Most gas generator turbopumps within the dashed block consist of a power density range from 11 kW/kg to 16 kW/kg for a 20 kN to 1,050 kN thrust range (Kwak et al., 2018). The mean average with a 1.5 kW/kg standard deviation was 13.5 kW/kg. Thus, the turbopump power density of 13.5 kW/kg was used to analyze the gas generator cycle.

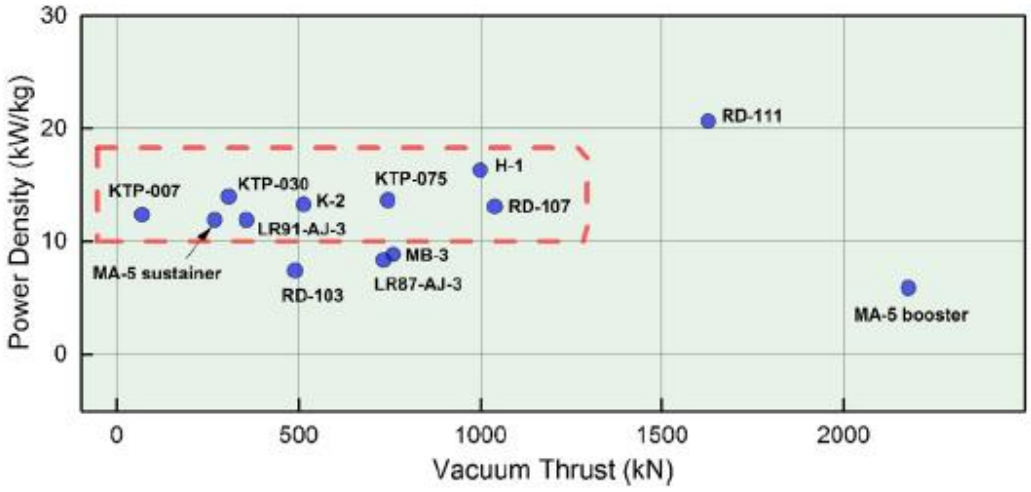

Figure 4-9: Turbopump power densities of LOX/RP-1 rocket engines (Kwak et al., 2018)

The turbine efficiency was an average of the efficiencies from historical reports of previously built and tested turbines used in gas generator rocket engine cycles (Macaluso and Douglass, 1974). It is proposed that the turbine be manufactured from Inconel 718 and has a maximum entry temperature of 900 K to prevent any damage. Tables 4-35 and 4-36 list the turbine input conditions used to assess the turbine mass of the gas generator cycle.

Table 4-35: Mass estimating relationship's turbine constants

Name	Symbol	Value	Unit
Turbine Efficiency	η_{tu}	0.52	-
Turbine inlet temperature	T_{itu}	900	K
Turbine Discharge Pressure	p_{dtu}	250,000	Pa
Turbine Pressure Ratio	PR_{tu}	10	-

Table 4-36: Mass estimating relationship's turbine constants continued

Name	Symbol	Value	Unit
Turbine Inlet Pressure	p_{itu}	2,500,000	Pa
Turbine Power Density	δ_{tu}	13.5	kW/kg

The inverter efficiency and power density are the same performance characteristics of the inverter and battery pack mass used in the Rutherford electropump rocket engine. They are displayed in Table 4-37 (Liu et al., 2021).

Table 4-37: Mass estimating relationship's inverter constants

Name	Symbol	Value	Unit
Inverter Efficiency	η_{inv}	0.85	-
Inverter Power Density	δ_{em}	60	kW/kg

Table 4-38 contains the motor efficiency and density based on the peak performances of the brushless DC motor used in the Rutherford rocket engine (Liu et al., 2021).

Table 4-38: Mass estimating relationship's electric motor constants

Name	Symbol	Value	Unit
Electric Motor Efficiency	η_{em}	0.9	-
Motor Power Density	δ_{em}	3.8	kW/kg

The battery pack mass is evaluated using the power density and energy density of the lithium-polymer battery made up of Amicell cells, with the density that produces the largest mass being the limiting factor. The lithium polymer battery pack has a power density of 6.95 kW/kg, an energy density of 0.198 kWh/kg, and an energy efficiency of 90%. The sizing factor of 1.2 ensures that the battery pack is large enough to last the entire burn time, as energy is lost due to heat and the lower limit to which the battery can be drained (Kwak et al., 2018). Table 4-39 contains the battery constraints of the SAFFIRE rocket engine.

Table 4-39: Mass estimating relationship's battery constants

Name	Symbol	Value	Unit
Sizing Safety Factor	K_b	1.2	-
Battery Power Density	δ_{bapo}	6.95	kW/kg
Battery Energy Density	δ_{baen}	0.198	kWh/kg
Energy Efficiency	η_E	0.9	-

5. Results and Discussion

5.1. Software Validation

For the purpose of validation, models of Rocket Lab's Rutherford electropump and NASA's Fastrac gas generator rocket engines were created to verify the accuracy of the results acquired from the SAFFIRE electropump and gas generator Flownex® simulations. Both rocket engines utilize RP-1 and LOX as the propellants, the same as the SAFFIRE rocket engines. The mechanical arrangement of the Rutherford rocket engine and the Fastrac engines are the same as the layouts proposed for the SAFFIRE engines, with a separate electric motor for each pump for the electropump cycle and a single-shaft dual impeller turbopump for the gas generator cycle.

5.1.1. Electropump Verification

The Rutherford engine is the first flight-ready engine that utilizes the electric-pump-fed engine cycle and powers Electron, a two-stage launch vehicle with a payload capacity of 200 kg. Electron uses a cluster of nine Rutherford engines for the booster stage and a single vacuum engine for the second stage, which is the same layout proposed for CLV. Although limited information on the Rutherford engine is available, data such as the thrust, pump input, and output parameters, was sufficient for the validation. The parameters used by Liu et al., (2021) are from the first version of the Rutherford engine and were used to generate a Flownex® model Liu et al., (2021) as seen in Figure 5-1.

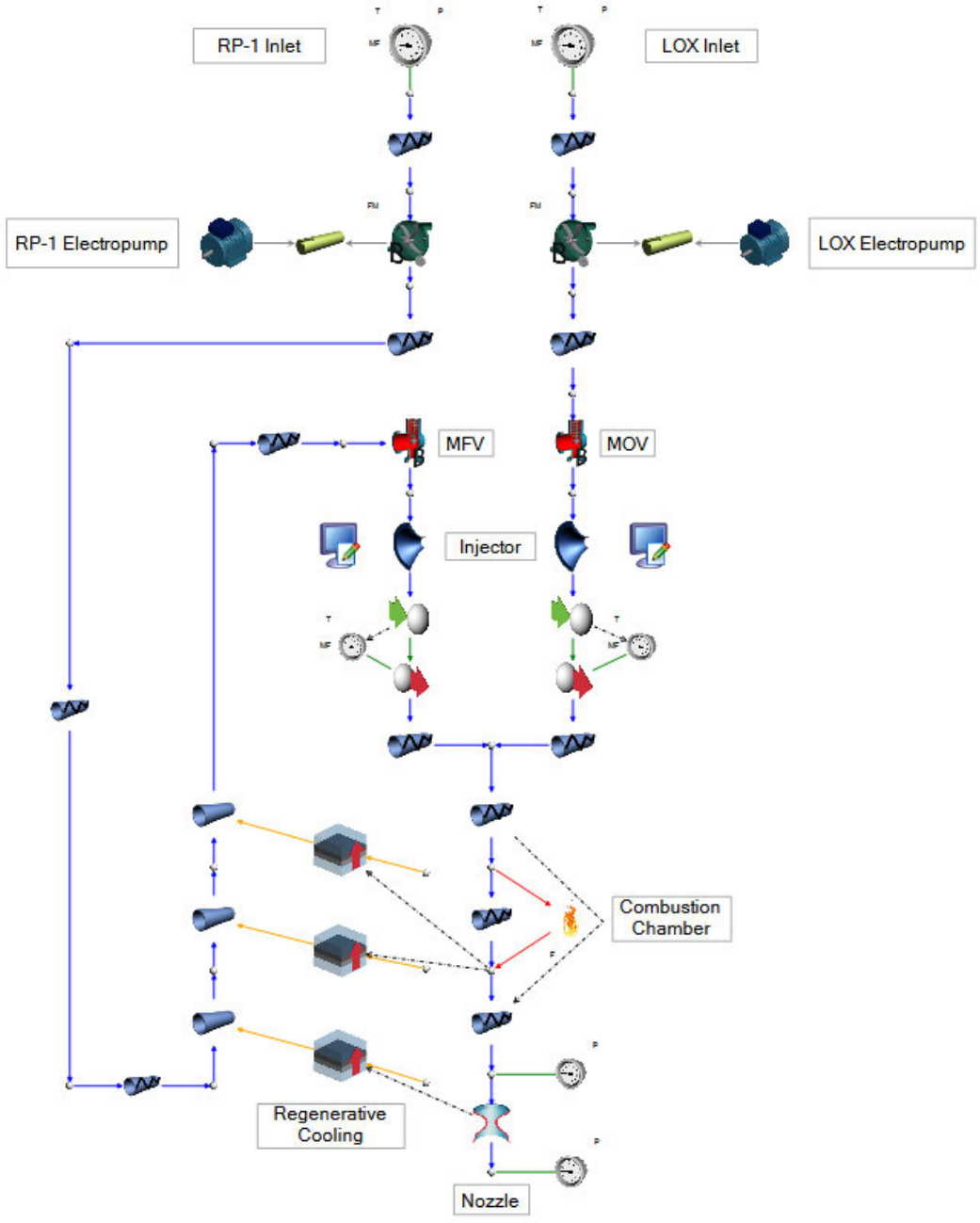

Figure 5-1: Rutherford electropump Flownex® model

Table 5-1 compares the performance data of the Rutherford engine published by Liu et al., (2021) and the data extracted from the Flownex® simulations with a percentage error for each parameter.

Table 5-1: Rutherford electropump engine verification parameters

Parameter	Paper Value	Flownex® Value	Percentage Error
Sea Level Thrust	22 kN	21.89 kN	- 0.50%
Sea Level Isp	286.78 s	285.48 s	- 0.45%
Combustion Chamber Pressure	30 bar	30.16 bar	+ 0.53%
Oxidizer Pump Exit Pressure	40.6 bar	40.58 bar	- 0.05%
Oxidizer Pump Efficiency	50%	49.46%	- 1.08%
Oxidizer Pump Power Consumed	36.1 kW	35.84 kW	- 0.72%
Fuel Pump Exit Pressure	52.5 bar	52.19 bar	- 0.59%
Fuel Pump Efficiency	45%	45.82%	+ 1.82%
Fuel Pump Power Consumed	29.1 kW	28.98 kW	- 0.41%

The validation exercise on the Rutherford engine produced good results for each major subsection of the rocket engine. The fuel pump efficiency has the highest percentage error of 1.82%. The second highest percentage difference was the oxidizer pump efficiency, with an error of 1.08%. These could be further minimized if the Rutherford pump curves were available for use in the simulation with the current pump curves an estimation created by Flownex® using the operating parameters consisting of the mass flowrate, the volumetric flow rate, and pressure head at the best efficiency point and the operating speed of the electric motors. Since the SAFFIRE engine's propellant pumps are also still in the design phase, the accuracy of the Rutherford pump parameters suggests that adequate electropump outputs can be estimated without pump curves. The percentage error of the exit pressure and the power consumed by the oxidizer and fuel pump may further decrease using an existing pump curve. However, it is within an acceptable error of 5% for the current analysis, which follows the same validation procedure as (Liu et al., 2021). The performance of the Rutherford combustion chamber and nozzle model in Flownex® was also reasonable, with a maximum error of 0.53% for the combustion chamber pressure. With all the performance parameters of the Flownex® model in close comparison to the values given by Liu et al., (2021), it can be argued that Flownex® is capable of accurately modeling an electropump rocket and that the electropump SAFFIRE models are likely to produce adequate results for the payload mass estimation of CLV.

5.1.2. Gas Generator Verification

The Fastrac rocket engine was NASA’s low-cost rocket engine that was proposed for a reusable launch vehicle and was extensively tested in a ground-based campaign. There are several Fastrac rocket engine documents on the gas generator, the combustion chamber, and the architecture of the rocket engine, allowing for the creation of the gas Fastrac Flownex® model. Insufficient data on the turbopump designs made the validations challenging, but the mass flow rates, the pressure head across the pump, and the pump's efficiency were available, which was enough to enable an approximation of power

consumption. NASA tested two nozzles for the Fastrac engine, the Bantam with a 15:1 expansion ratio and the X-34 with a 30:1 expansion ratio. For the verification of the Flownex® model, the Bantam expansion ratio was used, and a Flownex® model was created, as shown in Figure 5-2.

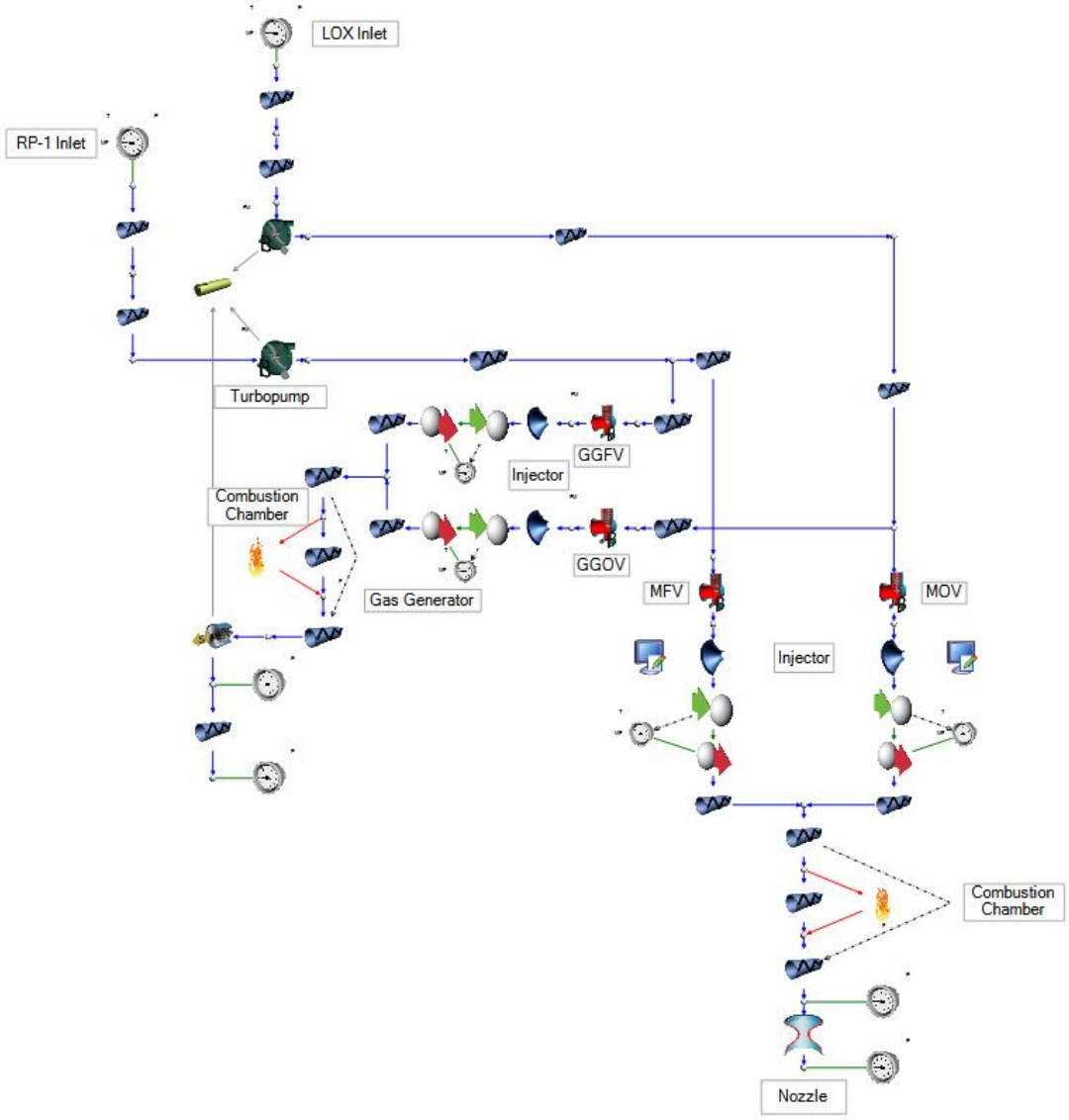

Figure 5-2: Fastrac gas generator Flownex® model

Table 5-2 gives the pump and performance parameters for the Bantam Fastrac rocket engines extracted from (Garcia and Nasa, 1999 and Kauffmann et al., 2001) and the comparative values from the Flownex® simulations with a percentage error for each parameter.

Table 5-2: Fastrac gas generator engine verification parameters

Parameter	Paper Value	Flownex® Value	Percentage Error
Sea Level Thrust	266.7 kN	269.54 kN	+ 1.06%
Vacuum Thrust	284.41 kN	286.21 kN	+ 0.63%
Sea Level Isp	306.15 s	305.97 s	- 0.06%
Vacuum Isp	326.48 s	328.55	+ 0.68%
Combustion Chamber Pressure	43.64 bar	43.78 bar	+ 0.32%
Oxidizer Pump Exit Pressure	61.71 bar	60.59 bar	- 1.81%
Oxidizer Pump Efficiency	83%	81.28%	- 2.07%
Oxidizer Pump Power Consumed	432.6 kW	431.88 kW	- 0.17%
Fuel Pump Exit Pressure	66.33 bar	67.64 bar	+ 1.97%
Fuel Pump Efficiency	85.8%	82.54%	- 3.80%
Fuel Pump Power Consumed	275.0 kW	267.9 kW	- 2.58%
GG Chamber Pressure	39.64 bar	39.64 bar	0%
GG Chamber Temperature	888.89 K	868.26 K	- 2.32%

Table 5-2 shows that the Flownex® model of the Fastrac rocket engine produced reasonably good results, all within a 5% error. The maximum error was the fuel pump efficiency at 3.8%. The Fastrac engine propellant pumps pump curves were based on the best efficiency point and operating speed and were estimated within Flownex®. If the pump curve of the Fastrac engine was imported into Flownex® for the propellant pumps, it is likely that the efficiency and the additional parameters, such as the exit pressure and the power consumed by the pumps, would decrease. When comparing the gas generator parameters, the combustion chamber pressure was modeled identically to the design value with a 0% error, and the chamber temperature was close to the author's value with a 2.32% error. The combustion chamber pressure was also close to the author's findings with a 0.42% error and resulted in a thrust value that is considered acceptable. The maximum error for the performance parameters of the rocket engine was 1.06% for the sea level thrust with vacuum thrust and the I_{sp} of both the altitude readings below 1%, which is close to the design and test data of the Fastrac engine. With a satisfactory level of validation achieved by comparing performance data from Garcia and Nasa, (1999) and Kauffmann et al., (2001) with the Flownex® model, it can be concluded that the gas generator models of the SAFFIRE engine are likely to provide acceptable values for the payload comparison between the various SAFFIRE engine configurations.

5.2. Feed Cycle Performance Comparison

A rocket design must minimize the initial mass of each stage to maximize the payload capabilities of the launch vehicle. Each electropump and gas generator cycle feed system was therefore analyzed to identify which cycle offered the lowest mass penalty.

The components considered for the feed system analysis were the propellants consumed by the combustion chamber (CC), the gas generator tap-off propellants, the battery pack, the tanks, the feed system, and the pressurant. The tank mass consists of the two propellant tanks and the pressurant tank. The feed system consists of the turbopump and gas generator for the gas generator cycle, the inverter, electric motors, and the two propellant pumps for the electropump cycle. Table 5-3 contains the first stage masses of the electropump (EP) and gas generator (GG) feed cycle components. Table 5-3 also contains a mass ratio of EP/GG to compare the mass penalty difference for each component of the feed cycle and an overall mass ratio (MR) to identify which cycle has the lowest weight penalty.

Table 5-3: CLV first stage feed cycle component mass comparison

	GG Cycle	**EP Cycle**	**EP/GG**
CC Propellants	14,862.06 kg	14,862.06 kg	1
GG Propellants	191.94 kg	-	-
Battery Pack	-	212.76 kg	1.11
Tanks	250.41 kg	248.01 kg	0.99
Feed System	121.9 kg	202.41 kg	1.66
Pressurant	32.2 kg	31.79 kg	0.99
Total	15,458.51 kg	15,557.03 kg	1.01
MR	0.026	0.045	1.73

Figure 5-3 displays the feed cycle masses from Table 5-3 in a percentage form to illustrate how each component contributes to the final mass of the launch vehicle. The outer ring represents the electropump cycle, and the inner ring is the gas generator cycle. The combustion chamber propellants for the electropump and gas generator cycles were calculated to be the same for each engine. During use, the exhaust gases that exit the gas generator produce thrust, contributing an additional 1% of the total thrust from the main combustion chamber. The analysis between the SAFFIRE engines does not consider constant thrust levels for each engine as the study requires identifying the engine that produces the most thrust using available components and the same total mass flow rate to the combustion chamber. Therefore, the combustion chamber propellants are kept constant for the mass analysis of both cycles.

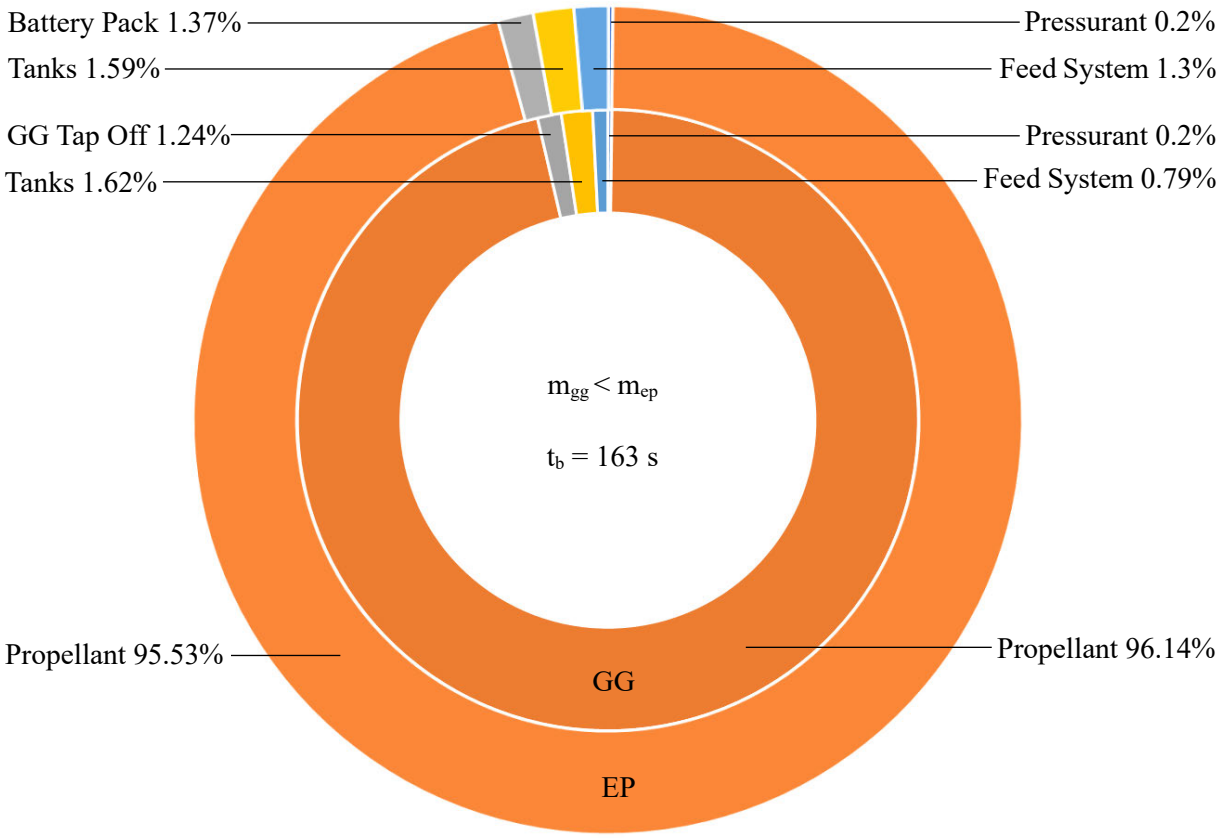

Figure 5-3: The first stage of initial mass budgets for each engine cycle

The gas generator tap-off propellant mass is compared to the battery pack mass, as the battery pack is also the source of energy used to drive the pumps. The battery pack used for the analysis has a characteristic burn time of 103 seconds, which can be found using equation 5-1.

$$t_c = \frac{\delta_{\text{bapo}}}{\delta_{\text{baen}}} \tag{5-1}$$

The burn time of 163 s of the booster stage is greater than the characteristic burn time of the battery pack, implying that the battery pack is energy-constrained. This leads to less available energy from the battery cells, resulting in an increased mass of the battery pack. Table 5-3 shows that the energy-constrained battery pack is heavier than the propellant consumed by the gas generator, with the GG propellant mass 11% less than the battery pack mass.

Unlike the GG propellants, which are burnt during operation, the battery pack mass is dead mass as it remains onboard the vehicle after it is depleted, contributing to its final dry mass and reducing the overall payload capability. The battery pack mass can be minimized if future lithium polymer batteries achieve a higher energy density. For the battery pack mass to weigh the same as the mass of the GG propellants, the energy density must increase from 198 Wh/kg to 220 Wh/kg. For the battery pack to achieve the optimum performance equivalent to the gas generator cycle, the battery pack's characteristic

time must match the burn time of the booster stage. This is achievable if the energy density increases to 314.68 Wh/kg for the same power density of 6.95 kW/kg.

The electropump cycle tank mass is 1% lower than the gas generator cycle because the gas generator cycle tanks require a large volume to account for the additional propellant consumed by the gas generator. The feed system mass of the electropump cycle is greater than the gas generator cycle by 66%. The electric motors are major contributors due to their poor power density, with the pump and inverter mass also contributing to the higher mass penalty. The overall mass ratio is found by calculating the ratio of the dry mass components (the tanks, battery pack, and feed system) to the combustion chamber propellants. The mass ratio shows that the electropump cycle is worse than the gas generator cycle, with a higher payload factor of 1.73. The higher mass ratio of the electropump cycle is due to the larger dry mass after the burn time with the battery pack, pumps, and inverter remaining behind, unlike the gas generator cycle, where the turbopump and gas generator is the only dead mass components. Nevertheless, with significant advancements in battery and motor technology expected, the overall mass of the electropump cycle will continue to decrease and potentially become comparable with the gas generator cycle.

The same analysis was conducted for the second stage feed cycles of CLV with the mass results for each subcomponent of the two cycles and the mass ratio displayed in Table 5-4. It is crucial to minimize the initial mass of the launch vehicle's second stage since it is the payload of the lower stage and has a significant influence on the vehicle's overall payload capability.

Table 5-4: Second stage feed cycle component mass comparison

	GG Cycle	**Elec Cycle**	**Elec/GG**
CC Propellants	2,361.06 kg	2,361.06 kg	1
GG propellants	30.2 kg	-	-
Battery Pack	-	40.25 kg	1.33
Tanks	51.61 kg	51.18 kg	0.99
Feed System	6.3 kg	26.6 kg	4.22
Feed Pressurant	5.1 kg	5.04 kg	0.98
Total	2,454.27 kg	2,484.13 kg	1.01
MR	0.026	0.050	1.92

Figure 5-4 is a visual indication of the masses listed in Table 5-4 and shows the influence each component of the feed cycle has on the overall mass.

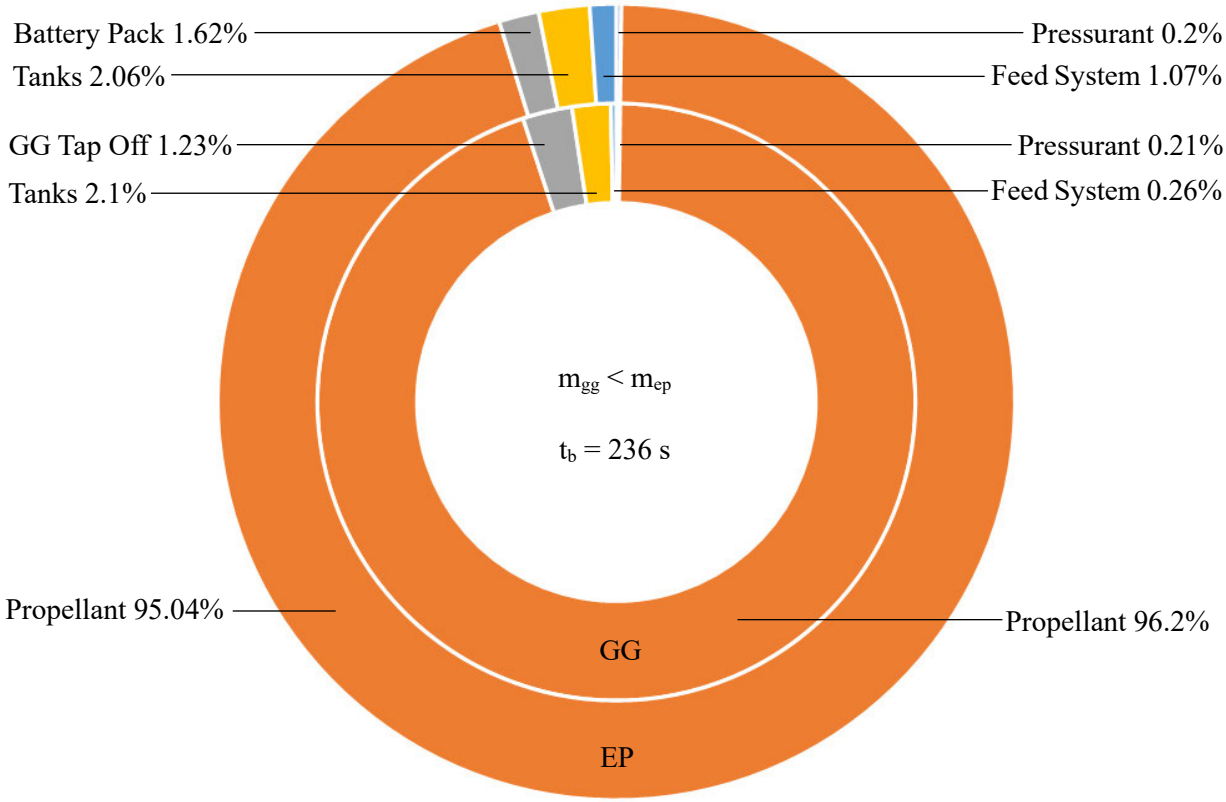

Figure 5-4: The second stage initial stage mass budgets

The electropump masses are displayed in the outer ring, and the gas generator mass is in the inner cycle. The propellants consumed by the combustion chamber remained constant as the mass flow rates and burn time were kept constant and did not vary to ensure a constant thrust level. The second-stage engines use the same lithium polymer cells as the first-stage engines. With a longer burn time of 236 seconds, the battery pack mass remains energy-constrained as the burn time exceeds the battery characteristic burn time and has a limited amount of energy to supply to the electric motors, resulting in a heavier battery pack weighing 1.33 times more than the GG propellants. For the battery pack mass to achieve equal mass as the propellants consumed by the gas generator, the energy density of the battery pack must increase from 198 Wh/kg to 264 Wh/kg. To closely match the payload capabilities of the gas generator cycle and minimize the battery pack mass penalty by having a characteristic burn time the same as the second stage burn time, the ideal energy density for the second stage is 510 Wh/kg for the same power density of 6.95 kW/kg.

The tank mass of the two feed cycles is similar, with the electropump cycle tanks outweighing the gas generator cycle by 430 grams due to the increased volume of the gas generator propellant tanks. The poor power density of the electric motors of the electropump cycle is emphasized in the second stage mass, with the feed system weighing 4.22 times more than the gas generator cycle feed system. The propellant pumps and inverter mass also contribute to the higher dry mass of the feed system. The total

masses of the second-stage feed cycles are closely matched as the electropump cycle weighs 1% more than the gas generator cycle, with the larger feed system a major contributor to the increased mass. While the total masses are similar, the mass ratio shows that the electropump feed cycle is nearly two times greater in mass than the gas generator feed cycle due to the large dry mass penalty of the battery pack and electric motors, which remain on board throughout the mission even when depleted. This dead mass penalty negatively affects the payload capabilities of CLV.

5.3. Mass Sensitivity Analysis

The proceeding section comprises a sensitivity analysis of the electropump and gas generator cycles for the first and second-stage SAFFIRE rocket engines. Sensitivity analysis helps identify how each input variable for a given output parameter influences the results, in this case, the feed cycle mass. A sensitivity analysis can be either of a multiple-factor or a single-factor type. The single-factor approach only examines one input variable at a time and can reflect the sensitivity of the mass of the feed system to each input variable. It can be simplified by assuming no interaction between the feed system mass model input variables. Thus, a single-factor sensitivity analysis was adopted here.

It was assumed that there are n influencing input variables b (b_1, b_2, $b_3 \ldots b_n$) of the parameter M that influence the feed system mass. Therefore, equation 5-2 can be given as:

$$M = f(b_1, b_2, b_3 \ldots b_n) \tag{5-2}$$

For each of the influencing input variables, there is a reference value $\hat{b} = \{\hat{b}_1, \hat{b}_2, \hat{b}_3 \ldots \hat{b}_n\}$ and the contributing component of the feed system will have a reference mass $\hat{M}$. Assuming that the change in mass of the contributing component M of the feed system is caused by the input variables b (b_1, b_2, $b_3 \ldots b_n$), the sensitivity of each variable can be defined as the ratio of the relative deviation of the mass of M to the relative deviation of the influencing variables as seen in equation 5-3.

$$S(b_n) = \frac{\frac{|\Delta M|}{\hat{M}}}{\frac{|\Delta b_n|}{\hat{b}_n}} \tag{5-3}$$

Four impact level scales, -10%, -5%, 5%, and 10%, were used for the sensitivity analysis to identify how each contributing component's input variables affected the feed system's overall mass for each engine cycle.

5.3.1. Electropump Cycle

The electropump cycle has eight input variables that can influence the mass of the feed system, including the fuel and oxidizer pump efficiencies and power densities, the inverter efficiency and power density, the electric motor efficiency and energy density, and the energy density of the battery pack. Another factor that can be considered but was neglected as it had no influence was the battery pack's

power density. Since the first-stage engines' burn time exceeds the battery's characteristic burn time, the battery pack is energy-constrained and independent of the power density. Table 5-5 and Figure 5-5 contain the impact levels the electropump input variables had on the mass of the supply system of the first stage of CLV.

Table 5-5: CLV first-stage electropump mass sensitivity of the feed system

Parameter	Impact Level				Average Sensitivity	Sensitivity Rating
	-10%	-5%	5%	10%		
δ_{fpu}	0.055	0.052	0.046	0.046	0.050	7
δ_{opu}	0.088	0.085	0.075	0.070	0.080	6
η_{inv}	0.57	0.54	0.49	0.47	0.52	3
δ_{inv}	0.028	0.026	0.020	0.021	0.024	8
$\delta_{ba,en}$	0.57	0.54	0.49	0.47	0.52	3
η_{em}	0.60	0.57	0.51	0.49	0.54	2
δ_{em}	0.37	0.35	0.32	0.31	0.34	5
η_{fpu}	0.43	0.41	0.36	0.35	0.39	4
η_{opu}	0.68	0.65	0.58	0.56	0.62	1

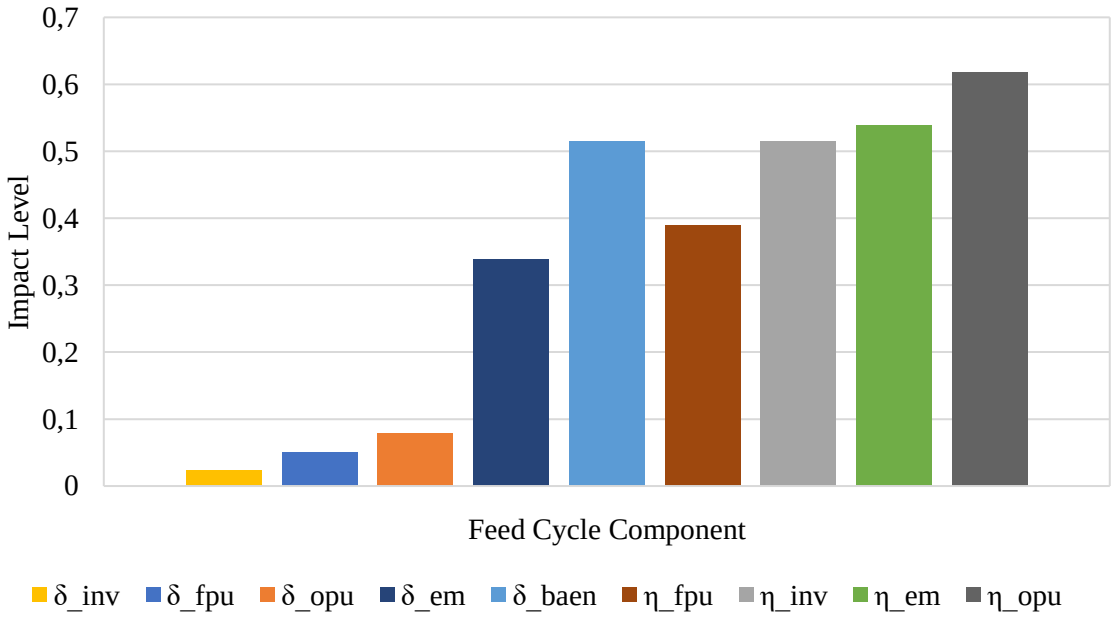

Figure 5-5: First-stage electropump mass sensitivity of each factor

Table 5-6 and Figure 5-6 give the impact levels the electropump input variables had on the mass of the supply system of the second stage of CLV.

Table 5-6: CLV second-stage electropump mass sensitivity of the feed system

Parameter	Impact Level				Average Sensitivity	Sensitivity Rating
	-10%	-5%	5%	10%		
δ_{fpu}	0.036	0.035	0.032	0.031	0.033	7
δ_{opu}	0.079	0.075	0.067	0.064	0.071	6
η_{inv}	0.67	0.63	0.57	0.55	0.61	3
δ_{inv}	0.019	0.019	0.019	0.019	0.019	8
δ_{baen}	0.67	0.63	0.57	0.55	0.61	3
η_{em}	0.69	0.65	0.59	0.57	0.63	2
δ_{em}	0.31	0.29	0.26	0.25	0.28	5
η_{fpu}	0.36	0.34	0.31	0.29	0.32	4
η_{opu}	0.75	0.72	0.64	0.61	0.68	1

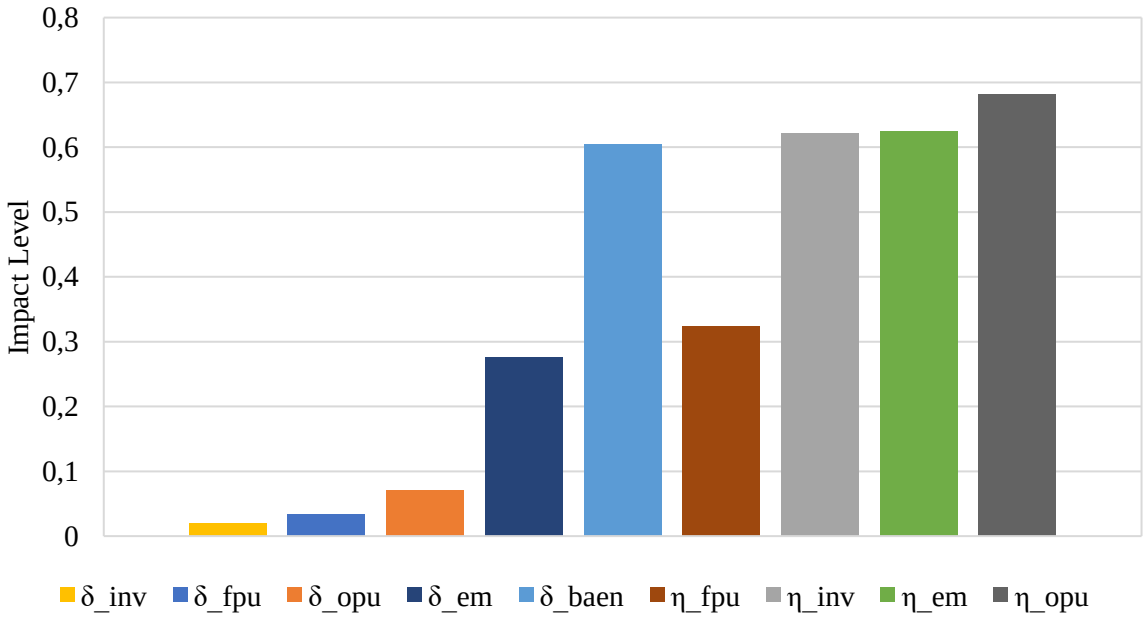

Figure 5-6: Second-stage electropump mass sensitivity of each factor

The results show that CLV's electropump stages have the same sensitivity ranking. From Table 5-5 and Figure 5-5 of the first stage and Table 5-6 and Figure 5-6 of the second stage, the oxidizer and fuel pump efficiency, the electric motor efficiency and power density, the inverter efficiency and the energy density of the battery pack have the largest impact on the mass of the feed system. The oxidizer and

fuel pump efficiencies affect the masses of the pumps, the electric motor, the inverter, and the battery pack, which are the largest mass-contributing components and are why efficiencies have the highest and fourth-highest sensitivity ranking, respectively. The oxidizer pump efficiency has the highest sensitivity ranking due to the higher density of liquid oxygen and a larger propellant mass fraction, resulting in large power requirement changes when the efficiency varies, affecting all four feed cycle components. Since the electric motors and battery packs contribute the most to the feed cycle mass, the oxidizer pump efficiency plays a crucial role in reducing the mass of components by minimizing the amount of power required with increased efficiency. The electric motor's energy density only affects the mass of the electric motor. Electric motors are the second largest mass contributors to the electropump cycle's feed system. Each component is considered to be a dead mass that directly affects the payload capacity of the launch vehicle and has a large influence over the mass of the electropump feed cycle. The inverter and motor efficiencies influence the mass of the inverter and the battery pack. Since the mass of the inverter contributes a small percentage of the total feed cycle mass, the effect it has on the battery pack mass, the largest mass of the feed cycle, gives the variables a large sensitivity ranking and plays an important role in increasing the payload mass of the launch vehicle by maximizing the efficiencies of the components to reduce the battery pack mass.

The power densities of the inverter, fuel pump, and oxidizer pump only affect the mass of the inverter and pumps, which have a small mass contribution to the total feed system mass and have the lowest sensitivity values. The energy density of the battery pack and the inverter efficiency have the same impact on the total mass of the feed system. When the inverter's efficiency increases, the required battery energy decreases by the same amount, which is equivalent to the energy density of the battery pack increasing. Therefore, the sensitivity of the two components is the same.

The sensitivity analysis shows that numerous input variables influence the mass of the battery pack, which is the largest contributor to the dry mass of the electropump cycle. Another key factor that plays a role in the mass of the battery pack is the working time or duty cycle. When the rocket stage burn time is shorter than the characteristic burn time of the battery pack, the power density determines the mass of the battery pack. For most rocket engines, including the SAFFIRE engines, the burn time exceeds the characteristic burn time, and an energy-constrained battery pack is used. Although lithium-ion batteries often have higher energy densities than lithium polymer batteries, it is difficult to find one that matches the large current outputs in a short operating time due to the slow discharge and recharging rate. Electropump rocket engines require rapid starting procedures, shutdowns, and quick mass flow rate adjustments, making the lithium-ion battery packs unsuitable for use for the short working time of the rocket engines. At the present stage, there are large advancements in battery technology with new composite batteries that combine the high energy batteries with high power density supercapacitor batteries being made that meet the performance requirements of the electropump cycle and will reduce the mass of the electropump cycle, increasing the cycles payload capacity. The electropump cycle mass

remains high compared to the turbopump cycle, which impedes its payload capacity. However, with steady advancements in battery technology, the mass of the battery pack will continue to decrease and consistently reduce the dry mass gap between the electropump and gas generator cycles.

The electric motors are the second largest source of mass for the feed system and impede the payload capacity of the electropump cycle due to their dead mass after use. One of the options to improve the electric motors' structural mass is increasing the motor's speed. However, the increase in speed also increases the motor's frictional losses, decreasing the motor's mechanical efficiency, increasing the power requirement, and negatively affecting the battery pack mass. The high-speed motors also require filling the pump inlet, which reduces the hydraulic efficiency of the pump. There is eventually a critical point where the battery pack mass increase exceeds the decrease in structural mass and increases the feed system mass. This problem can be overcome by adding an inducer that pressurizes the propellant at the pump inlet to increase the pump speed, reducing the motor's mass and size, helping prevent cavitation, and reducing boost pressure from the propellant tanks.

5.3.2. Gas Generator Cycle

The same sensitivity analysis was conducted for the first and second stages of the CLV gas generator feed system. The gas generator feed cycle has four variables that influence the mass of components that contribute to the feed cycle: turbine efficiency, turbine energy power density, and the efficiencies of the oxidizer and fuel pumps. Table 5-7 and Figure 5-7 provide the sensitivity impact levels the four-gas generator feed system input variables had on the mass of the supply system of the first stage of CLV.

Table 5-7: CLV first-stage gas generator mass sensitivity of the feed system

Parameter	**Impact Level**				**Average Sensitivity**	**Sensitivity Rating**
	-10%	**-5%**	**5%**	**10%**		
η_{tu}	0.74	0.70	0.63	0.61	0.67	1
δ_{tu}	0.095	0.090	0.081	0.077	0.086	4
η_{fpu}	0.31	0.30	0.27	0.26	0.28	3
η_{opu}	0.52	0.50	0.45	0.43	0.47	2

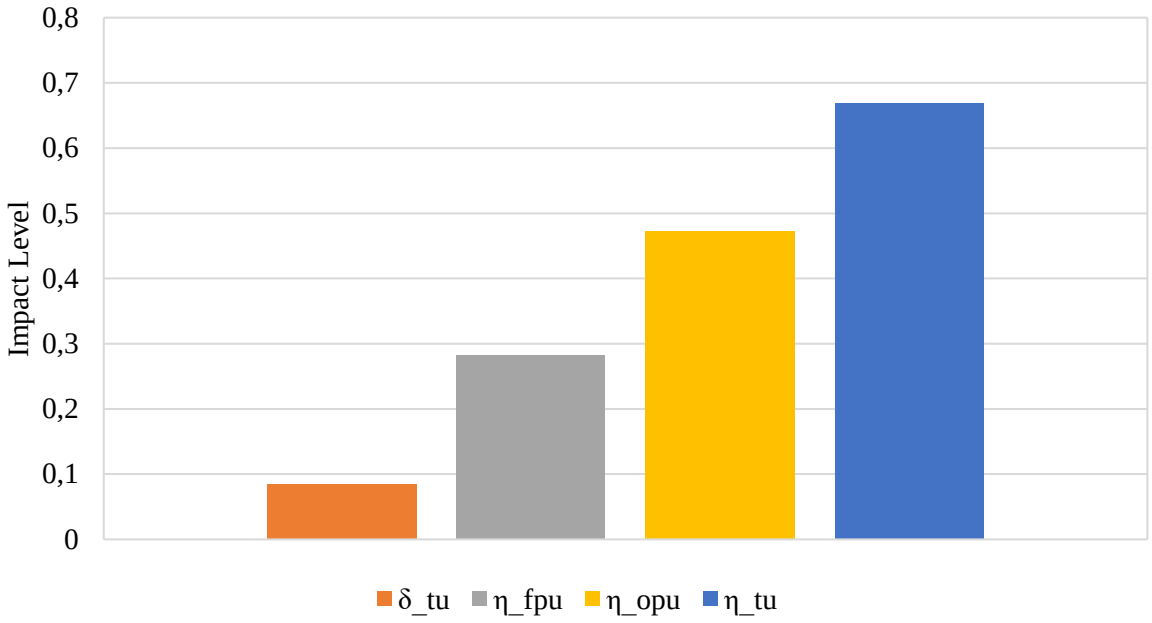

Figure 5-7: First-stage gas generator mass sensitivity of each factor

Table 5-8 and Figure 5-8 contain the sensitivity impact levels of the gas generator cycle's input variables on the mass of the supply system of the second stage of CLV.

Table 5-8: CLV second-stage gas generator mass sensitivity of the feed system

Parameter	Impact Level				Average Sensitivity	Sensitivity Rating
	-10%	-5%	5%	10%		
η_{tu}	0.99	0.94	0.85	0.81	0.90	1
δ_{tu}	0.088	0.086	0.075	0.072	0.080	4
η_{fpu}	0.35	0.34	0.30	0.29	0.32	3
η_{opu}	0.73	0.69	0.62	0.60	0.66	2

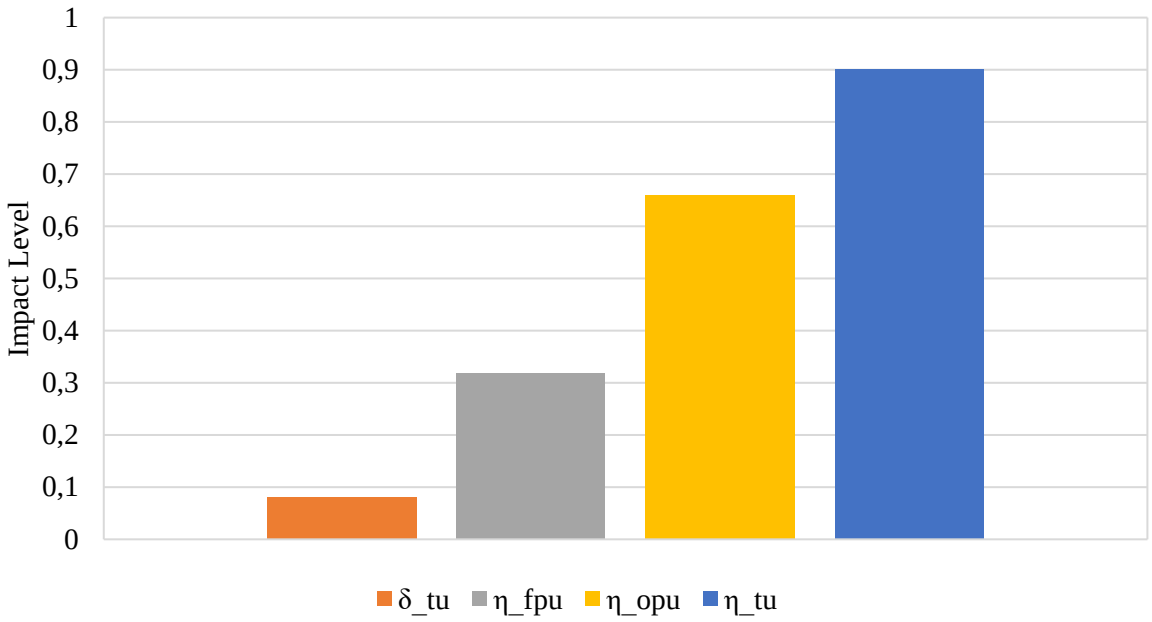

Figure 5-8: Second-stage gas generator mass sensitivity of each factor

Tables 5-7 and 5-8 show that both stages of CLV's gas generator feed systems have the same sensitivity ranking. Table 5-7 and Figure 5-7 of the first-stage gas generator feed system and Table 5-8 and Figure 5-8 of the second-stage gas generator feed system show that the turbopump's most influential variable is the turbine efficiency.

The turbine efficiency influences the amount of propellant consumed by the turbopump to supply sufficient power to the oxidizer and fuel pumps. When turbine efficiency decreases, the mass of propellant consumed by the gas generator increases, increasing the wet mass of the launch vehicle. Unlike the electropump cycle, where the equivalent mass to the gas generator tap-off propellant is the battery pack, the tap-off propellants are not dead mass and do not heavily influence the vehicle's payload capacity. The turbine efficiency has the greatest influence on the feed system mass, but it does not play a crucial role in increasing the vehicle's dry mass, which has a direct influence on the payload capabilities. The turbine efficiency should still be maximized to reduce the wet mass of the vehicle and maximize the payload capacity. The turbine energy density only influences the mass of the turbopump. It has a small contribution to the feed system mass and has a low sensitivity impact on the feed system. Similar to the electropump cycle, the efficiencies of the oxidizer and fuel pump have the second and third highest impact levels on the feed system as they influence the mass of the turbopump and the amount of propellant consumed by the gas generator. The oxidizer pump efficiency has a higher impact ranking than the fuel pump efficiency due to the higher density of the liquid oxygen and a larger propellant mass fraction, implying a larger influence on the power requirement changes when the efficiency is varied.

5.4. Payload Performance Comparison

To evaluate the payload mass that CLV can achieve for each SAFFIRE engine variation, the feed cycle masses from section Chapter 5.2 were combined with additional masses, including the engine, gimbal, thrust structure, plumbing, avionics interstage, RCS, and the payload fairing mass included.

5.4.1. Launch Vehicle Mass

This section provides a performance comparison between the four SAFFIRE engine variations regarding the total wet and dry mass and how these masses influenced the payload mass that each engine cycle can theoretically achieve. The wet and dry masses of the first and second stages of CLV for the four-rocket engine configurations are displayed in Table 5-9.

Table 5-9: Wet and dry masses of each stage of CLV

Parameter	1st Stage	2nd Stage
Elec Ablative Wet Mass	16,161.87 kg	2,657.59 kg
Elec Ablative Dry Mass	1384.32 kg	320.66 kg
Elec Regen Wet Mass	16,227.52 kg	2,688.81 kg
Elec Regen Dry Mass	1,411.61 kg	326.88 kg
GG Ablative Wet Mass	16,483.37 kg	2,698.18 kg
GG Ablative Dry Mass	1,245.66 kg	270.81 kg
GG Regen Wet Mass	16,492.76 kg	2,704.35 kg
GG Regen Dry Mass	1,255.05 kg	271.29 kg

Table 5-9 shows that the regeneratively cooled rocket engines have a larger wet and dry mass than the ablatively cooled rocket engines. For the first and second-stage electropump rocket engines, the dry mass of the ablatively cooled rocket engine weighed 27.29 kg and 6.22 kg less than the regeneratively cooled rocket engine. The same pattern was identified for both the gas generator cycle stages, where the first stage ablatively cooled engine weighed 9.84 kg less than the regeneratively cooled rocket engine, and the second stage ablatively cooled engine weighed 0.48 kg less than the regeneratively cooled rocket engine. The regeneratively cooled feed cycles are heavier due to the increased power required for the fuel pump.

Table 5-10 contains the power consumed by the fuel and oxidizer pumps for each cooling method's electropump and turbopump power of the gas generator cycle. Table 5-10 shows that the first stage fuel pump power increased from 28.23 kW to 31.06 kW for the electropump cycle and 34.49 kW to 37.77 kW for the second stage regeneratively cooled rocket engine, leading to an increase in mass of the regeneratively cooled rocket engines. The turbopump power required for the regeneratively cooled engines also increases due to the increased pressure demand of the regenerative cooling, with the first

stage turbopump power increasing from 74.51 kW to 77.78 kW and the second stage engine turbopump power increasing from 72.12 kW to 74.56 kW.

Table 5-10: Flownex® output thrust, electropump, and turbopump power output

Parameter	Symbol	Value
1st Stage Ablative Electropump Fuel Pump Power	$P_{fpu,\,a}$	28.23 kW
1st Stage Regenerative Electropump Fuel Pump Power	$P_{fpu,\,r}$	31.06 kW
1st Stage Electropump Oxidizer Pump Power	P_{opu}	30.69 kW
2nd Stage Ablative Electropump Fuel Pump Power	$P_{fpu,\,a}$	34.49 kW
2nd Stage Regenerative Electropump Fuel Pump Power	$P_{fpu,\,r}$	37.77 kW
2nd Stage Electropump Oxidizer Pump Power	P_{opu}	46.48 kW
1st Stage Ablative Gas Generator Turbopump Power	$P_{tp,\,a}$	74.51 kW
1st Stage Regenerative Gas Generator Turbopump Power	$P_{tp,\,r}$	77.78 kW
2nd Stage Ablative Gas Generator Turbopump Power	$P_{tp,\,a}$	72.12 kW
2nd Stage Regenerative Gas Generator Turbopump Power	$P_{tp,\,r}$	74.56 kW

An increase of approximately 3 kW for each regeneratively cooled engine is required to overcome the 1.8 bar pressure drop of the cooling channels, increasing the required exit pressure from the fuel pump. Equation 3-28 and equations 3-43 to 3-54, found in Chapter 3, show that the mass of feed cycle components, including the turbopump, the two electropump propellant pumps, the electric motor, the inverter, and the battery pack, are directly proportional to the power required by the propellant pumps and increase in mass due to the increased power required by the fuel pump.

Tables 5-11 and 5-12 contain the thrust output produced by the first and second-stage SAFFIRE engines extracted from the Flownex® simulations. The first stage SAFFIRE engine variations output thrust was tested at sea level, optimum pressure for the given engine's expansion ratio, and vacuum. The second-stage engines were simulated in vacuum conditions.

Table 5-11: First and second stage SAFFIRE engine output thrust

Parameter	Symbol	Value
1st Stage Ablative Electropump Sea Level Thrust	$F_{epc,a(sl)}$	25.82 kN
1st Stage Regenerative Electropump Sea Level Thrust	$F_{epc,\,r(sl)}$	26.86 kN
1st Stage Ablative Gas Generator Sea Level Thrust	$F_{ggc,\,a(sl)}$	25.85 kN
1st Stage Regenerative Gas Generator Sea Level Thrust	$F_{ggc,\,r(sl)}$	26.88 kN

Table 5-12: First and second stage SAFFIRE engine output thrust continued

Parameter	Symbol	Value
1st Stage Ablative Electropump Optimum Thrust	$F_{epc,a(op)}$	29.08 kN
1st Stage Regenerative Electropump Optimum Thrust	$F_{epc,\ r(op)}$	29.21 kN
1st Stage Ablative Gas Generator Optimum Thrust	$F_{ggc,\ a(op)}$	29.11 kN
1st Stage Regenerative Gas Generator Optimum Thrust	$F_{ggc,\ r(op)}$	29.23 kN
1st Stage Ablative Electropump Vacuum Thrust	$F_{epc,a(vac)}$	32.71 kN
1st Stage Regenerative Electropump Vacuum Thrust	$F_{epc,\ r(vac)}$	32.27 kN
1st Stage Ablative Gas Generator Vacuum Thrust	$F_{ggc,\ a(op)}$	32.74 kN
1st Stage Regenerative Gas Generator Vacuum Thrust	$F_{ggc,\ r(op)}$	32.29 kN
2nd Stage Ablative Electropump Vacuum Thrust	$F_{epc,\ a(vac)}$	33.77 kN
2nd Stage Regenerative Electropump Vacuum Thrust	$F_{epc,\ r(vac)}$	34.01 kN
2nd Stage Ablative Gas Generator Vacuum Thrust	$F_{ggc,\ a(vac)}$	33.80 kN
2nd Stage Regenerative Gas Generator Vacuum Thrust	$F_{ggc,\ r(vac)}$	34.04 kN

The results in Tables 5-11 and 5-12 show that the regeneratively cooled SAFFIRE rocket engines produced more thrust than the ablatively cooled engines at sea level and the optimum pressure. The same pattern is identified for the vacuum thrust of the second-stage rocket engines. The increase in thrust is due to the increased temperature of the fuel before entering the combustion chamber from the engine's cooling channels. The ablatively cooled rocket engine fuel enters the combustion chamber at 24.79°C, lower than the inlet temperature of 188.13°C for the regeneratively cooled electropump engine and 204.98°C for the regeneratively cooled gas generator cycle. The difference in temperature between the electropump and gas generator cycles is due to the increased thermal energy transfer from the turbopump compared to the electropump cycle. As the RP-1 increases in temperature, the energy density of the fuel increases, improving combustion efficiency and producing more thrust. Despite the first stage rocket engine's regeneratively cooled rocket engines producing more thrust at sea level and the optimum pressure, the ablatively cooled engines are superior in vacuum. The regeneratively cooled rocket engine has a higher sea level and optimum thrust due to the increased energy density of the fuel, with additional performance resulting from the smaller expansion ratio of 10.5, allowing for the thrust to be affected less by over-expansion than the larger expansion ratio of 13.5 for the ablative engines. The vacuum thrust of the first stage engine in Table 5-11 shows that the electropump ablatively cooled engine produced 440 N more than the regeneratively cooled engine, and the gas generator ablative engine produced 450 N less than the regenerative engine. When the rocket engines surpass their optimum atmospheric pressure where the nozzle is ideally expanded, the exit pressure exceeds the

atmospheric pressure, leading to under-expansion of the plume, reducing the efficiency and amount of thrust produced. The optimum pressure for the ablatively cooled engines is 53.36 kPa, which is 3.84 kPa greater than the optimum pressure of the regeneratively cooled engines. Thus, the ablatively cooled engines can achieve a higher altitude before losing thrust due to under-expansion and consistently produce more thrust than the regeneratively cooled engines in low-pressure environments because of the larger expansion ratio.

5.4.2. Payload Mass

Using the input parameters of the mass estimating relationships discussed in Chapter 4-7 and the Flownex® output values found in Tables 5-9, 5-10, 5-11, and 5-12, the payload masses of the four SAFFIRE engine configurations were calculated using the mass estimating relationships of Chapter 3 and the Launcher Calculator® payload software. Table 5-13 contains the payload masses of the four SAFFIRE engine variations for an apogee range from 200 km to 1000 km Sun Synchronous Orbit (SSO) and represents a key set of data for this study.

Table 5-13: CLV payload masses for each engine variation at SSO

	Electropump Cycle		**Gas Generator Cycle**	
Altitude	**Ablative Mass**	**Regen Mass**	**Ablative Mass**	**Regen Mass**
200 km	343 kg	329 kg	434 kg	428 kg
300 km	329 kg	316 kg	419 kg	414 kg
400 km	315 kg	302 kg	405 kg	400 kg
500 km	303 kg	290 kg	392 kg	386 kg
600 km	290 kg	278 kg	379 kg	374 kg
700 km	278 kg	266 kg	366 kg	361 kg
800 km	267 kg	255 kg	354 kg	349 kg
900 km	256 kg	244 kg	342 kg	338 kg
1000 km	245 kg	234 kg	331 kg	327 kg

The initial goal for CLV was to place a 200 kg payload at 500 km SSO. As seen in Table 5-13, all the SAFFIRE rocket engine configurations exceed the goal of 200 kg. The payload estimates are conservative values as a less detailed analysis of the launch vehicle was conducted. The masses of the valves, tank baffles, flight computers, and structural rib were omitted from the study due to insufficient information available to evaluate the components. The electropump cycle exceeded this limit with a payload mass of 303 kg for the ablative engine and 290 kg for the regenerative engine. Compared with the gas generator cycle, the estimated payload mass is larger, achieving an estimated mass of 392 kg for the ablative engine and 386 kg for the regenerative engine. The same pattern is observed for the

remaining orbit apogees, with the gas generator cycle exceeding the electropump cycle by an average increase payload of 88.44 kg.

The increase in performance of the gas generator cycle is due to the lower dry mass of each stage. The dry mass of the first stage ablative gas generator cycle is 138.66 kg lighter than the electropump cycle, and the regeneratively cooled engine is 156.56 kg lighter than the electropump cycle. The same pattern is identified for the second stage, with the gas generator ablative engine weighing 49.85 kg lighter and the gas generator regenerative engine weighing 55.59 kg less than the electropump cycle, which increases the payload mass. The large difference in the dry mass is due to the dead mass of the electric motors and battery packs of the electropump cycle, which remain onboard the vehicle after the burn time is complete. Upon further analyzing the difference in payload masses between the electropump and gas generator cycle, it is seen that as the orbit apogee increases, the electropump payload deficit decreases.

Figure 5-9 is a visual display of the CLV payload masses for the four SAFFIRE engines.

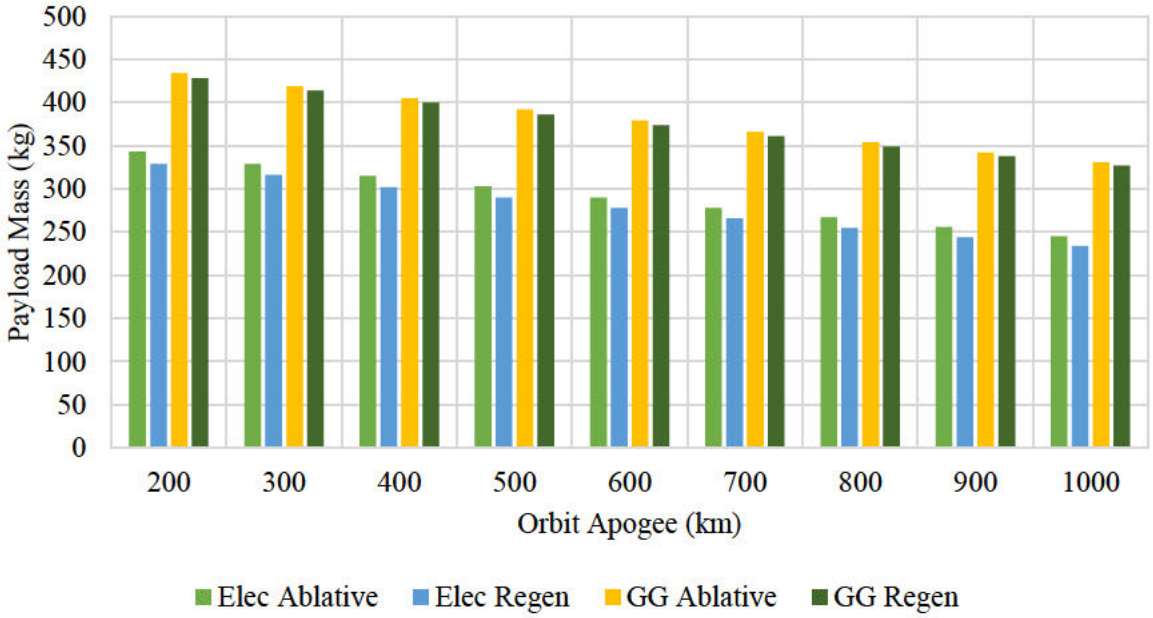

Figure 5-9: Payload mass comparison between the four SAFFIRE variations

At 200 km, the deficit to the gas generator cycle is 91 kg for the ablative engine and 99 kg for the regenerative engine. For the final apogee altitude of 1000 km, the payload deficit is reduced to 86 kg and 93 kg for the ablative and regenerative engines. Using the velocity increment, delta-V, to evaluate the performance of engine cycles, the delta-V required for the 200 km SSO orbit is 8091.1 m/s and 8550.7 m/s for the 1000 km SSO orbit, requiring a longer burn time for each stage of the vehicle to achieve the desired delta-V target. The electropump and turbopump required power is sensitive to the burn time. When the burn time increases, the volumetric flow rate and pump head decrease, requiring

less power. The power reduction required from the pumps implies smaller electric motors and battery packs can be used for the electropump cycle, reducing the dry mass penalty of the engine cycle since the motors and battery packs remain as dead weight after the burn time has terminated, decreasing the payload mass deficit between the electropump and gas generator cycle.

Figure 5-9 also shows that the payload mass of the ablatively cooled engines is larger than the regeneratively cooled engines for each engine apogee. The underperformance of the regeneratively cooled engines is linked to the loss in vacuum thrust due to the smaller expansion ratio and the increased dry mass of the regeneratively cooled engines. A separate analysis was conducted to evaluate the payload mass of the regeneratively cooled engines using the same expansion ratio of 13.5 as the ablative engines. Table 5-14 contains the updated thrust values for the electropump and gas generator regeneratively cooled rocket engines.

Table 5-14: Thrust for 13.5 expansion ratio regeneratively cooled engine

Parameter	Symbol	Value
1st Stage Regenerative Electropump Sea Level Thrust	$F_{epc,\ r(sl)}$	26.03 kN
1st Stage Regenerative Gas Generator Sea Level Thrust	$F_{ggc,\ r(sl)}$	26.05 kN
1st Stage Regenerative Electropump Optimum Thrust	$F_{epc,a(op)}$	29.28 kN
1st Stage Regenerative Gas Generator Optimum Thrust	$F_{ggc,\ r(op)}$	29.31 kN
1st Stage Regenerative Electropump Vacuum Thrust	$F_{epc,\ r(vac)}$	32.92 kN
1st Stage Regenerative Gas Generator Vacuum Thrust	$F_{ggc,\ r(vac)}$	32.94 kN

When comparing the updated regeneratively cooled thrust values with the new 13.5 expansion ratio, it was found that the sea level thrust decreased by 800 N for the electropump and gas generator cycle. The decrease in thrust was expected as the larger expansion ratio leads to the rocket engine being more susceptible to over-expansion at sea level, reducing the thrust output. At the optimum operating pressure, where the exit and atmospheric pressure are the same, the output thrust increases by 100 N for each engine. The vacuum thrust also increased for each engine cycle, with each updated regeneratively cooled engine producing 700 N more thrust than the 10.5 expansion ratio engine. The regeneratively cooled engines also produced more thrust than the ablatively cooled engines for each exit pressure, confirming that the fuel's increased energy density from the higher inlet temperature increased output thrust.

The mass estimating relationships and input parameters for the Launcher Calculator® were updated with the new thrust values to evaluate updated payload masses for the SAFFIRE engine configurations. Table 5-15 contains the updated payload masses for the SAFFIRE engine configurations with a 13.5 expansion ratio.

Table 5-15: CLV payload mass comparison with equal 13.5 expansion ratios

	Electropump Cycle		Gas Generator Cycle	
Altitude	**Ablative Mass**	**Regen Mass**	**Ablative Mass**	**Regen Mass**
200 km	343 kg	349 kg	434 kg	448 kg
300 km	329 kg	334 kg	419 kg	433 kg
400 km	315 kg	321 kg	405 kg	419 kg
500 km	303 kg	308 kg	392 kg	405 kg
600 km	290 kg	295 kg	379 kg	392 kg
700 km	278 kg	283 kg	366 kg	379 kg
800 km	267 kg	272 kg	354 kg	367 kg
900 km	256 kg	261 kg	342 kg	355 kg
1000 km	245 kg	250 kg	331 kg	344 kg

Figure 5-10 displays the payload masses of the four rocket engines with an expansion ratio of 13.5 and shows that the regeneratively cooled engines exceed the ablatively cooled engines despite the larger dry mass. The electropump regenerative engine's payload mass increased from 290 kg to 308 kg, while the gas generator cycle payload mass increased from 386 kg to 405 kg. The increase in thrust produced by the increased energy density of the hotter fuel produced enough thrust to overcome the weight penalty and produce a larger payload mass for CLV when the expansion ratios are the same as the ablatively cooled engines.

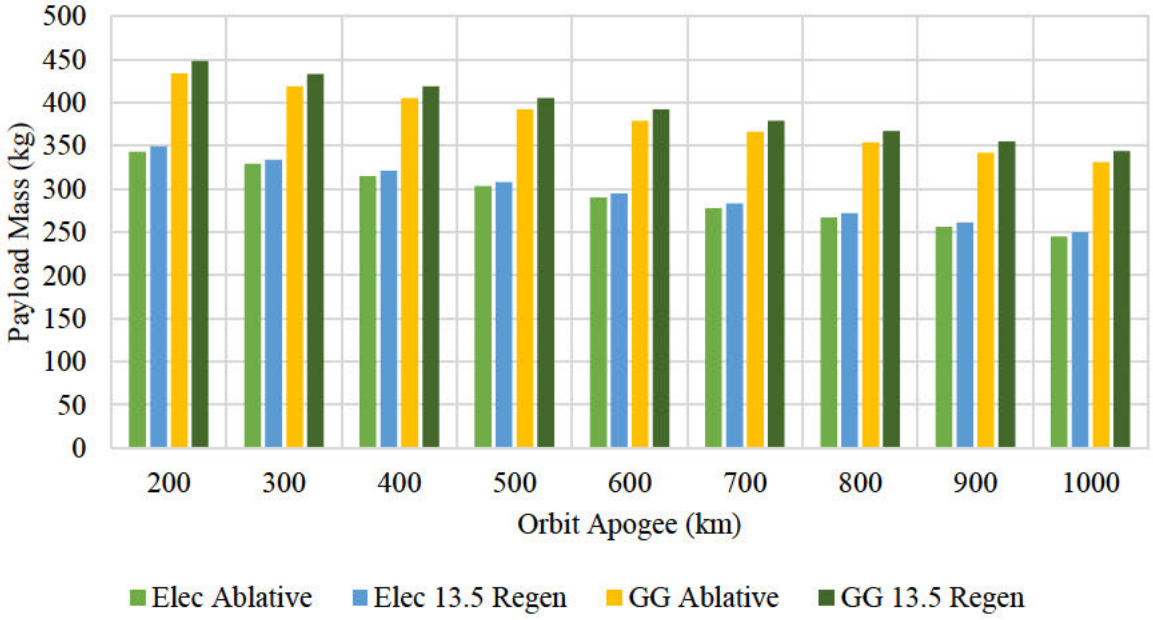

Figure 5-10: CLV payload mass with a 13.5 expansion ratio for all the engines

A significant disadvantage of electropump rocket engines is the dry mass penalty due to the electrical components of the feed cycle. The largest contributor to the high dry mass penalty is the battery pack used to power the electric motors for the pumps. Unlike the gas generator cycle, which utilizes combusted tap-off propellant to power the pumps and has no residual mass, the battery pack mass remains as a dry mass after the burning terminates and significantly impedes the vehicle's payload capacity, as seen in Figure 5-9 and Figure 5-10. The battery packs can be hot-swapped to reduce the dry mass penalty. This involves ejecting the depleted battery packs once their energy has been depleted without interrupting the power supply to the electric motors. Rocket Lab's Electron rocket has proven the viability of this option, successfully ejecting two of the three battery packs of the second stage and two battery packs from the booster stage to shed mass. Assuming that CLV can shed two-thirds of its battery pack mass for the second stage and one-third for the booster stage, updated electropump payload masses were calculated and are displayed in Table 5-16 and Figure 5-11.

Table 5-16: CLV payload mass comparison with the jettisoned battery packs

	Electropump Cycle		**Gas Generator Cycle**	
Altitude	**Ablative Mass**	**Regen Mass**	**Ablative Mass**	**Regen Mass**
200 km	402 kg	392 kg	434 kg	428 kg
300 km	389 kg	379 kg	419 kg	414 kg
400 km	376 kg	366 kg	405 kg	400 kg
500 km	363 kg	354 kg	392 kg	386 kg
600 km	351 kg	342 kg	379 kg	374 kg
700 km	340 kg	331 kg	366 kg	361 kg
800 km	329 kg	320 kg	354 kg	349 kg
900 km	319 kg	310 kg	342 kg	338 kg
1000 km	308 kg	300 kg	331 kg	327 kg

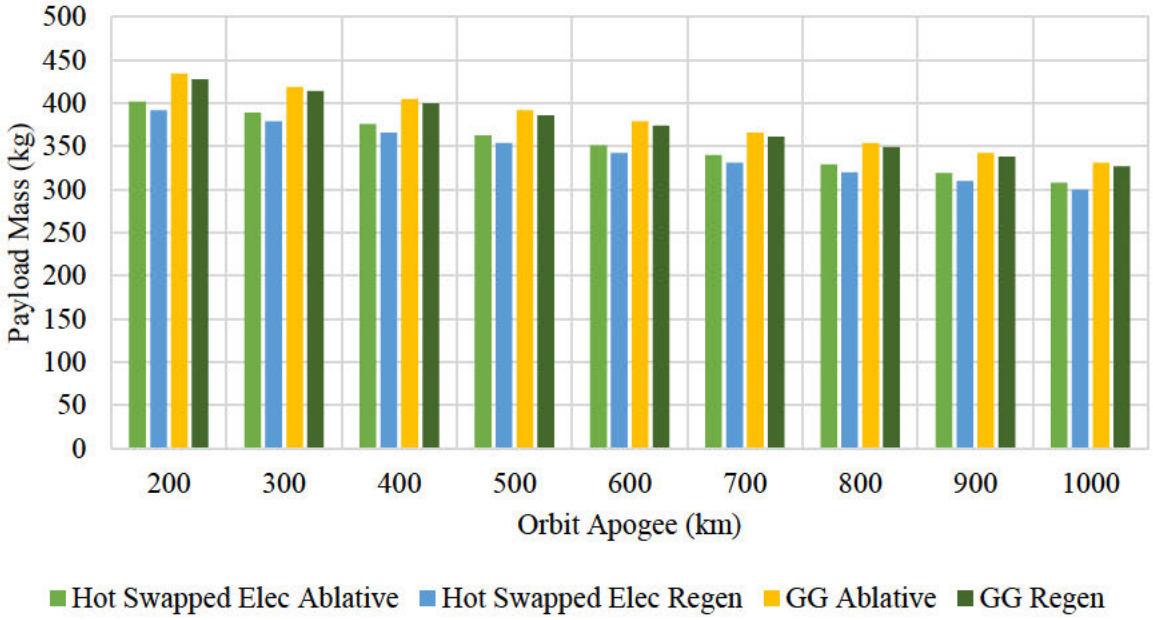

Figure 5-11: Payload mass comparison with hot-swapped batteries

Hot-swapping the depleted batteries reduced the booster stage dry mass by 74.3 kg for the regenerative engines and 70.9 kg for the ablatively cooled engines. The second stage dry mass was reduced by 27.7 kg and 26.9 kg for the regenerative and ablative engines. As a result of the dry mass reduction, the payload mass increased to values equivalent to the gas generator cycle. Figure 5-11 shows that the payload mass increased by 60 kg for the ablatively cooled engine and 64 kg for the regeneratively cooled engine for a 500 km SSO orbit. For each orbit apogee, the average payload difference was 27.3 kg between the gas generator cycle and the electropump cycle with jettisoned batteries, which is a 69.1% reduction in the payload shortfall of the electropump cycle compared to the gas generator cycle. The electropump payload mass deficiency was further decreased by 13% when the orbit apogee exceeded a 500 km SSO apogee due to the longer burn times, reducing the payload penalty of the electropump cycle.

6. Conclusion and Future Work

The primary aim of this study was to conduct an in-depth analysis and performance comparison of the four SAFFIRE engine configurations that are currently under consideration to be used on the first and second stage of the hypothetical South African Commercial Launch Vehicle designed to deliver a 200 kg payload to a 500 km SSO. The four SAFFIRE engine configurations consisted of the electropump cycle and gas generator cycles, each under ablative and regenerative cooling. The objectives of the study were as follows:

1) Develop a methodology to create a one-dimensional model of the SAFFIRE engine configurations in Flownex® for a steady-state analysis and verify the accuracy of the results using the Fastrac and Rutherford Engines.
2) Identify mass-estimating relationships that utilize the exported parameters from the Flownex® models and design characteristics of the engine.
3) Evaluate the mass of the feed cycle for each stage of the launch vehicle and the payload capability of the launch vehicle for each engine configuration.
4) Conduct a sensitivity impact analysis on the feed cycles.
5) Identify areas for future research.

The subsequent sections contain a discussion of the objectives and their fulfillment in identifying the performance of each SAFFIRE engine configuration, followed by future recommendations.

6.1. Analysis Methodology and Accuracy

The methodology for modeling the SAFFIRE liquid rocket engine as a one-dimensional model was based on the modular methodology conducted by Naderi and Liang, (2019), where the rocket engine is broken into interconnected modules that can be individually modeled and tested. The modular method is specifically useful for steady-state analyzes as it allows numerous components to be excluded from the simulation without hindering the accuracy of the results. The methodology used to model each subcomponent of the first and second-stage SAFFIRE engine configurations was presented in Chapter 4.

Each SAFFIRE engine was created in Flownex® using the built-in elements. Flownex® also contained a fluids library with two kerosene fuels, JP-10 and JP-8, but both were unusable. The JP-10 density was too high to represent RP-1, and the JP-8 was missing fluid data for pressures above 1 bar. Therefore, a new project-based surrogate mixture of RP-1 was created in NIST and imported into the Flownex® simulations. Huber et al., (2009) identified that the surrogate mixture of the RP-1 could be represented using α-Methyldecalin, n-Dodecane, 5-Methylnonane, and Heptylcyclohexane. Comparisons with experimental data of the fuel sample demonstrated that the surrogate mixture could represent the

density, sound speed, viscosity, and thermal conductivity to within 0.4%, 2%, 2%, and 4% error at a 95% confidence level (Huber et al., 2009).

To verify that the modular Flownex® models of the electropump and gas generator cycles produced accurate results using the surrogate mixture of RP-1, the identical electropump and gas generator Flownex® were used to model the Fastrac and Rutherford rocket engines using each engine input variables. The Rutherford engines had a maximum percentage error of 1.82% for the fuel pump efficiency, with the oxidizer pump efficiency having the second highest error of 1.08%. These errors can be further minimized if the actual Rutherford pump curves are used in the simulation. The performance of the Rutherford combustion chamber and nozzle model in Flownex® was also acceptable, with a maximum error of 0.53% for the combustion chamber pressure. Therefore, the performance parameters of the Flownex® model are in close comparison to the values stipulated by Liu et al., (2021), and it can be concluded that Flownex® is capable of adequately modeling an electropump rocket engine.

The Fastrac gas generator engine has a maximum percentage error of 3.8% for the fuel pump efficiency. The Fastrac engine turbopump pump curves and turbine input variables were based on the best efficiency point and operating speed and were estimated within Flownex® in the same way as the electropump. It is likely that metrics such as efficiency, exit pressure, and the power consumed by the pumps would decrease with the use of more accurate pump data. The combustion chamber pressure was modeled identically to the design value with a 0% error, and the chamber temperature had a 2.32% error. The combustion chamber pressure was also close to the findings of Garcia and Nasa, (1999) with a 0.42% error and resulted in accurate thrust readings to be estimated by the Flownex®. The maximum error for the performance parameters of the rocket engine was 1.06% for the sea level thrust with vacuum thrust and the I_{sp} of both the altitude readings below 1%, showing good proximity to the design and test data of the Fastrac engine.

The results of the Rutherford electropump cycle and the Fastrac gas generator Flownex® model's simulations were within 5% error. Thus, it can be concluded that the Flownex® models of the SAFFIRE engines provided realistic performance values used in the mass estimating relationships to evaluate the feed cycle mass and the payload capacity of CLV for each SAFFIRE engine configuration.

6.2. Feed Cycle Analysis

One of the most important features of a rocket is minimizing the initial mass of each stage to maximize the payload capabilities of the launch vehicle. The combustion chamber propellants for the electropump and gas generator cycles were calculated to be the same for the first and second-stage SAFFIRE engines as the mass flowrates and burn times remained constant and were not influenced by the additional 1% thrust increase from the gas generator exhaust gases.

The gas generator tap-off propellant mass was compared to the battery pack mass as both are a source of energy used to drive the pumps. The burn time of 163 seconds for the booster stage and 236 seconds for the second stage engine is greater than the characteristic burn time of 103 seconds for the battery pack. This led to an energy-constrained battery pack, resulting in a higher mass of the battery pack compared to its power density. The GG propellant mass was 11% less than the battery pack mass for the first-stage engine and 33% less for the second-stage engine. Future lithium polymer batteries require a higher energy density for the battery pack mass to be minimized and approach the performance of the gas generator cycle. For the first stage battery pack mass to weigh the same as the mass of the GG propellants, the energy density must increase from 198 Wh/kg to 220 Wh/kg and match the mass of the propellants consumed by the gas generator cycle. For the battery pack to have a characteristic burn time equal to the burn time of the booster stage and approach the payload capacity of the gas generator cycle, the energy density must increase to 314.68 Wh/kg for the same power density of 6.95 kW/kg. The second stage battery pack energy density must increase from 198 Wh/kg to 264 Wh/kg to match the GG propellant mass and must increase to 510 W/kg to approach the payload capabilities of the gas generator cycle and minimize the battery pack mass penalty.

The electropump cycle tank mass was 1% lower than the gas generator cycle for both stages of CLV due to the gas generator cycle tanks requiring a large volume to account for the additional propellants for the gas generator. The poor power density of the electric motors of the electropump cycle is emphasized in the first and second stage feed systems, with the first stage electropump cycle weighing 1.66 times more than the gas generator feed system and the second stage feed system weighing 4.22 times more. The increased dry mass of the electropump cycle from the high electric motor and battery pack mass leads the electropump cycle to be 1.73 times larger than the gas generator cycle for the first stage and 1.92 times larger for the second stage.

From the sensitivity analysis conducted on the electropump cycle, the oxidizer and fuel pump efficiency, the electric motor efficiency and power density, the inverter efficiency, and the energy density of the battery pack have the largest impact on the mass of the feed system. With significant advancements in battery and motor technology, the overall mass of the electropump cycle will continue to decrease and potentially become comparable with the gas generator cycle.

From the gas generator cycle sensitivity analysis, the turbine efficiency influences the amount of propellant consumed by the turbopump to supply sufficient power to the oxidizer and fuel pumps. When there is a decrease in turbine efficiency, the mass of propellant consumed by the gas generator increases, which is the largest mass contributor to the feed system mass and increases the wet mass of the launch vehicle. The turbine efficiency should still be maximized to reduce the wet mass of the vehicle and maximize the payload capacity. The turbine energy density only influences the mass of the turbopump.

It does not contribute a large mass to the feed system, thus having a low sensitivity impact on the feed system.

6.3. Vehicle Payload Capacity

For the first-stage and second-stage electropump rocket engines, the dry mass of the ablatively cooled rocket engine weighed 27.29 kg and 6.22 kg less than the regeneratively cooled rocket engine. The same pattern was identified for both the gas generator cycle stages, where the first stage ablatively cooled engine weighed 9.84 kg less than the regeneratively cooled rocket engine, and the second stage ablatively cooled engine weighed 0.48 kg less than the regeneratively cooled rocket engine. The regeneratively cooled feed cycles are heavier due to the increased power required for the fuel pump. The first and second-stage fuel pump power for the regeneratively cooled electropump cycle increased from 28.23 kW to 31.06 kW and 34.49 kW to 37.77 kW, respectively. The turbopump power required for the regeneratively cooled engines also increases due to the increased pressure demand of the regenerative cooling, with the first stage turbopump power increasing from 74.51 kW to 77.78 kW and the second stage engine turbopump power increasing from 72.12 kW to 74.56 kW. An approximate increase of 3 kW for each regeneratively cooled engine is required to overcome the 1.8 bar pressure drop of the cooling channels, increasing the required exit pressure from the fuel pump. Equations 3-28 and equations 3-43 to 3-54, found in Chapter 3, show that the mass of the turbopump, the two electropump propellant pumps, the electric motor, the inverter, and the battery pack are directly proportional to the power required by the propellant pumps and increase in mass due to the increased power required by the fuel pump.

The initial goal for CLV was to place a 200 kg payload at 500 km SSO, but in this study, all the SAFFIRE rocket engine configurations exceeded the target goal. The masses of the valves, the vehicle's propellant tank baffles, flight computers, and structural ribs were omitted from the study due to insufficient information available to evaluate the components, reducing the vehicle's dry mass and increasing the vehicle's payload capacity. The additional mass of the omitted components will increase the dry mass of the launch vehicle by approximately 120 kg for the first stage and 12.5 kg for the second stage. The changes in the dry mass of the launch vehicle have the potential to decrease CLV's payload capacity by 7.5% at 500 km SSO for the regeneratively and ablatively cooled electropump feed cycle engines. A 7% decrease in payload capacity can be expected for CLV with gas generator cycle engines for under both cooling architectures.

In this study, CLV had a payload capacity of 303 kg for the SAFFIRE ablatively cooled electropump cycle engine and 290 kg for the regeneratively cooled engine. The gas generator SAFFIRE engine exceeded these values, achieving an estimated payload mass of 392 kg for the ablative engine and 386 kg for the regenerative engine. The increase in performance of the gas generator cycle is due to the lower dry mass of each stage. The dry mass of the first stage ablative gas generator cycle is 138.66 kg

lighter than the electropump cycle, and the regeneratively cooled engine is 156.56 kg lighter. The same pattern was identified for the second stage, with the gas generator ablative and regenerative engines weighing 49.85 kg and 55.59 kg less, respectively.

It was also found that the payload difference between the electropump and gas generator cycles decreased with increased orbital apogee for the ablative and regenerative engines. When the burn time increases for higher orbital apogees, the volumetric flow rate and pump head decrease, requiring less power. The power reduction required from the pumps implies smaller electric motors and battery packs can be used for the electropump cycle, reducing the dry mass penalty of the engine cycle since the motors and battery packs remain as dead weight after the burn time has terminated, decreasing the payload mass deficit between the electropump and gas generator cycle.

The thrust produced by the regeneratively cooled rocket engines at sea level is over 1 kN greater than that of the ablatively cooled engines. The thrust at the optimum operating pressure of the regenerative engines is also larger by 220 N. The increase in thrust is due to the higher inlet temperature of the fuel before entering the combustion chamber. When the RP-1 increases in temperature, the energy density of the fuel increases, improving the combustion efficiency and contributing to an increase in thrust. The regeneratively cooled engines have a smaller expansion ratio of 10.5 compared to 13.5 for the ablatively cooled engines. The reduced expansion ratio also assists in producing more thrust at sea level as the exit thrust is affected less by over-expansion. However, when comparing the thrust produced by the first-stage regenerative engines in vacuum conditions, there is a deficit of 440 N for the electropump engines and 450 N for the gas generator cycle. The ablatively cooled engines achieve a higher altitude before losing thrust due to under-expansion and consistently produce more thrust than the regeneratively cooled engines because of the larger expansion ratio. Despite the regeneratively cooled rocket engines offering more thrust from the increased energy density of the fuel, the increased dry mass of the regeneratively cooled engines and the reduced vacuum thrust outweighed the gains in performance. It resulted in a lower payload mass for both regeneratively cooled engine cycles at each orbit apogee.

When the regenerative and ablatively cooled engines utilized the same expansion ratio of 13.5, the electropump regenerative engine's payload mass increased from 290 kg to 308 kg, and the gas generator cycle payload mass increased from 386 kg to 405 kg. The increase in thrust produced by the increased energy density of the hotter fuel produced enough thrust to overcome the weight penalty and allowed for a larger payload capacity for CLV.

A significant disadvantage of the electropump cycle is the battery pack mass, and thus can be overcome by hot-swapping the depleted batteries to reduce the dry mass of the electropump rockets. The reduction in the dry mass by ejecting the depleted batteries reduced the payload shortfall of the electropump by 69.1%. The electropump payload mass deficiency was further decreased by 13% when the orbit apogee

exceeded a 500 km SSO apogee due to the longer burn times, reducing the payload penalty of the electropump cycle.

With the rapid development of electrical and electronic technology, the dead mass of the electric motor and battery pack of the electropump rocket engine will steadily decrease, closing the deficit compared to the gas generator cycle. The electropump cycle offers deep variable thrust, an easy modular design, high reliability, and good payload capacity for CLV compared to the gas generator cycle. Due to its flexible thrust adjustment capability, the electric pump-fed liquid propellant rocket engine can take the place of the turbopump-fed liquid propellant rocket engine to a certain extent. Therefore, it might be argued that electric pump-fed liquid propellant rocket engines have greater development potential and broader application prospects.

6.4. Future Work

The propellant tanks and feed system are some of the main contributors to the dead mass of the launch vehicle for the gas generator and electropump cycle. With advancements in composite materials, a study comparing different tank designs like composite overwrapped tanks and linerless composite tanks can be investigated to identify how they affect the mass of the launch vehicle and the payload capabilities. The selection of the material used for the composite tanks is dependent on the cost, availability, and suitability of the SAFFIRE propellant selection and how it will influence the density, shape, and thickness of the composite tanks.

The Flownex® simulations of the electropump and gas generator cycles can also be updated with new input information like oxidizer pump and fuel pump curves, replacing the basic centrifugal pump element with an improved centrifugal pump element, which will improve the output results for the pumps and potentially the output values downstream of the pumps. A new study into designing a suitable gas generator and turbine for the gas generator cycle SAFFIRE engine will allow for improved input values for the turbine and gas generator elements, which should allow a better torque balance between the turbopump and turbine to be completed. New analyzes might also investigate improved modeling of the gas generator, the main combustion chamber, and the associated combustion losses to improve the output thrust and temperature data accuracy.

References

Aerospace Engineering, 2012. Power Cycles [WWW Document]. Aerospace. URL http://www.aerospacengineering.net/power-cycles/ (accessed 3.24.23).

Akin, D., 2016. ENAE 791 - Launch and Entry Vehicle Design. Maryland: University of Maryland.

Anderson, C., 2017. Milestone for South African satellite technology [WWW Document]. Brand South Africa. URL https://brandsouthafrica.com/124793/science-technology/milestone-for-south-african-satellite-technology-2/ (accessed 3.26.23).

Beck, P., 2019. SSC19-X-01 Making Space on Orbit: Responsible Orbital Deployment in the Era of High-Volume Launch, in: 33rd Annual AIAA/USU Conference on Small Satellite. California.

Browne, E.C., Marchese, A., Windom, B., Watson, T., 2020. Modeling Ablative and Regenerative Cooling Systems for An Ethylene/Ethane/Nitrous Oxide Liquid Fuel Rocket Engine. Colorado.

Chetty, C., 2018. The Hydrodynamic Design and Analysis of an RP-1 Pump for a Liquid Rocket Engine, MScEng Thesis, University of KwaZulu-Natal, Durban.

Demyanenko, Y., Dmitrenko, A., Rachuk, V., Buro Khimavtomatiyi, K., Minick, R.A., Bracken, R., Buser, M., 2006. Single-Shaft Turbopumps in Liquid Rocket Engines, in: 42nd AIAA/ASME/SAE/ASEE Joint Propulsion Conference & Exhibit. American Institute of Aeronautics and Astronautics , Sacramento.

Durakbasa, N.M., G.M.G., 2023. Future of Lithium Ion Batteries for Electric Vehicles: Problems and Expected Developments, in: Durakbasa, N.M., Gençyılmaz, M.G. (Eds.), Towards Industry 5.0. Springer, Cham, Turkey, pp. 524–540.

ESA, 2017. Ariane 6 [WWW Document]. The European Space Agency. URL https://www.esa.int/Enabling_Support/Space_Transportation/Launch_vehicles/Ariane_6 (accessed 3.23.23).

Garcia, R., Nasa, R.W., 1999. Hydrodynamic Design of The Fastrac Turbopump. Marshall Space Flight Center: NASA.

Gopal, S., 2020. Analysis of Different Types of Motors for the Use in Electric Vehicles. International Research Journal of Engineering and Technology.

Gyasi-Agyei, P., 2021. Preliminary Design Considerations for a Commercial Launch Vehicle Upper Stage, MScEng Thesis, University of KwaZulu-Natal, Durban.

Haidn, O.J., 2008. Advanced Rocket Engines. Advances on Propulsion Technology for High-Speed Aircraft 6, 1–40.

Harpale, A., Sawant, S., Kumar, R., Levin, D., Chew, H.B., 2018. Ablative thermal protection systems: Pyrolysis modeling by scale-bridging molecular dynamics. Carbon N Y 130, 315–324. https://doi.org/10.1016/J.CARBON.2017.12.099

Huber, M.L., Lemmon, E.W., Ott, L.S., Bruno, T.J., 2009. Preliminary Surrogate Mixture Models for the Thermophysical Properties of Rocket Propellants RP-1 and RP-2. Energy and Fuels 23, 3083–3088. https://doi.org/10.1021/ef900216z

Huzel, D.K., Huang, D.H., Arbit, Harry., 1992. Modern Engineering for Design of Liquid-Propellant Rocket Engines. American Institute of Aeronautics and Astronautics.

Isaacs, L., 2022. Satellite launches first for SA [WWW Document]. Cape Times. URL https://www.iol.co.za/capetimes/news/satellite-launches-first-for-sa-cab482d3-dbd0-45d3-94da-0122db1d2164 (accessed 2.20.23).

Kauffmann, J., Herbertz, A., Sippel, M., 2001. Systems Analysis of a High Thrust, Low-Cost Rocket Engine. 4th International Conference on Green Propellants for Space Propulsion, Noordwijk, pp. 1–7.

Kwak, H.D., Kwon, S., Choi, C.H., 2018. Performance assessment of electrically driven pump-fed LOX/kerosene cycle rocket engine: Comparison with gas generator cycle. Aerosp Sci Technol 77, 67–82. https://doi.org/10.1016/j.ast.2018.02.033

Lam, M., 2022. Case Study: Gilmour Space uses Grepow batteries for Launch Vehicles [WWW Document]. Case Study. URL https://www.grepow.com/company-news/gilmour-space-uses-grepow-lipo-batteries-for-launch-vehicle.html (accessed 7.18.23).

Law, A., 2022. Rocket Engine Cycles [WWW Document]. Everyday Astronaut. URL https://everydayastronaut.com/rocket-engine-cycles/ (accessed 3.23.23).

Leander, K., 2021. An Integrated System Model of the Rs-25 Liquid-Fuel Cryogenic Rocket [WWW Document]. Blog. URL https://flownex.com/news/spaceflight/ (accessed 5.20.23).

Lee, Y., Kim, J., 2019. Analysis of the Three-Phase Inverter Power Efficiency of a BLDC Motor Drive Using Conventional Six-Step and Inverted Pulse Width Modulation Driving Schemes. Canadian Journal of Electrical and Computer Engineering 42, 34–40. https://doi.org/10.1109/CJECE.2018.2885351

Lemmon, E.W., Bell, I.H., Huber, M.L., McLinden, M.O., 2018. NIST Standard Reference Database 23: Reference Fluid Thermodynamic and Transport Properties-REFPROP.

Liu, Y., Yang, J., He, Y., Ni, Z., Wu, Y., 2021. Concept and Key Technology Analysis of Electric Pump-Fed Liquid Propellant Rocket Engine, in: IOP Conference Series: Earth and Environmental Science. IOP Publishing Ltd. https://doi.org/10.1088/1755-1315/781/4/042016

Macaluso, S.B., Douglass, H.W., 1974. Liquid Rocket Engine Turbines. Cleveland: University of Cleveland.

Mohammad, A.A., Abedin, A., Rahman Khan, Z., 2017. Implementation of a Three Phase Inverter for BLDC Motor Drive. 2016 9th International Conference on Electrical and Computer Engineering (ICECE) 9.

Naderi, M., Liang, G., 2019. Static Performance Modeling and Simulation of The Staged Combustion Cycle LPREs. Aerosp Sci Technol 86, 30–46. https://doi.org/10.1016/j.ast.2018.12.035

Nikishchenko, I., 2020. Launcher Calculator (Version 41) [Computer program]. Available at: https://launchercalculator.com/ (accessed 03 May 2023).

Odunlade, E., 2018. Different Types of Batteries and their Applications [WWW Document]. Article. URL https://circuitdigest.com/article/different-types-of-batteries (accessed 6.21.23).

Percival, C., 2022. Engine Cooling-Why Rocket Engines Don't Melt [WWW Document]. The Everyday Astronaut. URL https://everydayastronaut.com/engine-cooling-methodes/#:~:text=Regenerative%20Cooling,-Regenerative%20cooling%20is&text=While%20the%20walls%20and%20nozzle,order%20to%20keep%20them%20cool.&text=The%20discovery%20of%20this%20was,run%20more%20or%20less%20indefinitely. (accessed 2.20.23).

Polinovel, 2022. Lithium Metal Battery vs Lithium-ion Battery: Which Is Better [WWW Document]. Article. URL https://polinovel.com/lithium-metal-battery-vs-lithium-ion-battery-which-is-better/#:~:text=Firstly%2C%20lithium%2Dion%20batteries%20are,observed%20while%20charging%20and%20discharging. (accessed 6.21.23).

Rachov, P., Tacca, D.L.H., 2010. Electric Feed Systems for Liquid Propellant Rocket Engines. https://doi.org/10.13140/2.1.4431.9042

Rao, A.D., 2010. Gas-fired combined-cycle power plant design and technology. Advanced Power Plant Materials, Design and Technology 32–53. https://doi.org/10.1533/9781845699468.1.32

Rocket Lab USA Inc., 2022. Electron Payload User Guide 7.0. United States of America.

Shepard, J., 2021. The Difference Between Lithium Ion and Lithium Polymer Batteries [WWW Document]. URL https://www.batterypowertips.com/difference-between-lithium-ion-lithium-polymer-batteries-faq/ (accessed 6.21.23).

Smyth, J., 2013. The Design and Analysis of a Kerosene Turbopump for a South African Commercial Launch Vehicle, MScEng Thesis, University of KwaZulu-Natal, Durban.

Space, A., 2019. 10 Advantages of Cube Satellites vs. Conventional Satellites [WWW Document]. Alen Space. URL https://info.alen.space/advantages-of-cubesats-vs-conventional-satellites (accessed 3.20.24).

Sutton, G.P., Biblarz, O., 2001. Rocket Propulsion Elements. John Wiley & Sons: Virginia.

Vashista, S., 2022. Lithium-ion Battery vs Lithium-polymer Battery [WWW Document]. Linkedin. URL https://www.linkedin.com/pulse/lithium-ion-vs-lithium-polymer-batteries-sumit-vashista/ (accessed 7.18.23).

Vezzini, A., 2014. Lithium-Ion Battery Management, in: Lithium-Ion Batteries: Advances and Applications. Elsevier B.V., pp. 345–360. https://doi.org/10.1016/B978-0-444-59513-3.00015-7

Waxenegger-Wilfing, G., Hahn, R.H.S., Deeken, J., 2018. Studies on Electric Pump-Fed Liquid Rocket Engines for Micro-Launcher, in: Space Propulsion 2018. German Aerospace Centre (DLR), Hardthausen am Kocher, pp. 1–6.

Woellert, K., Ehrenfreund, P., Ricco, A.J., Hertzfeld, H., 2011. Cubesats: Cost-effective science and technology platforms for emerging and developing nations. Advances in Space Research 47, 663–684. https://doi.org/10.1016/j.asr.2010.10.009

Wunderlin, N., 2019. Design of a Liquid Propellant Rocket Engine Combustion Chamber, MScEng Thesis, University of Kwazulu-Natal, Durban.

Zhao, J., Yangwei, Y., 2011. Brushless DC Motor Fundamentals Application Note. Monolithic Power Systems.